# ARTICLE IN PRESS

Geochemistry xxx (xxxx) xxx



Contents lists available at ScienceDirect

# Geochemistry

journal homepage: www.elsevier.com/locate/chemer



# INVITED REVIEW

# Chemical equilibrium calculations for bulk silicate earth material at high temperatures

Bruce Fegley Jr a, Katharina Lodders A, Nathan S. Jacobson b

- a Planetary Chemistry Laboratory, Dept. of Earth & Planetary Sciences and McDonnell Center for the Space Sciences, Washington University, St Louis, MO 63130, USA
- b Materials and Structures Division, NASA Glenn Research Center/HX5, 21000 Brookpark Road, Cleveland, OH 44135, USA

#### ARTICLE INFO

Handling Editor: Astrid Holzheid

Keywords:
Condensation temperatures
Earth
Moon
Thermodynamics
High temperatures
Vaporization
Condensation

Oxygen fugacity

#### ABSTRACT

The chemical equilibrium distribution of 69 elements between gas and melt is modeled for bulk silicate Earth (BSE) material over a wide P – T range (1000–4500 K,  $10^{-6}$ – $10^{2}$  bar). The upper pressure end of this range may occur during lunar formation in the aftermath of a Giant Impact on the proto-Earth. The lower pressures may occur during evaporation from molten silicates on achondritic parent bodies. The virial equation of state shows silicate vapor behaves ideally in the P - T range studied. The BSE melt is modeled as a non-ideal solution and the effects of different activity coefficients and ideal solution are studied. The results presented are 50% condensation temperatures, major gas species of each element, and the pressure and temperature dependent oxygen fugacity (fO2) of dry and wet BSE material. The dry BSE model has no water because it excludes hydrogen; it also excludes the volatile elements (C, N, F, Cl, Br, I, S, Se, Te). The wet BSE model has water because it includes hydrogen; it also includes the other volatiles. Some key conclusions include the following: (1) much higher condensation temperatures in silicate vapor than in solar composition gas at the same total pressure due to the higher metallicity and higher oxygen fugacity of silicate vapor (cf. Fegley et al. 2020), (2) a different condensation sequence in silicate vapor than in solar composition gas, (3) good agreement between different activity coefficient models except for the alkali elements, which show the largest differences between models, (4) agreement, where overlap exists, with prior published silicate vapor condensation calculations (e.g., Canup et al. 2015, Lock et al. 2018, Wang et al. 2019), (5) condensation of Re, Mo, W, Ru, Os oxides instead of metals over the entire P - T range, (6) a stability field for Ni-rich metal as reported by Lock et al. (2018), (7) agreement between ideal solution (from this work and from Lock et al. 2018) and real solution condensation temperatures for elements with minor deviations from ideality in the oxide melt, (8) similar 50% condensation temperatures, within a few degrees, in the dry and wet BSE models for the major elements Al, Ca, Fe, Mg, Si, and the minor elements Co, Cr, Li, Mn, Ti, V, and (9) much lower 50% condensation temperatures for elements such as B, Cu, K, Na, Pb, Rb, which form halide, hydroxide, sulfide, selenide, telluride and oxyhalide gases. The latter results are preliminary because the solubilities and activities of volatile elements in silicate melts are not well known, but must be considered for the correct equilibrium distribution, 50% condensation temperatures and mass balance of halide (F, Cl, Br, I), hydrogen, sulfur, selenium and tellurium bearing species between silicate melt and vapor.

# 1. Introduction

The chemistry of hot silicate vapor is important for several reasons yet is little known. For example, the ongoing debate about nebular versus planetary mechanisms responsible for meteoritic and terrestrial abundances of the moderately volatile elements (MVE) and Earth's volatility trend (e.g., Braukmüller et al., 2019; Fegley et al., 2020) dates back over 45 years to the MVE condensation calculations of Wai and Wasson (1977) and the discussion of lunar and terrestrial siderophile

and volatile elemental abundances by Ringwood and Kesson (1977). Isotopic evidence for MVE depletion during planetary formation, and experimental and theoretical studies of major element and MVE evaporative loss from meteorite parent bodies, the Moon, and Mars after dissipation of the solar nebula are attracting increased attention (Canup et al., 2015; Lock et al., 2018; Jiang et al., 2019; Sossi et al., 2019; Ivanov et al., 2022; Neuman et al., 2022; Tian et al., 2021; Zhang et al., 2021).

Other topics of current interest are the chemistry of silicate vapor

E-mail address: bfegley@wustl.edu (B. Fegley).

https://doi.org/10.1016/j.chemer.2023.125961

Received 14 September 2022; Received in revised form 13 February 2023; Accepted 17 February 2023 Available online 23 February 2023 0009-2819/© 2023 Elsevier GmbH. All rights reserved.

Please cite this article as: Bruce Fegley et al., Geochemistry, https://doi.org/10.1016/j.chemer.2023.125961

<sup>\*</sup> Corresponding author.

atmospheres of hot rocky exoplanets and the chemistry of impact-generated silicate melt – vapor debris disks in our solar system and in exoplanetary systems (Visscher and Fegley, 2013; Lupu et al., 2014; Lock et al., 2018). Condensation and/or evaporation of elements from silicate melt – vapor is important in all these cases. Geochemists have been forced to use condensation temperatures from solar composition gas as a proxy for element volatility in silicate vapor (Lodders, 2003). But there is no reason to expect the same condensation temperatures because hydrogen dominates solar composition gas while oxygen is the major element in silicate vapor. This work models the chemical equilibrium distribution of 69 elements between gas and melt for bulk silicate Earth material over a wide P – T range (1000–4500 K,  $10^{-6}$ – $10^2$  bar) and gives condensation temperatures for the 69 elements studied and the major gas(es) of each element.

This paper is organized as follows:

Section 2 describes computational methods and data sources and is divided into subsections that give an overview of the computations, discuss the CONDOR and FactSage codes, describe the thermodynamic data sources for pure materials, explain details of molten oxide solution modeling in the CONDOR code, present background information on activities and activity coefficients, discuss sources for activity coefficients used in the calculations, and use the virial equation of state to check ideality of bulk silicate Earth vapor under the pressure and temperature conditions in the calculations.

Section 3 describes computational results starting with the condensation curve for molten BSE material over the  $10^{-8}$  to  $10^2$  bar range. Next is a discussion of condensation of the major, minor, and trace elements in BSE material and effects of variable activity coefficients upon condensation temperatures.

Section 4 discusses condensation temperatures in silicate vapor and solar composition material and differences between computed and actual condensation and evaporation temperatures due to evaporation (condensation) coefficients. Section 5 summarizes the work.

Preliminary results of this work were published earlier in two abstracts and one paper (Fegley and Lodders, 2017, 2021; Fegley et al., 2020).

# 2. Computational methods and data sources

# 2.1. Overview

Different sets of chemical equilibrium calculations for BSE material were done using the CONDOR code at Washington University and the FactSage code at the NASA Glenn Research Center. The FactSage code was also used to compute some of the activity coefficients used in the CONDOR code. The CONDOR code is described and used in several prior papers (e.g., Lodders and Fegley, 1993; Fegley and Lodders, 1994; Lodders, 2003). CONDOR is a mass-balance, mass-action code that computes gas phase and gas – condensed phase chemical equilibrium as a function of temperature, pressure, elemental abundances, and thermodynamic data. CONDOR includes thermal ionization and non-ideal molten oxide solutions. Validation examples and references to other papers using the code are at the Planetary Chemistry Laboratory website (http://solarsystem.wustl.edu/research/condor/).

The CONDOR code was used to compute 50% condensation temperatures (i.e., half of an element in the gas and half in the melt), gas phase and gas – melt chemical equilibria from  $10^{-6}$  to  $10^2$  bar total pressure for 69 elements: Li, Na, K, Rb, Cs; Be, Mg, Ca, Sr, Ba; Sc, Y; La, Ce, Pr, Nd, Sm, Eu, Gd, Tb, Dy, Ho, Er, Tm, Yb, Lu; Ti, Zr, Hf; V, Nb, Ta; Cr, Mo, W; Mn, Re; Fe, Ru, Os; Co, Rh, Ir; Ni, Pd, Pt; Cu, Ag, Au; Zn, Cd, Hg; B, Al, Ga, In, Tl; Si, Ge, Sn, Pb; P, As, Sb, Bi; O; Th, U, Pu in a dry model of BSE composition based on Palme and O'Neill (2014) and Hudson et al. (1989) for the  $^{244}$ Pu/ $^{238}$ U ratio of 0.0068. Calculations were done with 1 K temperature steps and  $\leq$ 0.5 log P pressure steps. The dry model excludes the volatile elements (H, C, N, F, Cl, Br, I, S, Se, Te), which will be included in a separate set of calculations called the wet

model. This was done because the solubilities and activities of volatile elements in silicate melts are not well known, but must be considered because hydrogen, carbon, nitrogen, sulfur, selenium, tellurium and halogens are soluble (to varying extent) in silicate melts. Preliminary results of the wet model calculations for a few elements, whose chemistry is similar in the dry and wet models, are presented here. Elements that are not considered are the noble gases (He, Ne, Ar, Kr, Xe), and the following radioactive elements: Tc (43) Pm (61), Po (84), At (85), Rn (86), Fr (87), Ra (88), Ac (89), Pa (91), and Np (93). Plutonium (94) is considered because <sup>244</sup>Pu is a short-lived (82 Ma half-life) radionuclide present in the early solar system and it is important for Pu – I – Xe dating of meteorites and of the Earth – Moon system (Hudson et al., 1989; Avice and Marty, 2014). Table 1 summarizes compositions of the dry and wet models.

The FactSage thermochemical modeling software package (Bale et al., 2002, 2009, 2016) was used to calculate thermodynamic activities and condensation temperatures in solution using the modified quasichemical model. The liquid/glass solution phase of the FToxid-Slag Database was used. This includes Al, As, B, Ca, Co, Cr, Cu, Fe, Ge, K, Li, Mg, Mn, Na, Ni, P, Pb, Si, Sn, Ti, Zn + dilute S and F (Miscibility gap at high SiO<sub>2</sub>). The core system of this phase is Al<sub>2</sub>O<sub>3</sub>-CaO-FeO-Fe<sub>2</sub>O<sub>3</sub>-MgO-SiO<sub>2</sub> and "has been optimized from 25 °C to above the liquidus temperatures at all compositions and oxygen partial pressures" (Bale et al., 2009). Numerous other oxides are included in this database, and it is optimized for industrial slags such as an iron blast furnace slag or a copper smelting slag. The database is extrapolated/interpolated to a separate set of conditions in this study. A comparison of compositions of industrial slags, molten BSE, and molten continental crust shows there is some overlap (Table 3 of Fegley et al., 2020). Compositionally the extrapolation/interpolation is reasonable. For example, Fegley et al. (2016) compared activities at 2000 K for SiO2, MgO, CaO, Al2O3, and FeO computed from the MELTS and the FactSage codes for molten BSE and molten continental crust and found agreement, except for alumina

**Table 1**Composition model for the Bulk Silicate Earth (BSE). a,b

Oxide	Mol%	Oxide	Mol%
MgO	47.67	Rb <sub>2</sub> O	$1.8\times10^{-5}$
SiO <sub>2</sub>	39.48	$La_2O_3$	$1.3  imes 10^{-5}$
FeO	5.90	$Dy_2O_3$	$1.2\times10^{-5}$
CaO	3.40	$Gd_2O_3$	$9.7 \times 10^{-6}$
$Al_2O_3$	2.30	$HfO_2$	$8.8 \times 10^{-6}$
Na <sub>2</sub> O	0.29	$Sm_2O_3$	$7.5 \times 10^{-6}$
NiO	0.17	$Er_2O_3$	$7.3 imes10^{-6}$
$TiO_2$	0.14	$Yb_2O_3$	$7.2  imes 10^{-6}$
$Cr_2O_3$	0.13	SnO	$6.2  imes 10^{-6}$
MnO	0.10	$Pr_2O_3$	$4.9 \times 10^{-6}$
K <sub>2</sub> O	$1.74 \times 10^{-2}$	PbO	$4.7 \times 10^{-6}$
CoO	$9.1 \times 10^{-3}$	$Eu_2O_3$	$2.9 \times 10^{-6}$
$P_2O_5$	$7.3 \times 10^{-3}$	$MoO_3$	$2.6 \times 10^{-6}$
$V_2O_3$	$4.4  imes 10^{-3}$	$Ho_2O_3$	$2.5\times10^{-6}$
ZnO	$4.3 imes10^{-3}$	$As_2O_3$	$2.4\times10^{-6}$
SrO	$1.3  imes 10^{-3}$	$ThO_2$	$1.9\times10^{-6}$
$Sc_2O_3$	$9.6\times10^{-4}$	$Tb_2O_3$	$1.8\times10^{-6}$
Cu <sub>2</sub> O	$8.2\times10^{-4}$	CdO	$1.6\times10^{-6}$
Li <sub>2</sub> O	$6.0 \times 10^{-4}$	$Tm_2O_3$	$1.1\times10^{-6}$
ZrO <sub>2</sub>	$5.9\times10^{-4}$	$Lu_2O_3$	$1.1\times10^{-6}$
BaO	$2.6 \times 10^{-4}$	$Ta_2O_5$	$6.2  imes 10^{-7}$
$Ga_2O_3$	$1.6 \times 10^{-4}$	$UO_2$	$5.0  imes 10^{-7}$
$Y_2O_3$	$1.2  imes 10^{-4}$	$In_2O_3$	$4.1 \times 10^{-7}$
$B_2O_3$	$6.3 \times 10^{-5}$	Cs <sub>2</sub> O	$3.5\times10^{-7}$
$GeO_2$	$8.6\times10^{-5}$	$WO_3$	$3.4 \times 10^{-7}$
BeO	$3.6 \times 10^{-5}$	Ag <sub>2</sub> O	$1.5\times10^{-7}$
$NbO_2$	$3.3 \times 10^{-5}$	$Sb_2O_3$	$1.2\times10^{-7}$
$Ce_2O_3$	$3.3 imes10^{-5}$	$Tl_2O$	$5.2  imes 10^{-8}$
$Nd_2O_3$	$2.4\times10^{-5}$	$Bi_2O_3$	$3.7\times10^{-8}$

<sup>&</sup>lt;sup>a</sup> Calculated from Palme and O'Neill (2014).

 $<sup>^</sup>b$  The molar percentages of volatiles in the wet BSE model are 0.31  $\rm H_2O,0.044$  CO<sub>2</sub>, 0.0326 S, 6.9  $\times$  10 $^{-3}$  F, 4.4  $\times$  10 $^{-3}$  Cl, 4.9  $\times$  10 $^{-6}$  Br, 3.0  $\times$  10 $^{-7}$  I,7.5  $\times$  10 $^{-4}$  N, 5.0  $\times$  10 $^{-6}$  Se, 4.0  $\times$  10 $^{-7}$  Te, and 1.6  $\times$  10 $^{-6}$  Hg.

where FactSage gave a( $Al_2O_3$ ) about 100 times smaller than the value from MELTS, which does not include a MgAl $_2O_4$  liquid component. Extrapolations in temperature and pressure are more extreme in the present work. However, as discussed later, the agreement between activity coefficients from FactSage and other models suggests these extrapolations/interpolations are reasonable.

Thermodynamic activities of the melt components are part of the equilibrium solution parameters in FactSage. Model parameters are from many assessments of experimental data and standard solution models, as described in publications on the database (Bale et al., 2002, 2009, 2016). Condensation temperatures were calculated in the "Equilib" module. This is the FactSage free energy minimizer, which calculates the equilibrium products under a given set of conditions. Using the "Formation Target Phase" option, the module steps through temperature until the selected phase (Slag in our case) first appears.

The CONDOR and FactSage codes were used to calculate the condensation curve for the six most abundant oxides (thus the seven most abundant elements) in the BSE according to the compilation of Palme and O'Neill (2014). These six oxides are MgO, SiO<sub>2</sub>, FeO, CaO, Al<sub>2</sub>O<sub>3</sub>, and Na<sub>2</sub>O, which are the bold-face entries in Table 1. CONDOR code calculations using all elements included in the dry BSE model give the same condensation temperatures as the seven-element (six oxide) model. This occurs because the additional elements are less abundant than those in the seven-element model and do not significantly alter the oxygen fugacity. The results of the calculations and comparisons to prior work are in the Results and Discussion sections.

#### 2.2. Thermodynamic data sources for pure materials

The calculations for dry BSE material use thermodynamic data for the elements, and their oxides (e.g., the Li-bearing gases in the dry model are Li, Li $^+$ , Li $^-$ , Li $^2$ , Li $^+$ , LiNa, LiNaO, LiK, LiRb, LiBO $_2$ , LiO, Li $_2$ O, Li $_2$ O, 2 and the Li-bearing condensed phase in the code is Li $_2$ O). The wet BSE model calculations also use thermodynamic data for any gases formed with the volatiles H, C, N, F, Cl, Br, I, S, Se, and Te (e.g., the additional Li-bearing gases in the wet model are LiH, LiBeF $_3$ , LiN, LiNO, LiNO $_2$ , LiNO $_3$ , LiOH, LiOH $^+$ , Li $_2$ (OH) $_2$ , Li $_2$ SO $_4$ , LiF, Li $_2$ F $_2$ , Li $_3$ F $_3$ , LiFO, LiCl, Li $_2$ Cl $_2$ , Li $_3$ Cl $_3$ , LiClO, Li $_2$ ClF, LiBr, Li $_2$ Br $_2$ , Li $_3$ Br $_3$ , LiI, Li $_2$ I $_2$ , and Li $_3$ I $_3$ ).

The data for the compounds included in the calculations are those tabulated in standard compilations, e.g., the NIST-JANAF Tables (Chase, 1998), the US Geological Survey tables (Robie and Hemingway, 1995), Schick (1966), and the FactSage and IVTAN code databases described elsewhere (Bale et al., 2002, 2009, 2016; Belov et al., 1999; Glushko et al., 1982; Gurvich et al., 1989). The IVTAN thermodynamic database is the Russian counterpart of the NIST-JANAF Tables and is from the Joint Institute for High Temperatures of the Russian Academy of Sciences. It has the advantage of continual updates that include newer experimental studies that are not in the NIST-JANAF Tables, e.g., Aristova et al. (2018) on solid and liquid uranium dioxide. The published tables give book length discussions of data evaluation methods with extensive literature citations (Gurvich et al., 1989). Additional data sources are given in the text as needed when discussing particular compounds.

# 2.3. Molten oxide solution modeling

Magnesium exemplifies an element condensing as a single oxide into a non-ideal multicomponent oxide melt and copper exemplifies a multivalent element that can condense as two oxides into a non-ideal multicomponent oxide melt. Ideal gas chemical equilibria are used because as discussed later, the virial equation of state shows silicate vapor is ideal within  $\leq 2\%$  in the P – T range considered.

# 2.3.1. Condensation as a single oxide

The silicate vapor - melt equilibrium for magnesium is.

$$Mg (gas) + \frac{1}{2} O_2 (gas) = MgO (melt)$$
 (1)

The equilibrium constant  $K_1$  for reaction Eq. (1) is

$$K_1 = \frac{a_{MgO}}{P_{Mg}P_{Os}^{1/2}}$$

The partial pressure of gaseous Mg in equilibrium with the melt is  $P_{Mg}$ ,  $a_{MgO}$  is the thermodynamic activity of liquid MgO dissolved in the oxide melt, and  $P_{O_2}^{-1/2}$  is the square root of the  $O_2$  gas partial pressure (not  $P_O$ , which is completely different). Hence the equilibrium partial pressure of Mg over the oxide melt is

$$P_{Mg} = \frac{a_{MgO}}{K_1 P_{O_2}^{1/2}}$$

Now consider how the equilibrium partial pressure of Mg over the melt relates to the total amount of magnesium in the system, denoted  $S_{Mg}$  for sum magnesium. The total amount  $S_{Mg}$  is comprised of magnesium in the gas phase (denoted  $S_{G}$  for sum gas) and magnesium condensed as liquid MgO in the oxide melt (denoted  $S_{C}$  for sum condensed)

$$S_{Mg} = S_C(Mg) + S_G(Mg) \label{eq:SMg}$$

The fraction of magnesium condensed in the melt is  $\alpha_{Mg}$ ,

$$\alpha_{Mg} = \frac{S_C(Mg)}{S_{Mg}}$$

and the fraction of total magnesium in the gas is thus  $(1 - \alpha_{Mg})$ ,

$$\left(1-\alpha_{Mg}\right) = \frac{S_G(Mg)}{S_{Mg}}$$

Monatomic Mg and all other Mg-bearing gases, in decreasing order of abundance, in dry silicate vapor are in the  $S_G$  term,

$$S_G(Mg) = P_{Mg} + P_{Mg^+} + P_{Mg^{2+}} + P_{MgO} + 2P_{Mg_2} \label{eq:sg}$$

The mass balance sum is more complex in wet silicate vapor, e.g., at 3415 K (the 50% condensation temperature at one bar total pressure), the nine most abundant Mg-bearing gases in decreasing order of abundance are

$$S_G(Mg)\!=\!P_{Mg}\!+\!P_{MgO}\!+\!P_{MgOH}\!+\!P_{MgF}\!+\!P_{MgCl}\!+\!P_{Mg^+}\!+\!P_{MgH}\!+\!P_{MgS}\!+\!P_{Mg(OH)_2}\!+\!\cdots$$

The entire mass balance sum contains 28 gases, but Mg and MgO are the two major ones, and all other gases combined are <0.1% of total gaseous magnesium.

The variable  $\beta_{\text{Mg}}$  is the fraction of total gaseous magnesium present as monatomic Mg (gas); this is

$$\beta_{Mg} = \frac{P_{Mg}}{S_G(Mg)}$$

Using  $\beta_{Mg}$  to substitute into the expression for  $K_1$  gives

$$K_1 = \frac{a_{MgO}}{P_{Mg}P_{O_2}^{1/2}} = \frac{a_{MgO}}{\beta_{Mg} \bullet S_G(Mg) \bullet P_{O_2}^{1/2}}$$

Using the definition of (1  $-\alpha_{\mbox{\scriptsize Mg}})$  – the fraction of total Mg in the gas – one can write

$$\left(1-\alpha_{Mg}\right) = \frac{a_{MgO}}{K_1 \bullet \beta_{Mg} \bullet S_G(Mg) \bullet P_{O_2}^{1/2}} \frac{1}{S_{Mg}}$$

The code calculates gas chemistry for a given MgO activity and  $\rm O_2$  partial pressure, which means that  $\rm S_G$  (Mg) is computed. This is one of the iterative procedures in the code.

The MgO activity controls the amount of MgO condensed into the oxide melt because the MgO activity is the product of the MgO mole fraction (X) and activity coefficient  $(\gamma)$ ,

$$a_{MgO} = X_{MgO} \bullet \gamma_{MgO}$$

The activity coefficient is unity ( $\gamma=1$ ) for an ideal solution. Negative deviations from ideality mean  $\gamma<1$  and positive deviations from ideality mean  $\gamma>1$ . Calculation of activity coefficients is described in another section below.

The MgO mole fraction is the condensed moles of MgO  $(N_{MgO})$  divided by the sum of the moles of all other species (all oxides in this case) in the melt,

$$X_{MgO} = \frac{N_{MgO}}{N_{MgO} + N_{SiO_2} + N_{Al_2O_3} + N_{CaO} + N_{Na_2O} + \cdots} \label{eq:XMgO}$$

This is equivalent to

$$X_{MgO} = \frac{\alpha_{Mg} S_{Mg}}{\alpha_{Mg} S_{Mg} + \sum \nu_{i \neq Mg}^{-1} \alpha_i S_i} \label{eq:mgO}$$

The summation term in the denominator includes all cationic elements (Al, Ca, Si, Fe, ...) other than Mg in the melt. The moles of the other cationic elements are expressed by their fraction condensed  $\alpha_i$  times their respective total abundance  $S_i$  with  $\nu_i$  being the stoichiometric coefficient of the cation in the oxide formula, e.g., for Al<sub>2</sub>O<sub>3</sub>,  $\nu_{Al}=2$  for mass balance. The condition that all mole fractions sum to unity is another constraint used by the code, i.e.,

$$X_{MgO} + X_{SiO_2} + X_{Al_2O_3} + X_{Na_2O} + \cdots = 1 \label{eq:constraint}$$

Rewriting the  $X_{MgO}$  equation to explicitly include the MgO activity coefficient and to solve for  $1/S_{Mg}$ ,

$$\frac{1}{S_{Mg}} = \frac{\alpha_{Mg} \left(1 - X_{MgO}\right)}{X_{MgO} \sum v_{i \neq Mg}^{-1} \alpha_i S_i} = \frac{\gamma_{MgO} \; \alpha_{Mg} \left(1 - X_{MgO}\right)}{a_{MgO} \sum v_{i \neq Mg}^{-1} \alpha_i S_i}$$

Substituting this equation into the prior one for (1  $-\alpha_{\mbox{\scriptsize Mg}}$  ), the fraction of Mg in the gas,

$$\left(1-\alpha_{Mg}\right) = \frac{S_G(Mg)}{S_{Mg}} = \frac{\gamma_{MgO} \ \alpha_{Mg} \left(1-X_{MgO}\right)}{a_{MgO} \sum v_i^{-1} \alpha_i S_i} \cdot S_G(Mg)$$

This equation shows the connection between gas phase and melt chemistry and shows how the activity coefficient of MgO affects its chemistry. Going back to the mole fraction sum shows that the activity coefficient of any oxide also affects the chemistry of all other oxides

$$X_{MgO} + X_{SiO_2} + X_{Al_2O_3} + X_{Na_2O} + \cdots = 1$$

$$\frac{a_{MgO}}{\gamma_{MgO}} + \frac{a_{SiO_2}}{\gamma_{SiO_2}} + \frac{a_{Al_2O_3}}{\gamma_{Al_2O_3}} + \frac{a_{Na_2O}}{\gamma_{Na_2O}} \dots = 1$$

All chemical equilibrium calculations must preserve mass balance; thus, the effects of varying the activity coefficient of a single melt constituent upon the chemistry of all other melt constituents is always apparent in *all* calculations of multicomponent melt chemistry. Experimental studies of the effects of  $SiO_2$  and  $Al_2O_3$ , the two most abundant acidic oxides in melts, upon solubilities of alkali oxides  $M_2O$  (M=Na,K,Rb) in the  $CaO-Al_2O_3-SiO_2$  (CAS) and the CAS-MgO (CMAS) systems by Borisov (2009) demonstrate this interdependence, and show

$$\left(\frac{\partial a_{M_2O}}{\partial X_{SiO_2}}\right)_{P,T} > \left(\frac{\partial a_{M_2O}}{\partial X_{Al_2O_3}}\right)_{P,T}$$

in ultramafic melts, but the reverse in felsic melts.

This interdependence is a consequence of the Gibbs – Duhem equation, which constrains the covariance of thermodynamic potentials, volume, entropy, activities, and activity coefficients, of the components in *any* solution (see chapter 34 of Pitzer and Brewer, 1961)

$$X_1dln\gamma_1+X_2dln\gamma_2+X_3dln\gamma_3+\cdots=0$$

This equation shows the activity coefficient of a species in a ternary or multicomponent solution can increase or decrease upon change of concentration of another species in the solution. Figs. 4–7 of Borisov

(2009), Fig. 31 of Kubaschewski and Alcock (1979), and Fig. 34–1 of Pitzer and Brewer (1961) illustrate this point. In practical terms the Gibbs — Duhem equation means that changing the activity coefficient for a single abundant species can affect the fraction condensed of other species with similar or smaller abundances. Conversely, changes in activity coefficients for trace species (e.g., CdO) have insignificant effects on condensation of more abundant oxides (e.g., MgO).

Rearranging the  $(1 - \alpha_{Mg})$  equation again yields the "key" equation for the fraction of magnesium condensed,

$$\alpha_{Mg} = \frac{a_{MgO} \sum v_{i \neq Mg}^{-1} \alpha_i S_i}{\gamma_{MgO} \; S_G(Mg) \; \left(1 - X_{MgO}\right) + a_{MgO} \sum v_{i \neq Mg}^{-1} \alpha_i S_i}$$

Generalizing, the "key" equation for any metal (metalloid) M that dissolves in a multicomponent melt as a single constituent, e.g., Si as  $SiO_2$ , Al as  $Al_2O_3$ , Na as  $Na_2O$ , and so on,

$$\alpha_{M} = \frac{a_{M_{v(M)}O_{x}} \sum v_{i}^{-1}\alpha_{i}S_{i}}{\gamma_{M_{v(M)}O_{x}} \; S_{G(M)} \left(1 - X_{M_{v(M)}O_{x}} \right) + a_{M_{v(M)}O_{x}} \sum v_{i}^{-1}\alpha_{i}S_{i}} \; \; \text{with} \; (i \neq M)$$

The code solves this equation iteratively for each element considered in the system. The coupled gas chemistry and melt composition link the equations. The required inputs for the calculations are temperature, total pressure, elemental abundances of the system, and activity coefficients as well as the usual basic thermodynamic properties of the elements and their gaseous, liquid, and solid compounds.

If only tiny amounts of element M condense into a melt such that  $X_{M_{v}}$   $_{(00)}o_{x}\ll 1$ , then

$$\left(1 - X_{M_{v(M)}O_x}\right) \approx 1$$

And the expression for  $\alpha_M$  simplifies to

$$\alpha_{M} \approx \frac{a_{M_{\nu(M)}O_{X}} \sum v_{i}^{-1}\alpha_{i}S_{i}}{\gamma_{M_{\nu(M)}O_{X}} S_{G(M)} + a_{M_{\nu(M)}O_{X}} \sum v_{i}^{-1}\alpha_{i}S_{i}} \ \ \text{with} \ (i \neq M)$$

This equation is a useful approximation for quick estimates of trace element condensation into a liquid host phase made of one or more major elements, e.g., a melt in the CMAS system made of CaO, MgO, Al<sub>2</sub>O<sub>3</sub>, and SiO<sub>2</sub>; and a trace element such as zinc.

# 2.3.2. Condensation as two oxides with different oxidation states

Copper exemplifies multivalent elements that may exist in two different oxidation states with different activity coefficients in oxide melts (Paul, 1990). These multivalent elements include Ti, V, Nb, Cr, Mo, W, Mn, Fe, Cu, In, Tl, Ge, Sn, Pb, As, Sb, Bi, Ce, Pr, Eu, U, and Pu. The basic variables are the sum of copper in the gas  $S_G(Cu)$ , the sum of condensed copper  $S_C(Cu)$ , and total copper  $S_{Cu}$ , which is the sum of  $S_G(Cu)$  plus  $S_C(Cu)$ . In dry silicate vapor,  $S_G(Cu)$  has only six terms; in decreasing order of abundance at the 50% condensation temperature (3127 K at 1 bar total P),

$$S_G(Cu) = P_{Cu} + P_{CuO} + 2P_{Cu_2} + P_{Cu^-} + P_{Cu^+} + P_{Cu^{2+}} \label{eq:sg}$$

However, total gaseous copper is almost 100% monatomic Cu with percent levels of CuO and trace amounts of all other Cu gases at temperatures where copper condenses into the oxide melt. The  $S_G(Cu)$  expression contains 18 species in wet silicate vapor because Cu-bearing halide, hydride, selenide, and sulfide gases are present. At the 50% condensation temperature of 2025 K (1 bar  $P_{Total}$ ) the seven most abundant Cu gases (decreasing order of abundance) in  $S_G(Cu)$  are

$$S_G(Cu) = P_{Cu} + P_{CuS} + P_{CuH} + P_{CuCl} + P_{CuF} + P_{CuSe} + 2P_{Cu_2}$$

Monatomic Cu again dominates but is only 62% of  $S_G(Cu)$  with CuS (20%) and CuH (16%) making up most of the rest. Of course, the gas phase speciation varies with P and T and this distribution at 2025 K and 1 bar total P is only illustrative. Holzheid and Lodders (2001) found no evidence for sulfidic dissolution of copper, and it was not considered in

the wet model calculations.

The sum of condensed copper is the number of moles (N) of liquid CuO plus liquid  $Cu_2O$ ,

$$S_C(Cu) = N_C(Cu) = N_{CuO} + 2N_{Cu \cdot O}$$

The fraction condensed  $\alpha_{Cu}$  of total copper is

$$\alpha_{Cu} = \frac{S_{C}(Cu)}{S_{Cu}} = \frac{N_{C}(Cu)}{S_{Cu}} = \frac{N_{CuO} + 2N_{Cu_{2}O}}{S_{Cu}}$$

And the fraction of total copper left in the gas is

$$(1-\alpha_{Cu}) = \frac{S_G(Cu)}{S_{Cu}} = \frac{P_{Cu} + P_{CuO} + \cdots}{S_{Cu}} \cong \frac{a_{Cu_2O}}{K_{Cu}a_{CuO}} \frac{1}{S_{Cu}}$$

If Cu is the only important gas, then  $S_G(Cu)=P_{Cu}$ , otherwise other gases also must be considered as done above. The coexistence of CuO and Cu<sub>2</sub>O dissolved in the melt regulates  $P_{Cu}$  via

$$CuO(melt) + Cu(gas) = Cu_2O(melt)$$

$$K_{Cu} = \frac{a_{Cu_2O}}{a_{CuO}}\,\frac{1}{P_{Cu}}$$

The mole fractions of CuO and Cu2O in the melt are

$$X_{Cu_2O} = \frac{N_{Cu_2O}}{N_{Cu_2O} + N_{CuO} + N_{MgO} + N_{SiO_2} + N_{Al_2O_3} + \cdots} = \frac{N_{Cu_2O}}{\sum v_i^{-1} \alpha_i S_i}$$

$$X_{CuO} = \frac{N_{CuO}}{N_{Cu_2O} + N_{CuO} + N_{MgO} + N_{SiO_2} + N_{Al_2O_3} + \cdots} = \frac{N_{CuO}}{\sum v_i^{-1} \alpha_i S_i}$$

The summation term includes all melt constituents (including CuO and  $\text{Cu}_2\text{O}$ ).

Because the activities of CuO and Cu<sub>2</sub>O are the product of their mole fractions and activity coefficients, one can rewrite the equation for  $\alpha_{Cu}$  as follows

$$\alpha_{Cu}S_{Cu} = 2N_{Cu_2O} + N_{CuO} = 2X_{Cu_2O} \sum v_i^{-1}\alpha_iS_i + X_{CuO} \sum v_i^{-1}\alpha_iS_i$$

Rearranging to solve for  $(S_{Cu})^{-1}$ ,

$$\frac{1}{S_{Cu}} = \frac{\alpha_{Cu}}{(2X_{Cu_2O} + X_{CuO}) \sum v_i^{-1} \alpha_i S_i} = \frac{\alpha_{Cu}}{\left(2\frac{a_{Cu_2O}}{\gamma_{Cu_2O}} + \frac{a_{CuO}}{\gamma_{Cu_2O}}\right) \sum v_i^{-1} \alpha_i S_i}$$

Inserting this into the equation for (1  $-\alpha_{\text{Cu}}$ ) and rearranging gives,

$$\alpha_{Cu} = \frac{\left(2a_{Cu_2O}\gamma_{Cu_2O} + a_{CuO}\gamma_{CuO}\right)\sum v_i^{-1}\alpha_iS_i}{\gamma_{Cu_2O}\gamma_{Cu_O}S_{G(Cu)} + \left(2a_{Cu_2O}\gamma_{CuO} + a_{CuO}\gamma_{Cu_2O}\right) \bullet \sum v_i^{-1}\alpha_iS_i}$$

The generalized equation for an oxide pair of metal (metalloid) M with formulas  $M_{\nu m1}O_{\nu o1}$  and  $M_{\nu m2}O_{\nu o2}$  and an exchange equilibrium between gas and melt analogous to that for copper is

$$\nu_{o1} M_{\nu m2} O_{\nu o2}(melt) + uM(gas) = \nu_{o2} M_{\nu m1} O_{\nu o1}(melt)$$

$$u = (\nu_{m1} \upsilon_{o2} - \nu_{m2} \nu_{o1})$$

The generalized version of the  $\alpha_{Cu}$  equation is

$$\alpha_{M}\!=\!\!\frac{\left(\nu_{m_{1}}a_{M_{\nu m_{1}}O_{\nu o_{1}}}\gamma_{M_{\nu m_{1}}O_{\nu o_{1}}}\!+\!a_{M_{\nu m_{2}}O_{\nu o_{2}}}\gamma_{M_{\nu m_{2}}O_{\nu o_{2}}}\right)\sum v_{i}^{-1}\alpha_{i}S_{i}}{\gamma_{M_{\nu m_{1}}O_{\nu o_{1}}}\gamma_{M_{\nu m_{2}}O_{\nu o_{2}}}\!+\!a_{M_{\nu m_{1}}O_{\nu o_{1}}}\!+\!a_{M_{\nu m_{2}}O_{\nu o_{2}}}\!+\!a_{M_{\nu m_{2}}O_{\nu o_{2}}}\gamma_{M_{\nu m_{1}}O_{\nu o_{1}}}\right)\sum v_{i}^{-1}\alpha_{i}S_{i}}$$

In principle, elements with two or more valence states can form various oxide pairs depending on oxygen fugacity and temperature. For example, Mn can form oxides in five oxidation states (2+, 3+, 4+, 6+,and 7+). However, there is a maximum of two stable coexisting oxides with different valence states that can simultaneously dissolve in the melt, such as  $Ce_2O_3/CeO_2$ ,  $CrO/Cr_2O_3$ ,  $CuO/Cu_2O$ ,  $EuO/Eu_2O_3$ ,  $FeO/Fe_2O_3$ ,  $TiO/Ti_2O_3$  or  $Ti_2O_3/TiO_2$ . If an element has more than two valence states, the oxide pairs with the highest thermochemical activity are usually the ones that dissolve; these oxides always have neighboring valence states (e.g., 3+ and 4+ but not 3+ and 5+ if 4+ exists). As a

corollary, the oxide pair dissolving will also be the one that gives the maximum amount of element condensed. The activities of these oxides can be calculated (provided reliable thermodynamic data exists), but there are no tabulated data for some oxides such as GeO (s,liq) and data for other liquid oxides with high melting points are estimates of uncertain reliability such as CuO (liq). The CONDOR code computes activities of the following liquid oxides of multivalent elements: CeO<sub>2</sub>, Ce<sub>2</sub>O<sub>3</sub>; CuO, Cu<sub>2</sub>O; EuO, Eu<sub>2</sub>O<sub>3</sub>; FeO, Fe<sub>2</sub>O<sub>3</sub>, Fe<sub>3</sub>O<sub>4</sub>; MnO, Mn<sub>3</sub>O<sub>4</sub>; MoO<sub>2</sub>, MoO<sub>3</sub>; NbO, NbO<sub>2</sub>, Nb<sub>2</sub>O<sub>5</sub>; SnO, SnO<sub>2</sub>; TiO, Ti<sub>2</sub>O<sub>3</sub>, Ti<sub>3</sub>O<sub>5</sub>, Ti<sub>4</sub>O<sub>7</sub>, TiO<sub>2</sub>; Tl<sub>2</sub>O, Tl<sub>2</sub>O<sub>3</sub>; and VO, V<sub>2</sub>O<sub>3</sub>, V<sub>2</sub>O<sub>4</sub>, V<sub>2</sub>O<sub>5</sub>. These calculations are discussed later.

#### 2.4. Activities and activity coefficients

The Raoultian activity  $(a_i)$  of a solid or liquid evaporating to an ideal gas is the ratio of its partial pressure  $(P_i)$  divided by its saturated vapor pressure  $(P_i^{\circ})$  at the same temperature,

$$a_i = \frac{P_i}{P_i^o}$$

The activity of a pure solid or liquid is unity, while the activity of a species in a solid or liquid solution is proportional to its concentration in the solution. The proportionality constant is the activity coefficient  $(\gamma_i)$  which is the ratio of activity  $(a_i)$  divided by concentration  $(X_i)$ 

$$\gamma_i = \frac{a_i}{X_i}$$

An ideal solution has  $\gamma=1$  and non-ideal solutions have  $\gamma<1$  (negative deviations from ideality) or  $\gamma>1$  (positive deviations from ideality). Compound formation between two oxides, such as MgSiO\_3 in the MgO - SiO\_2 system, requires  $\gamma<1$  while unmixing into two liquids such as in the NaCl - albite system (Koster van Groos and Wyllie, 1969) requires  $\gamma>1$ . Activity coefficients <1 give higher condensation temperatures than for ideal solutions. Activity coefficients >1 give lower condensation temperatures than for ideal solutions.

# 2.5. Temperature dependence and extrapolation of activity coefficients

Activity coefficients trend toward unity (ideality) with increasing temperature and the general equation describing the temperature dependence of activity coefficients (Gaskell, 1973) is

$$\left[\frac{\partial ln\gamma_{i}}{\partial(1/T)}\right]_{P,n} = \frac{\overline{H}_{i}^{E}}{R}$$

The subscripts P and n (the number of moles) denote differentiation at constant pressure and constant composition and the enthalpy term is the *excess* partial molal enthalpy of mixing for any species in a solution. Converting to base 10 logs and rearranging gives an equation like that below for CaO,

$$log_{10}\gamma_{CaO}(MAGMA) = -0.144 - \frac{4656.5}{T}$$

The temperature dependence of activity coefficients for a regular solution is (Charles, 1967),

$$\left[\frac{\partial ln\gamma_{i}}{\partial(1/T)}\right]_{R,n} = \frac{\overline{H}_{i}^{E}}{R} = Tln\gamma_{i,T} = T \cdot 2.303 \cdot log\gamma_{i,T}$$

In this case the intercept term is zero and the temperature dependence is an equation like

$$\textit{log}_{10}\gamma_{MnO}(BanYa) = \frac{672.096}{T}$$

Table 2 Activity coefficients (log<sub>10</sub>  $\gamma = A + B/T$ ).

Oxide	A	В	Notes
Ag <sub>2</sub> O	0	-582	Regular solution 1673 K point, Sossi et al. (2019)
	0	3582.8	Set = $\gamma(Cu_2O)$ , Sossi et al. (2019)
$Al_2O_3$	0	-6253.138	Ban-Ya (1993)
	-0.938 $-12.515$	720.9	MAGMA code
$As_2O_3$	-12.515 3.4014	19,111.25 -26,309.08	FactSage FactSage 1800–2200 K, CMAS+FeO
A32O3	0	-4791	Chen and Jahanshahi (2010), $\gamma$ (AsO <sub>1.5</sub> ) =
	Ü	., , , 1	0.03 at 1573 K
	0	-396.2	Chen and Jahanshahi (2010), $\gamma$ (AsO <sub>1.5</sub> ) = 0.56 at 1573 K
$B_2O_3$	-7.1517	508.158	FactSage 1800–2200 K, CMAS+FeO
$Bi_2O_3$	3.4014	$-26,\!309.08$	Set = $\gamma(As_2O_3)$ from FactSage
	0	-1251.8	Paulina et al. (2013), regular solution, 1573 K point
CaO	-0.246	-6710.736	Ban-Ya (1993)
	-0.144	-4656.5	MAGMA code
CdO	1.30	-7014.6 803.1	FactSage
	-1.23		Regular solution, liquid standard state, 1473 K point, Sossi et al. (2019)
CoO	0.303	0	FactSage BSE melt, 2000–3000 K mean $\gamma$ = 2.01 $\pm$ 0.07
CrO	0.165	601.518	FactSage
Cr <sub>2</sub> O <sub>3</sub>	-2.318	4413.29	FactSage
Cs <sub>2</sub> O	-0.083 0	-13,634.1 $-12,144.$	See text, set = $\gamma$ (Na <sub>2</sub> O) FactSage Cs <sub>2</sub> O-Na <sub>2</sub> O-SiO <sub>2</sub> ternary, Bennour et al.
	<b>J</b>		(1999), see text
CuO	4	0	Set $= 10,000$ , see text
$Cu_2O$	0	373.261	Altman (1978)
	0	3144.1	Regular solution, 1573 K point, Holzheid and Lodders (2001)
	0	3582.8	Regular solution, 1673 K point, Sossi et al. (2019)
	0	2094	Regular solution, 1923 K point, Wood and Wade (2013)
FeO	0.373	399.1	Ban-Ya (1993)
	0.025	-141.8	MAGMA code
Fo O	0.282 $-1.2867$	49.7 1336.0	FactSage FactSage
Fe <sub>2</sub> O <sub>3</sub> Ga <sub>2</sub> O <sub>3</sub>	0	-6314	Interpolated from log $\gamma$ vs OB using Al <sub>2</sub> O <sub>3</sub> and In <sub>2</sub> O <sub>3</sub>
$GeO_2$	3.669	-7886	Sossi et al. (2019)
3002	0	-1601	Regular solution, 1673 K point, Sossi et al. (2019)
	0.8692	0	$\gamma(\text{GeO}_2) = 7.4$ , FactSage
	-0.010	-580.4	$\gamma(GeO_2) = \gamma(SiO_2)$ from FactSage
$In_2O_3$	0	-6534.2	Regular solution, 1923 K point, Wood and Wade (2013)
$K_2O$	0.8218	-18,774.	pMELTS, BSE 2000-3000 K
	-1.64	-15,671.2	MAGMA code
	-1.13	-16,818.8 $-12,239$	FactSage Regular solution, 1673 K point, Sossi et al.
			(2019)
$Li_2O$	-3.1647	-7945.375	FactSage 1800–2200 K CMAS+FeO
	0	−2046 <b>.</b>	Regular solution, 1573 K point, Nassaralla and Fruehan (1992)
	0	853.7	Regular solution, 1673 K, $fO_2 = 10^{-8}$ bar point, Sossi et al. (2019)
	0	3973.	Regular solution, 1673 K, $fO_2$ = air point, Sossi et al. (2019)
MgO	0.09574	-1774.577	Ban-Ya (1993)
	0.021	-1800.3	MAGMA code
MnO	0.565	-2794.3 672.006	FactSage
MnO	0 1.068	672.096 -2787.3	Ban-Ya (1993) FactSage
$MoO_2$	0.187	681.0	Geometric mean of FeO and TiO <sub>2</sub> , Ban-Ya
$MoO_3$	0.7494	-347.091	(1993) Set $\log \gamma(MoO_3) = \log \gamma(WO_3) + \log(4)$
Na <sub>2</sub> O	1.19437	-11,521.64	Ban-Ya (1993)
	0.573	-13,034.2	MAGMA code
	-0.083	-13,634.1	FactSage
	0	-10,039	Regular solution, 1673 K point, Sossi et al. (2019)
NiO	0.352	114.05	FactSage

Table 2 (continued)

Oxide	A	В	Notes
$P_2O_5$	-12.0506	4076.293	Ban-Ya (1993)
	1.8919	$-25,\!111.69$	FactSage
	1.75	$-26,\!270$	Suito (1981)
PbO	0.7172	-1863.825	FactSage 1800-2200 K
	0	-1265	Regular solution, 1923 K point, Wood and Wade (2013)
	0	-689	$PbO(liq) = Pb(g) + 1/2O_2(g), 1673 K,$ Sossi et al. (2019)
	0	-1320	PbO (liq) = PbO (g), 1673 K, Sossi et al. (2019)
Rb <sub>2</sub> O	0	-13,400	Regular solution, 1673 K point, Sossi et al. (2019)
$Sb_2O_3$	3.4014	-26,309.08	$Set = As_2O_3$ , FactSage
SiO <sub>2</sub>	0.14730	-347.091	Ban-Ya (1993)
	-0.320	-929.6	MAGMA code
	-0.010	-580.4	FactSage
SnO	0.470	-90.4	FactSage 1800–2200 K CMAS+FeO
$SnO_2$	0.86923	0	$Set = GeO_2$ , $FactSage$
$TiO_2$	0	963.090	Ban-Ya (1993)
	-0.305	-964.6	MAGMA code
	-1.407	3073.5	FactSage
$Ti_2O_3$	-2.432	289.76	FactSage
$Tl_2O$	0	-13,145	Basicity modified Rb <sub>2</sub> O value
$Tl_2O_3$	-1.2867	1336.0	$Set = Fe_2O_3$ , FactSage
VO	0.373	399.1	$Set = FeO_{,} Ban-Ya (1993)$
$V_2O_3$	-1.1319	$-16,\!818.75$	Set = $Ti_2O_3$ , FactSage, Pistorius (2006)
$WO_3$	0.14730	-347.091	$Set = SiO_2, Ban-Ya (1993)$
ZnO	1.126	-1868.7	FactSage 1800-2200 K, CMAS+FeO
	3.624	-7061.6	E1 composition, Reyes and Gaskell (1983)
	4.161	-7488.1	1573-1823 K, Sossi et al. (2019)
	0	-51.65	MAGMA code, Visscher and Fegley (2013)

# 2.6. Oxide activity coefficients for bulk silicate Earth melts

There are no experimental measurements of oxide activity coefficients in molten BSE material, i.e., peridotite, at super-liquidus temperatures. This is not surprising given the complex composition and high liquidus temperature of dry peridotite at one bar pressure (~2000 K, Takahashi, 1986).

The CONDOR code calculations use activity coefficients from six primary sources: (1) Ban-Ya's (1993) implementation of Lumsden's (1961) quadratic solution model for molten oxides, (2) the FactSage code, a modified quasi-chemical model, (3) the MAGMA code, which is an associated solution model (Fegley and Cameron, 1987; Schaefer and Fegley, 2004), (4) regular solution extrapolation of a single activity coefficient value to higher temperature, e.g., see the discussions of Ag, Cd, Cu, Ge, and In, (5) the MELTS code (Ghiorso and Sack, 1995; Ghiorso et al., 2002) used for K, (6) consideration of optical basicity and ionic potential in periodic table groups, e.g., see the later discussions of Li, Rb, Cs, Mo, W, Ag, Cd, Cu, Ga, and Tl. Table 2 lists coefficients for the twoterm equations giving  $log_{10}$  values of activity coefficients used in the CONDOR code. As Table 2 shows, sources (1), (2), and (4) supplied most of the nominal activity coefficient values. The Lumsden - Ban-Ya quadratic solution model is described next. Details about individual activity coefficient estimates and the dependence of 50% condensation temperatures upon activity coefficients are in the Results section.

# 2.7. Molten oxide quadratic solution model

Lumsden (1961) developed a regular solution model "to calculate the thermodynamic properties of complex molten slags from those of the component binary systems. The essential features of this problem can be demonstrated by a ternary system." The two key points of his model are (1) a single interaction parameter for each cation pair and (2) regular mixing of cations (e.g., Fe<sup>2+</sup>, Fe<sup>3+</sup>, Si<sup>4+</sup>) in an oxygen ion (O<sup>2-</sup>) matrix. This is a variant of Temkin's ionic mixing model, which postulates ideal mixing of cations with other cations and ideal mixing of anions with other anions in fused salts and metallurgical slags (Temkin, 1945;

Samarin et al., 1945). The two equations that define the activity coefficient for a cation in the regular solution model are

$$\overline{G}_{i}^{E} = \overline{H}_{i}^{E} = RTln\gamma_{i}$$

$$RTln\gamma_i = \sum_{i} \alpha_{ij} N_j^2 + \sum_{i} \sum_{k} \bigl(\alpha_{ij} + \alpha_{ik} - \alpha_{jk}\bigr) N_j N_k$$

The excess partial molal Gibbs energy, and excess partial molal enthalpy of component "i" are  $\overline{G}_i^E$  and  $\overline{H}_i^E$ , respectively, the interaction energy between cations "i" and "j" is  $\alpha_{ij}$ , and  $N_i$  is the cation mole fraction, i.e.,  $N_{SiO_2}$ ,  $N_{NaO_{0.5}}$ , and so on. Although quadratic regular solution models neglect ternary and other higher order terms (Grover, 1977; Berman, 1983; Berman and Brown, 1984) they are often used, e.g., see Ghiorso et al. (1983), Ghiorso and Sack (1995).

Lumsden (1961) demonstrated the regular solution model fit data for  $Pb^{2+}O^{2-} - Bi_2^{3+}O_3^{2-}$  melts and applied it to  $FeO - Fe_2O_3 - SiO_2$  slags. Later work by other metallurgists applied Lumsden's model to multicomponent melts made of various combinations of  $Al_2O_3$ , CaO,  $Cu_2O$ , FeO,  $Fe_2O_3$ , MgO, MnO,  $Na_2O$ ,  $SiO_2$ ,  $TiO_2$ , and ZnO (e.g., Richards and Thorne, 1961; Sommerville et al., 1973; Martin and Bell, 1974; Altman, 1978; Ban-Ya and Shim, 1982; Ban-Ya et al., 1984; Nagabayashi et al., 1989; Ban-Ya, 1993). These papers show agreement between experimental data and quadratic solution modeling. The CONDOR calculations use the interaction energies and temperature-dependent equations in Tables 1–3 of Ban-Ya (1993) to compute activity coefficients for  $Al_2O_3$ , CaO, FeO, MgO, MnO,  $Na_2O$ ,  $P_2O_5$ ,  $SiO_2$ , and  $TiO_2$  in BSE melt.

#### 2.8. Ideality of BSE vapor

An important question is whether silicate vapor is ideal or non-ideal under the pressure (P) and temperature (T) conditions used in the calculations. Corrections for intermolecular forces between neutral atoms and molecules in a gas become significant as the gas density approaches that of the liquid and the ideal gas equation no longer applies. The compression factor Z quantifies the non-ideality and is the ratio of the  $PV_m$  product or the  $P/\rho_m$  quotient (where  $V_m=$  molar volume, and  $\rho_m=1/V_m=$  molar density) to RT:

$$\frac{PV_{m}}{RT} = \frac{1}{RT} \cdot \frac{P}{\rho_{m}} = Z = 1 + \frac{B(T)}{V_{m}} + \frac{C(T)}{V_{m}^{2}} + \frac{D(T)}{V_{m}^{3}} + \cdots$$

The compression factor Z is unity for an ideal gas (i.e., with attractive and repulsive forces in balance), is greater than unity for an incompressible real gas (repulsive forces are dominant) and is less than unity for a highly compressible real gas (attractive forces are dominant).

The equation above is the virial equation of state (EOS), which has a sound theoretical foundation (Hirschfelder et al., 1964; Mason and Spurling, 1969). The B(T), C(T), and D(T) in the virial EOS are the second, third and fourth virial coefficients (henceforth virials) respectively. The first virial is unity and is the ideal gas term. The second virial B arises from interactions between two gas molecules. The third virial C arises from interactions between three gas molecules, and the fourth virial D from interactions of four gas molecules and so on. The virial coefficients for reactive atoms and radicals such as atomic Fe, O, Na, and SiO can be computed from their interatomic (or intermolecular) potentials. Thus, one can rigorously compute fugacity coefficients for these reactive species – something that is not possible with empirical EOS such as the van der Waals or Redlich – Kwong equations.

The second virial is easily, the third virial less easily and the fourth virial with difficulty computed from intermolecular potentials. A common potential is the Lennard-Jones (12–6) potential energy function  $\phi(r)$  with two force constants  $\sigma$  and  $\epsilon/k$ ,

$$\phi(r) = 4\varepsilon \left\lceil \left(\frac{\sigma}{r}\right)^{12} - \left(\frac{\sigma}{r}\right)^{6} \right\rceil$$

The distance between two gas molecules (or atoms) is r,  $\boldsymbol{\sigma}$  is the

distance at which  $\varphi(r)=0$ ,  $\epsilon$  is the maximum depth of the potential energy well, and  $\epsilon/k$  is epsilon divided by Boltzmann's constant and has units of temperature. Hirschfelder et al. (1964) gives equations and tabular data for computing B(T) and C(T) for the Lennard-Jones (12–6) potential. These were used to get the numerical values of B(T) in Table 3. The maximum T and P in the calculations are 5000 K, 100 bar corresponding to  $\rho_m \simeq 2.4 \times 10^{-4}$  mol cm $^{-3}$  (about six times denser than air at room temperature). This low density allows simplification of the virial EOS to the equation below.

$$\frac{PV_m}{RT} = 1 + \frac{B(T)}{V_m}$$

The corresponding equation below gives fugacity coefficients  $\phi$  (see Chapter 16 of Pitzer and Brewer, 1961).

$$ln\left(\frac{f}{P}\right) = ln\phi = \frac{B}{RT}P$$

Table 3 gives values for the second virials and fugacity coefficients for several major gases in BSE vapor at 5000 K and 100 bar total pressure. The least ideal gases in Table 3 are sodium and silicon dioxide which are more compressible than an ideal gas (2% and 1% respectively). The other gases for which second virials are known have fugacity coefficients closer to unity. At 1500 K and 100 bar total pressure  $O_2$  is the major gas with much smaller amounts of metallic gases. Under these conditions  $B(O_2) = 25.00 \, \mathrm{cm}^3 \, \mathrm{mol}^{-1}$  and the  $O_2$  fugacity coefficient  $\phi$  of 1.02 is 2% less compressible than an ideal gas. Monatomic Hg vapor (0.15%) is the second most abundant gas with  $B(Hg) = -26.15 \, \mathrm{cm}^3 \, \mathrm{mol}^{-1}$ . The mercury fugacity coefficient of  $\phi = 0.98$  is 2% more compressible than an ideal gas. These small deviations from ideality are neglected in the chemical equilibrium calculations.

Many gases in silicate vapor have negative second virials and display negative deviations from ideality. This behavior follows directly from the characteristic temperature dependence of the second virial coefficient *B* (Mason and Spurling, 1969). Values of the second virial *B* are negative below the Boyle temperature, zero at the Boyle temperature, and positive above the Boyle temperature of a gas. The Boyle temperature is defined by the equation below.

$$\left(\frac{\partial \mathbf{Z}}{\partial \rho}\right)_{\mathrm{T}} = 0 \text{ as } \rho \rightarrow 0$$

The Boyle temperature,  $T_B$ , is greater than the critical temperature,  $T_{Crit}$ . Oxygen is a major gas in silicate vapor, and it has  $T_B = 406$  K,  $T_{Crit} = 154.58$  K, and  $T_B/T_{crit} = 2.63$ . This is the same as the  $T_B/T_{crit}$  ratio for a Lennard-Jones fluid (Apfelbaum and Vorob'ev, 2009). The critical temperatures are even higher for other species in silicate vapor; 1763  $\pm$ 

**Table 3**Second virials and fugacity coefficients at 5000 K in BSE vapor.

Gas	ε/k	σ (Å)	b <sub>o</sub> (cm <sup>3</sup> )	B(T)	ф	Reference
O <sub>2</sub>	118	3.460	52.26	26.97	1.006	НСВ
O	81.5	2.956	32.58	16.19	1.004 <sup>a</sup>	W62
SiO	569	3.374	48.45	21.07	1.005	Sv62
$SiO_2$	2954	3.706	64.21	-59.89	0.99	Sv62
Mg	1614	2.926	31.60	-2.69	0.9994	Sv62
Fe	3521	2.435	18.21	-24.39	0.994	T62
Na	8471	3.0788	36.82	-73.77	$0.98^{b}$	HB87
Hg <sup>c</sup>	851	2.898	30.70	$-26.15^{c}$	0.98 <sup>c</sup>	HCB

HCB: Hirschfelder et al. (1964). W62: Woolley (1962). Sv62: Svehla (1962). T62: Turkdogan (1962). HB87: Holland and Bilosi (1987).

<sup>&</sup>lt;sup>a</sup> Capitelli and Lamanna (1976) considered all electronic states of interacting oxygen atoms and computed  $B_{Total}=10.55~cm^3$  at 5000 K corresponding to  $\varphi=1.0005$ 

<sup>&</sup>lt;sup>b</sup> Holland and Bilosi (1987) used the Hulbert – Hirschfelder potential to compute B for Na.

 $<sup>^</sup>c\,$  At 1500 K where Hg is the 2nd most abundant gas with a mole fraction of 1.5  $\times$   $10^{-3}.$ 

15 K for Hg (Franck and Hensel, 1966), and 2497  $\pm$  15 K for Na (Ohse et al., 1985). As mentioned earlier (Fegley et al., 2020), "the critical temperatures of silica, iron, and silicates are unknown. Estimated critical temperatures for silica range from 4,700 to 13,500 K (Melosh, 2007)." More recent estimates of critical temperatures for silica and other minerals are 5200–6200 K for silica Si<sub>1.1</sub>O<sub>2</sub> - Si<sub>1.4</sub>O<sub>2</sub> (Connolly, 2016), 5500–6000 K for NaAlSi<sub>3</sub>O<sub>8</sub> and 5000–5500 K for KAlSi<sub>3</sub>O<sub>8</sub> (Kobsch and Caracas, 2020), 6240  $\pm$  200 K for Mg<sub>2</sub>SiO<sub>4</sub> from ab initio calculations (Townsend et al., 2020), 7928 K for elemental Fe using a corresponding states method (Apfelbaum and Vorob'ev, 2015), and 9250  $\pm$  700 K for Fe from rapid pulse heating experiments Pottlacher and Jäger (1996). Using the T<sub>C</sub>/T<sub>B</sub> ratio of 0.38 for a Lennard-Jones fluid (Apfelbaum and Vorob'ev, 2009), the T<sub>C</sub> estimates suggest T<sub>B</sub> values >10,000 K for constituents of silicate vapor and thus negative deviations from ideality.

# 3. Results

#### 3.1. BSE melt condensation curve

The condensation curve is the highest temperature at which melt is stable and is the boundary between unsaturated silicate vapor and condensate plus vapor. The BSE melt condensation curve was calculated (using the six-oxide model for the bulk silicate Earth, boldface entries in Table 1) with the CONDOR code at Washington University and with the FactSage code at NASA Glenn. The six-oxide model makes up more than 99% of the BSE and is the same model used in Fegley et al. (2016). As stated earlier, CONDOR code calculations using all elements in the dry BSE model give the same condensation temperatures for BSE melt as the six-oxide model. In particular, the absence of TiO $_2$  (0.14% molar abundance in the BSE) and other less abundant refractory oxides found in Ca, Al-rich inclusions in meteorites does not change the results. The TiO $_2$  content of the initially condensed BSE melt is small because TiO $_2$  is more volatile than either Al $_2$ O $_3$  or CaO in BSE melt as discussed later.

Fig. 1 displays the condensation curve for molten bulk silicate Earth (BSE) material from  $10^{-8}$  to  $10^2$  bar and compares the results from the CONDOR and FactSage codes with results from the GRAINS code (Lock et al., 2018). Table 4 lists the condensation temperatures plotted in

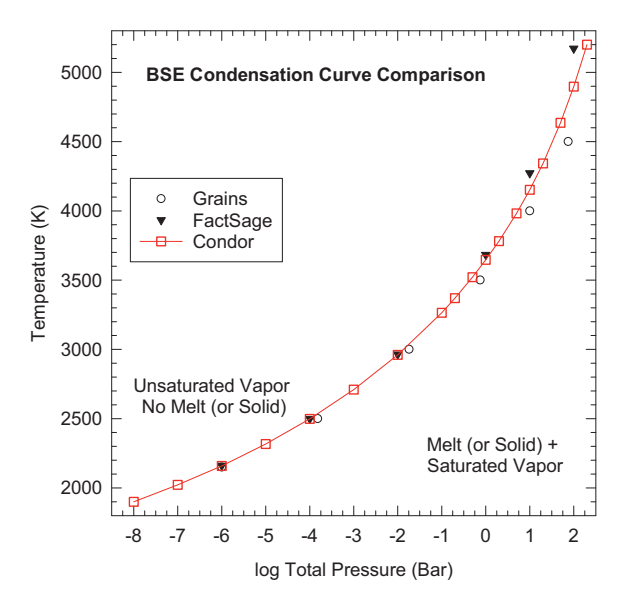


**Fig. 1.** The condensation curve for molten BSE material as a function of total pressure and a comparison of results from the CONDOR, FactSage and GRAINS codes. The curve shows where melt becomes stable; only vapor is present to the left above the curve. A mixture of vapor plus melt is present on and below the curve to the right. **Fig. 2** illustrates the composition of the melt as a function of total pressure.

**Table 4**Condensation curve for bulk silicate Earth material.

Log P	-6	-4	-2	0	1	2
Dry	2159	2498	2960	3645	4151	4894
Wet	2158	2496	2949	3619	4113	4837
FactSage	2161	2499	2964	3683	4272	5172
GRAINS	2150	2458	2923	3544	3979	4581
$fO_2$	4.4 ×	7.3 ×	$1.1 \times$	0.126	1.23	11.3
(bar) <sup>a</sup>	$10^{-8}$	$10^{-6}$	$10^{-3}$			

<sup>&</sup>lt;sup>a</sup> The  $fO_2$  is identical within  $\leq$ 5% in the dry and wet BSE models.

Fig. 1. Linear least squares equations for computing total pressure  $P_T$  over the melt as a function of temperature [f(T)] or the converse T=f  $(P_T)$  along the (dry) molten BSE condensation curve from  $10^{-8}$  to  $10^2$  bar are

$$log P_{T} = 8.564 - \frac{31415.9}{T}$$

$$\frac{10,000}{T} = 2.726 - 0.31823 log P_T$$

The corresponding equations for the wet molten BSE condensation curve are

$$log P_T = 8.638 - \frac{31503.7}{T}$$

$$\frac{10,000}{T} = 2.742 - 0.31727 log P_T$$

The results from the CONDOR and FactSage codes agree within 38 K up to one bar with increasing disagreement at higher pressures reaching 278 K (6%) at 100 bar. FactSage gives higher condensation temperatures than CONDOR at all pressures. Both codes used the same model bulk composition and both codes are well validated as described earlier. The differences in the results are due to the large extrapolation in temperatures and pressures from one bar and temperatures < 2000 K where the solution parameters are optimized for use.

Table 4 and Fig. 1 also compare CONDOR and FactSage code results to those from the GRAINS code (Lock et al., 2018), which is a Gibbs energy minimization code developed by Petaev (2009). Petaev (personal communication, 2021) kindly supplied us with tabular data for the 20 element ideal solution calculations discussed in Lock et al. (2018) and earlier in several abstracts at the Lunar and Planetary Science Conference (Petaev et al., 2014, 2015, 2016). The agreement with CONDOR and FactSage results is good overall, except at the highest temperatures and pressures studied, e.g., differences are 313 K (6%) at 100 bar between CONDOR and GRAINS. Again, the differences are due to large extrapolations in thermodynamic data.

The GRAINS code calculations include He and the volatiles H, C, N, S, and Cl that are only in the wet BSE model. Table 4 shows the wet BSE model agrees even better with the GRAINS code results at all pressures. The wet BSE model gives lower condensation temperatures at the same total pressure because the O and O<sub>2</sub> partial pressures at a given temperature are lowered by H, OH, CO, CO<sub>2</sub>, H<sub>2</sub>O, H<sub>2</sub>O, NO, S<sub>2</sub>, SO, and other volatile-bearing gases. As a result, reactions of Al and Ca with O or O<sub>2</sub> forming Al<sub>2</sub>O<sub>3</sub> and CaO in the molten oxide only reach equilibrium at a lower temperature where the fO<sub>2</sub> of wet BSE material is the same as the fO<sub>2</sub> of dry BSE material. The bottom row in Table 4 shows the fO<sub>2</sub> values along the dry and wet BSE condensation curves, which we found equal within  $\leq$ 5% at the same total pressure.

The major conclusion from *all* results in Fig. 1 is the extremely high temperatures for silicate melt stability in a system with silicate bulk composition in the absence (or with only very small amounts) of hydrogen. At a given pressure and temperature the oxygen fugacity and rocky element abundances (i.e., the metallicity) are significantly higher in a silicate bulk composition system than in solar composition, i.e.,  $H_2$  and  $H_2$  definition of the system  $H_2$  and  $H_3$  definition of the solution  $H_3$  are significantly higher in a silicate bulk composition system than in solar composition, i.e.,  $H_3$  and  $H_3$  definition  $H_3$  definition

Although the CONDOR, FactSage, and GRAINS codes use different activity coefficient models derived from data at <2000 K and have different algorithms, BSE melt condensation temperatures from all three codes agree (within the small differences mentioned above). The highest temperatures involve the largest extrapolations in activity coefficient models and larger differences between the three models are not surprising. Nevertheless, the fact that BSE melt condensation temperatures from the three different codes agree within  $\leq\!10\%$  over eight orders of magnitude in pressure and a factor of 2.4 in temperature is noteworthy given the large extrapolations involved in the different activity coefficient models and thermodynamic data.

This good agreement between condensation temperatures exists because the  $RTln\gamma_i$  term and differences between  $RTln\gamma_i$  terms from different activity coefficient models are smaller than the enthalpy  $(\Delta H^\circ)$  and entropy  $(\Delta S^\circ)$  of condensation. We illustrate this using the condensation of CaO, one of the two most refractory oxides in the initially condensed BSE melt:

$$Ca(gas) + \frac{1}{2}O_2(gas) = CaO(melt)$$

The reaction isotherm gives the Gibbs energy change for CaO condensation

$$\Delta G_{CaO} = \Delta G_{CaO}^{\circ} + RTln \frac{a_{CaO}}{P_{Ca} f_{O_2}^{1/2}} \label{eq:deltaGcaO}$$

At equilibrium between the gas and melt,  $\Delta G = 0\,$ 

$$\Delta G_{\text{CaO}} = 0 = \Delta G_{\text{CaO}}^{\circ} + \text{RTIn} \frac{a_{\text{CaO}}}{P_{\text{Ca}} f_{\text{O}_{2}}^{1/2}}$$

Rewriting the reaction isotherm gives

$$\Delta G_{CaO}^{\circ} = \, -RTln \frac{a_{CaO}}{P_{Ca} f_{O_2}^{1/2}} = \, -RTln K_{eq} \label{eq:deltaGaO}$$

This equation shows the relationship between the standard Gibbs energy change, which is at one bar pressure, and the reaction quotient, which is equal to the equilibrium constant  $K_{\rm eq}$ .

The standard Gibbs energy change is also given by the Gibbs - Helmholtz equation

$$\Delta G_{CaO}^{\circ} = \Delta H_{CaO}^{\circ} - T \Delta S_{CaO}^{\circ}$$

Rewriting the reaction quotient by substituting for activity with the equation  $a=\gamma X$  and using the definition of the partial molal ideal entropy of mixing,

$$\overline{\Delta S}_{i}^{M} = -RlnX_{i}$$

After substituting back into the reaction isotherm and grouping terms

$$\left[\Delta H_{\text{CaO}}^{\circ} + RT ln \gamma_{\text{CaO}}\right] - T \left[\Delta S_{\text{CaO}}^{\circ} + \overline{\Delta} \overline{S}_{\text{CaO}}^{M}\right] = RT \left( ln P_{\text{Ca}} + \frac{1}{2} ln f_{\text{O}_{2}} \right)$$

Over the 2000–4500 K range, JANAF (or IVTAN) data show typical  $\Delta H^{\circ}$  values for the CaO condensation reaction are -710 to -670 kJ mol $^{-1}$  versus typical RTln( $\gamma_{CaO}$ ) values of  $-145\pm5$  kJ mol $^{-1}$ , about 17% of the [enthalpy term]. Typical  $\Delta S^{\circ}$  values are -170 to -155 J mol $^{-1}$  K $^{-1}$  (2000–4500 K) versus typical RTlnX $_{CaO}$  values of 29 J mol $^{-1}$  K $^{-1}$ , about 17% of the [entropy term]. The energetic differences between two different activity coefficient models are smaller than these between the Ban-Ya regular solution model and ideal solution. Thus, the CaO condensation temperatures are closer as seen in Fig. 1. Table 4 and Fig. 1 show the net effect of these differences; the CONDOR and FactSage calculations used two different non-ideal melt models while that of Lock et al. (2018) used an ideal melt model. All three sets of calculations give the same result to first order because the  $\Delta H^{\circ}$  and  $\Delta S^{\circ}$  for condensation of pure liquid oxides are larger than the  $\Delta H^{\circ}$  and  $\Delta S^{\circ}$  terms due to formation of non-ideal oxide melts. Ebel (2005) and Ebel

and Grossman (2005) reached a similar conclusion in their calculations.

### 3.2. Melt composition

The composition of the initially condensed melt varies with total pressure as shown in Fig. 2. The melt is mainly  $Al_2O_3$  (more abundant) and CaO (less abundant) at lower total pressures with increasing amounts of CaO, MgO and other oxides and decreasing amounts of  $Al_2O_3$  and CaO with increasing pressure. As MgO becomes the major oxide in the melt, the amounts of  $Al_2O_3$  and CaO are diluted by the more abundant MgO. Table 5 compares melt compositions at  $10^{-3}$ , 10, and 100 bars calculated by the CONDOR and FactSage codes. The FactSage code shows the same general trend with total pressure, but the overall agreement is only fair. However, the two codes show the same key point; namely the initially condensed melt at any total pressure is more refractory with less  $SiO_2$ ,  $FeO_3$ , and  $Na_2O$  than the BSE composition in Table 1.

# 3.3. Condensation chemistry of major, minor, and trace elements in dry BSE material

# 3.3.1. Oxygen

Oxygen, the most abundant element in BSE material, is considered first. Fig. 3a (dry BSE model) and 3b (wet BSE model) show logarithmic contours of constant oxygen fugacity (fO<sub>2</sub>) over the 1500–4500 K and  $10^{-6}$  to  $10^2$  bar total pressure range. The thicker dark green curves in Fig. 3a and b show 50%, 99%, and 99.99% (only in Fig. 3a) condensation of total oxygen into the BSE melt, which causes the curvature and fine structure of the log fO<sub>2</sub> contours. Grid calculations with  $\Delta T=4~\rm K$  and  $\Delta(log_{10}P)=0.10$  or 0.16 gave the same fine structure and took several weeks computer runtime because of the complexity of the calculations. The most abundant oxides in BSE material (MgO, SiO<sub>2</sub>, FeO) condense into the BSE melt within a small temperature range in the vicinity of the oxygen 50% condensation curve and the amount of oxygen left in the gas decreases markedly. The CONDOR chemical equilibrium calculations give the equilibrium fO<sub>2</sub> and the fraction of oxygen condensed into the melt.

A comparison of the shape and range of the  $log fO_2$  contours for the dry and wet BSE models is instructive. Above the 50% condensation

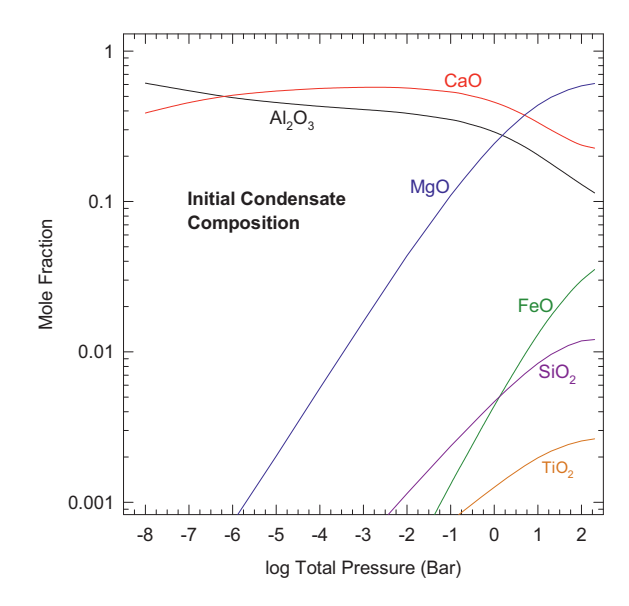


**Fig. 2.** The composition of the initially condensed melt as a function of total pressure using the nominal activity coefficients in Table 2. Note the composition axis is logarithmic. Fig. 1 gives the melt condensation curve. See the text and Table 5 for a comparison of initial melt compositions from the CONDOR and FactSage codes.

**Table 5**Composition of initial condensates (mol%).

Oxide	$P = 10^{-3} \text{ bar}$	$P=10^{-3}$ bar			P = 100  bar		
	CONDOR <sup>a</sup>	FactSage <sup>b</sup>	CONDOR <sup>a</sup>	FactSage <sup>b</sup>	CONDOR <sup>a</sup>	FactSage <sup>b</sup>	
CaO	48.	21.	34.	3.	24.	1.	
MgO	2.	2.	44.	52.	59.	58.	
$Al_2O_3$	50.	76.	20.	16.	13.	14.	
$SiO_2$	0.06	0.6	0.8	28.	1.	26.	
FeO	0.01	0.04	1.	0.3	3.	0.4	
Na <sub>2</sub> O	1.e-14	1.e-7	4.e-5	1.e-4	7.e-6	4.e-4	
Total	100.1 <sup>c,d</sup>	99.6 <sup>c,d</sup>	$100.0^{\circ}$	99.3 <sup>d</sup>	100.2 <sup>c,d</sup>	99.4 <sup>d</sup>	

 $<sup>^{</sup>m a}$  The calculated condensation temperatures are 2706 K at  $10^{-3}$  bar, 4152 K at 10 bar, and 4895 K at 100 bar.

d Totals are not 100% due to rounding.

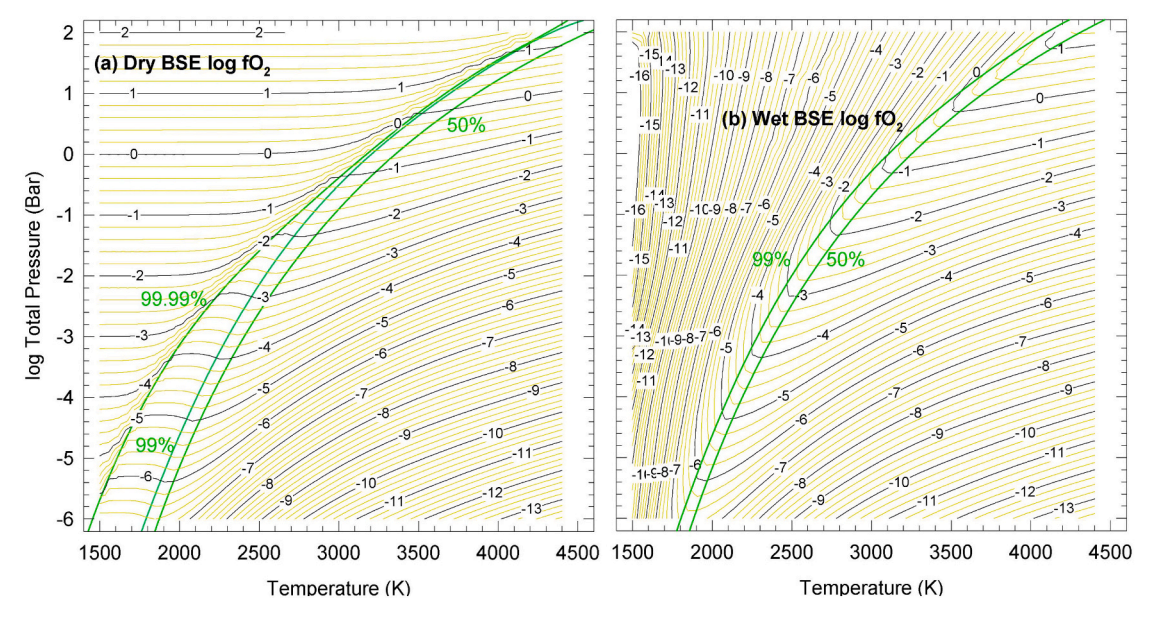


Fig. 3. Oxygen equilibrium chemistry in dry (a) and wet (b) BSE material as a function of temperature and total pressure. The curves are logarithmic contours of constant oxygen fugacity (fO<sub>2</sub>). The dark green curves show the 50%, 99%, and 99.99% (3a only) condensation curves for oxygen. The CONDOR code computes the  $O_2$  fugacity; there is no separate  $fO_2$  buffer. Kinks in the contours in this figure and subsequent figures are due to size of the P and T steps in the grid. See the text for a detailed discussion of this figure. (For interpretation of the references to colour in this figure legend, the reader is referred to the web version of this article.)

temperature of oxygen, i.e., to the right of the 50% curve, the  $fO_2$  contours have the same shape and about the same value at any P, T point. The small difference between the dry and wet  $fO_2$  values leads to slightly lower condensation temperatures for wet BSE melt at the same total pressure ( $P_T$ ) as seen in Table 4.

Below the 50% condensation temperature of oxygen, to the left of the 50% curve, the shape, and values of the fO $_2$  contours are different. In the dry BSE model, the fO $_2$  contours go through a shallow minimum near the 50% condensed curve and then flatten out parallel to isobars. The fO $_2$  is independent of temperature in the low T, high P region at the top left of Fig. 3a. In the wet BSE model (Fig. 3b) fO $_2$  contours go through a deeper minimum between 50% and 99% condensed and then curve upward with fO $_2$  decreasing steeply with decreasing temperature on isobars and with increasing pressure on isotherms. At the lowest temperatures and highest pressures in the dry BSE model (top left in Fig. 3a), almost no rocky elements are in the gas; the O $_2$  fugacity equals the total gas pressure to good approximation. In the same P, T range, speciation in the wet BSE model (in Fig. 3b) is completely different with fO $_2$  contours down to  $10^{-16}$  bar. The major oxygen – bearing gases are CO and  $\rm H_2O$  with the fO $_2$  controlled by the water gas reaction

$$H_2 + CO_2 = H_2O + CO$$

Although  $O_2$  does not appear in the water gas reaction, the  $H_2/H_2O$  and  $CO/CO_2$  ratios each control  $FO_2$  and give identical  $FO_2$  values.

As temperature is isobarically increased in the dry BSE model, i.e., moving from left to right along horizontals in Fig. 3a, rocky elements vaporize from the melt into the gas and reduce the O2 abundance in the gas. The more volatile elements such as Au, Ag, Cd, Cu, Zn, and As vaporize at lower temperatures but are less abundant than major elements such as Si, Fe, Mg, and Ti. Thus, log fO2 contours initially show small deviations from isobars. But as temperature continues increasing, more of the major elements go into the gas and the O2 mole fraction decreases. Several factors including formation of metal (metalloid) oxide gases, thermal dissociation of O2 to O atoms, and eventually thermal ionization of all elements lead to large decreases in the O2 abundance at any given pressure. The fO<sub>2</sub> contours slope upward with respect to the isobars they originally followed, e.g., compare the log  $P_{Total} = -1$  isobar and the log  $fO_2 = -1$  contour in Fig. 3a. Deviations between isobars and fO2 contours increase with decreasing pressure and increasing temperature. At 4500 K and  $10^{-6}$  bar,  $fO_2$  is reduced to 1.5 imes $10^{-14}$  bar by the effects mentioned earlier. The equilibrium partial pressures of the major gases are O (4.4  $\times$  10<sup>-7</sup> bar), Mg<sup>+</sup> (1.4  $\times$  10<sup>-7</sup> bar),  $\text{Si}^+$  (7.4 × 10<sup>-8</sup> bar), Si (4.6 × 10<sup>-8</sup> bar), and  $\text{Fe}^+$  (1.6 × 10<sup>-8</sup> bar). Figs. 6-9 of Fegley et al. (2020) shows these changes at one bar total

 $<sup>^{</sup>m b}$  The calculated condensation temperatures are 2710 K at  $10^{-3}$  bar, 4272 K at 10 bar and 5168 K at 100 bar.

 $<sup>^{\</sup>rm c}$  Also includes 0.03% TiO<sub>2</sub> (10<sup>-3</sup> bars), and 0.2% TiO<sub>2</sub> at 10 and 100 bars.

pressure for Si, Mg, Fe, and O in bulk Earth vapor.

#### 3.3.2. Major elements

The composition of the condensed BSE melt changes with temperature because more refractory elements condense at higher temperatures and more volatile elements condense at lower temperatures along isobars. Figs. 4, 8a, 9a, 10a, 11a, 12a, and b and Tables 6-11 show the 50% condensation curves from CONDOR code calculations for Ca, Al, Mg, Si, Fe, Ti, Mn, Cr, Na, and K as a function of total pressure from  $10^{-6}$  to  $10^{2}$ bar in the dry BSE model. Table 6 also shows 50% condensation temperatures for Ca, Al, Mg, Si, and Fe in the wet BSE model using the Ban-Ya activity coefficients. Except for nickel, discussed later, the major elements are the most abundant elements in Table 1. The different symbols denote different activity coefficient models used in the calculations. The black curves are fits to the nominal activity coefficient model. The graphs show ideal solution 50% condensation temperatures from 10<sup>-4</sup> to 10<sup>2</sup> bar calculated with the GRAINS code by Lock et al. (2018). The graphs also show 50% condensation temperatures at one bar total pressure for elements listed in Table 4 of Ivanov et al. (2022), which are the only tabular values in their paper. We also did ideal solution calculations with the CONDOR code. Figure labels show major gases in the region above the curves where each element is >50% in the gas, and oxide(s) dissolved in the BSE melt below the curve where each element is >50% in the melt. Figs. 5, 6, 7, 8b, 9b, and 10b show 50% condensation curves superimposed on logarithmic grids of the ratios of major gases for each element.

#### 3.3.3. Calcium

Fig. 4a shows the "50%" condensation curve for calcium, which coincides with the curve in Fig. 1. Calcium is more than 50% condensed where melt initially forms; at  $10^{-6}$  bar Ca is 68% condensed and at  $10^{2}$ bar Ca is 98% condensed. The CONDOR code calculations use activity coefficients from the Ban-Ya model, the MAGMA code, and the FactSage code (see Table 2). The MAGMA activity coefficients are linear least squares fits to  $log_{10}\gamma(CaO)$  values versus 1/T where the  $\gamma(CaO)$  values were calculated for a nine-oxide model (MgO, SiO<sub>2</sub>, FeO, CaO, Al<sub>2</sub>O<sub>3</sub>, Na2O, TiO2, K2O, ZnO) of the BSE composition used by Fegley et al. (2016) over the 2000-5500 K range. All activity coefficients from the MAGMA code in Table 2 are from the same set of calculations. The FactSage activity coefficients are linear least squares fits to  $log_{10}\gamma(CaO)$ values versus 1/T for the six oxide BSE composition (Table 1) over the 2000-3000 K range and were previously used in Fegley et al. (2016). All activity coefficients from the FactSage code in Table 2 are from the same set of calculations except for As<sub>2</sub>O<sub>3</sub>, B<sub>2</sub>O<sub>3</sub>, GeO<sub>2</sub>, Li<sub>2</sub>O, PbO, SnO, SnO<sub>2</sub>, and ZnO done from 1800 to 2200 K. Fig. 4a and Table 6 show the condensation temperatures for the three sets of activity coefficients are similar. There is a 94 K range at  $10^{-6}$  bar between the highest and lowest values (5% difference) decreasing with increasing pressure to a 10 K (0.2%) difference at 100 bar. Table 6 also shows condensation temperatures from the dry and wet BSE models agree within 1-57 K over the  $10^{-6}$ - $10^{2}$  bar range. The ideal solution condensation temperatures, either from Lock et al. (2018) or those computed in this work using the CONDOR code, are lower, as they should be, because the activity

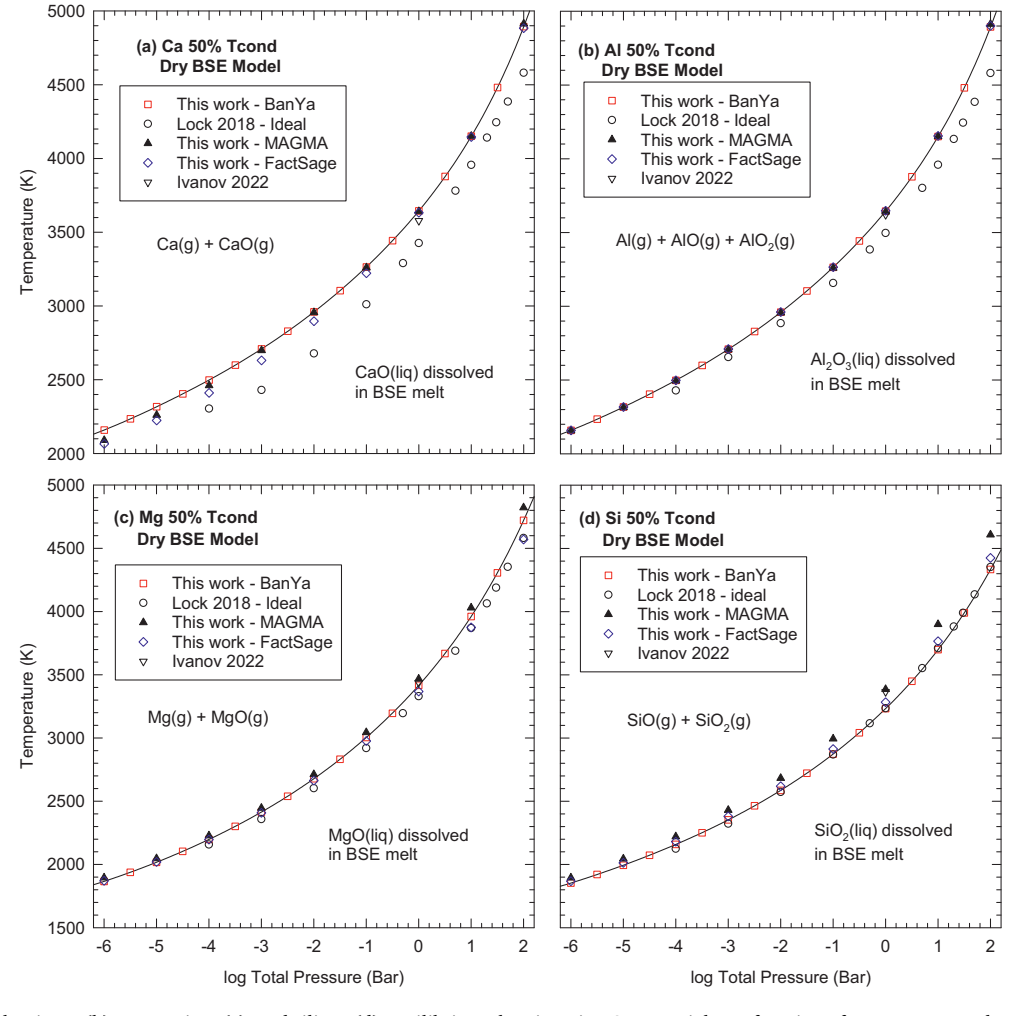


Fig. 4. Calcium (a), aluminum (b), magnesium (c), and silicon (d) equilibrium chemistry in BSE material as a function of temperature and total pressure. The black curves are the 50% condensation curves. Calcium and aluminum are >50% condensed where melt forms. See the text for a detailed discussion of this figure.

**Table 6**Ca, Al, Mg, Si, and Fe 50% condensation temperatures.

Log P (bar)	BanYa	BY wet	MAGMA	FactSage	Ideal (lock)	Ideal (this work)
Calcium						
-6	2159	2158	2090	2065	_	1880
-4	2498	2496	2461	2411	2304	2216
-2	2960	2949	2956	2897	2678	2700
0	3645	3619	3640	3633	3426	3448
2	4894	4837	4893	4884	4581	4758
Aluminum						
-6	2159	2158	2157	2159	_	2134
-4	2498	2496	2495	2498	2429	2460
-2	2960	2949	2956	2961	2885	2901
0	3645	3619	3641	3648	3496	3555
2	4894	4837	4913	4901	4581	4734
Magnesiun	n					
-6	1866	1865	1895	1871	_	1817
-4	2198	2197	2228	2197	2157	2135
-2	2678	2677	2712	2663	2602	2592
0	3417	3415	3467	3368	3330	3303
2	4721	4719	4822	4570	4581	4561
Silicon						
-6	1853	1852	1895	1868	_	1820
-4	2159	2157	2221	2181	2124	2132
-2	2586	2585	2683	2619	2573	2572
0	3233	3230	3386	3284	3235	3228
2	4334	4327	4608	4425	4352	4341
Iron						
-6	1818	1814	1871	1832	-	1813
-4	2138	2135	2208	2148	2120	2131
-2	2581	2579	2679	2597	2584	2584
0	3284	3282	3423	3318	3320	3303
2	4599	4596	4812	4657	4581	4627

See text for details.

**Table 7**Ti 50% condensation temperatures – different activity coefficient models.

Log P (bar)	BanYa	MAGMA	FactSage	Ideal (Lock)	Ideal (this work)
-6	1882	1990	1896	_	1879
-4	2213	2318	2239	2129	2192
-2	2690	2803	2744	2649	2650
0	3433	3580	3558	3388	3378
2	4778	4913	4894	4581	4694

See text for details.

**Table 8**Mn 50% condensation temperatures – different activity coefficient models.

Log P (bar)	BanYa	FactSage	Ideal (Lock)	Ideal (this work)
-6	1807	1835	_	1808
-4	2134	2149	2111	2127
-2	2579	2594	2573	2574
0	3287	3286	3275	3279
2	4597	4497	4487	4563

See text for details.

coefficient equations for CaO give negative deviations from ideality in the BSE melt. The ideal solution values are a lower limit to the "50%" condensation temperature for CaO (liquid) dissolved in the dry BSE melt. Ideal solution condensation temperatures are useful because they help disentangle volatility and activity coefficient contributions to condensation temperatures, e.g., for the alkalis, alkaline earths, and the Group 13–15 elements.

**Table 9**Cr 50% condensation temperatures – FactSage and Ideal.

Log P (bar)	FactSage	FS (wet)	Ideal (Lock)	Ideal (this work)
-6	1803	1798	_	1802
-4	2121	2115	2106	2113
-2	2554	2547	2534	2540
0 <sup>a</sup>	3196	3188	3154	3173
2	4299	4290	4199	4253

 $<sup>^{\</sup>rm a}$  Ivanov et al. (2022) give a 50% condensation temperature of 3346 K at 1 bar total pressure. See text for details.

**Table 10**Na 50% condensation temperatures – real and ideal solution.

Log P (bar)	BanYa	MAGMA	FactSage	Sossi	Ideal (Lock)	Ideal (this work)
-6	1477	1569	1627	1488	-	1102
-4	1820	1942	2013	1853	1583	1364
-2	2373	2486	2527	2436	1800	1809
0	3154	3184	3199	3176	2469	2743
2	4276	4324	4426	4330	3772	4223

See text for details.

**Table 11**K 50% condensation temperatures – different activity coefficient models.

Log P (bar)	MELTS	MAGMA	FactSage	Sossi	Ideal (lock)	Ideal (this work)
-6	1528	1574	1564	1441	-	1021
-4	1863	1954	1930	1775	<1500	1267
-2	2403	2550	2485	2321	1752	1691
0	3161	3339	3187	3140	2297	2699
2	4286	4648	4410	4263	3807	4223

See text for details.

The two major Ca-bearing gases in the dry and wet models are Ca and CaO, in agreement with Knudsen effusion mass spectrometry (KEMS) measurements of molten lunar basalts (DeMaria et al., 1971; Markova et al., 1986) and CaO-bearing melts (Stolyarova et al., 1991; Shornikov et al., 1997; Shornikov, 2020). The other Ca-bearing gases included in the calculations ( $Ca_2$ ,  $Ca^+$ ,  $Ca^{2+}$ ) are much less abundant along the condensation curve.

Fig. 5a shows the thick red colored CaO "50%" condensation curve superimposed on a logarithmic grid of CaO/Ca molar ratio contours over the 1500–4500 K and  $10^{-6}$  to  $10^2$  bar range. Calcium oxide is the major Ca-bearing gas at low T and high P (top left), Ca is the major Ca-bearing gas at high T and low P (bottom right), and the two gases have equal abundances on the zero contour. The irregularities in the zero contour and others in its vicinity arise from condensation of oxygen into the melt (see Fig. 3). The distribution of calcium between monatomic Ca gas and CaO gas depends upon temperature and fO<sub>2</sub> via

$$Ca(gas) + \frac{1}{2}O_2(gas) = CaO(gas)$$

The equilibrium constant for this reaction is

$$K_{eq} = \frac{P_{CaO}}{P_{Ca}} \cdot \frac{1}{f_{O_2}^{1/2}} = \frac{X_{CaO}}{X_{Ca}} \cdot \frac{1}{f_{O_2}^{1/2}}$$

Rearranging, taking logs, and using IVTAN data for log  $K_{eq}$ ,

$$log_{10} \left( \frac{X_{CaO}}{X_{Ca}} \right) = \frac{1}{2} log_{10} f_{O_2} + \frac{6474.2}{T} - 1.650$$

The equation shows the CaO/Ca ratio increases with the square root of oxygen fugacity and with decreasing temperature.

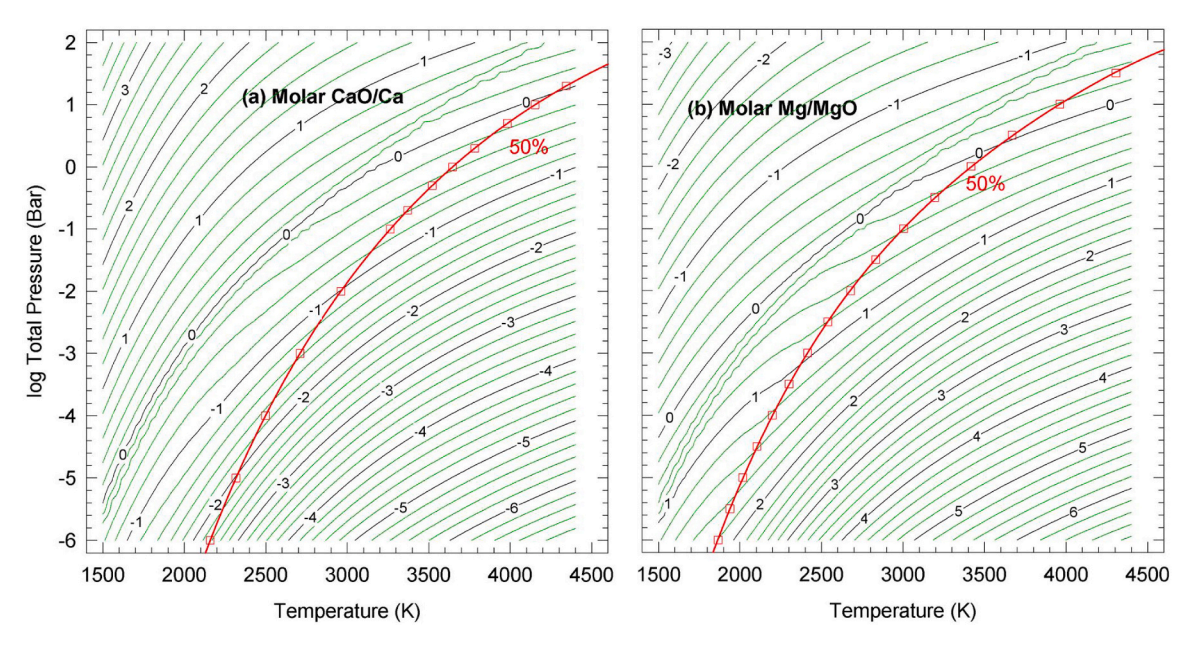
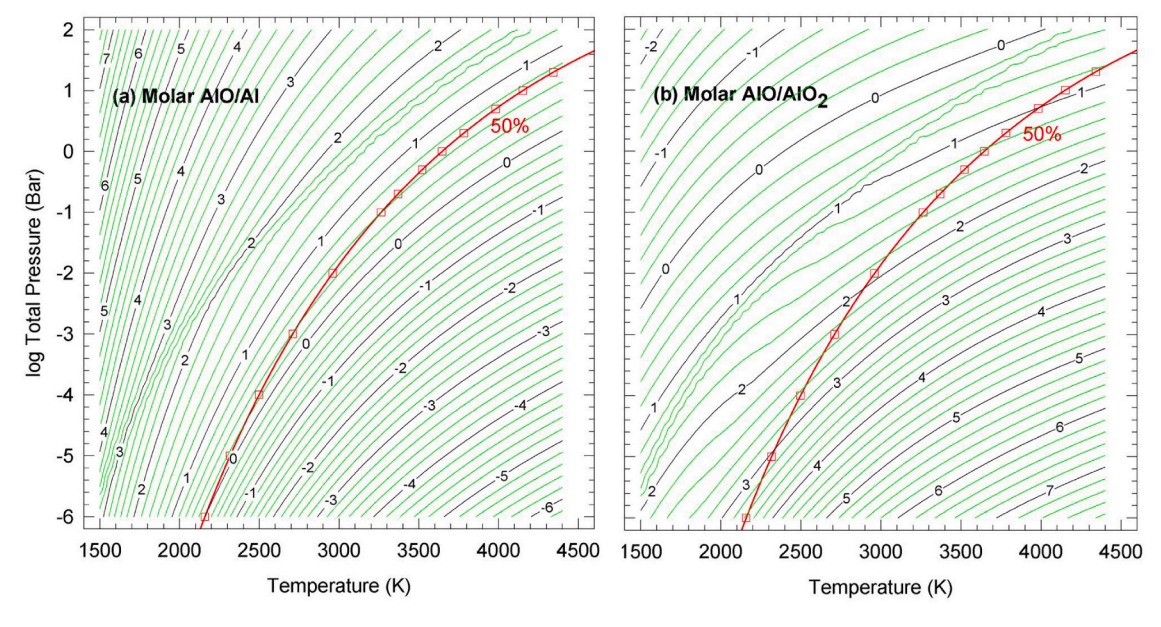


Fig. 5. The distribution of calcium (a) and magnesium (b) between monatomic and monoxide gases as a function of temperature and total pressure. The logarithmic contours give the CaO/Ca (5a) and Mg/MgO (5b) molar ratios. The red colored 50% condensation curves for calcium and magnesium are superimposed on the contours. (For interpretation of the references to colour in this figure legend, the reader is referred to the web version of this article.)



**Fig. 6.** The distribution of aluminum between monatomic and oxide gases as a function of temperature and total pressure. The red colored 50% condensation curve for aluminum is superimposed on the logarithmic molar contours. Molar ratios of AlO/Al are in (a) and molar ratios of AlO/AlO<sub>2</sub> are in (b). (For interpretation of the references to colour in this figure legend, the reader is referred to the web version of this article.)

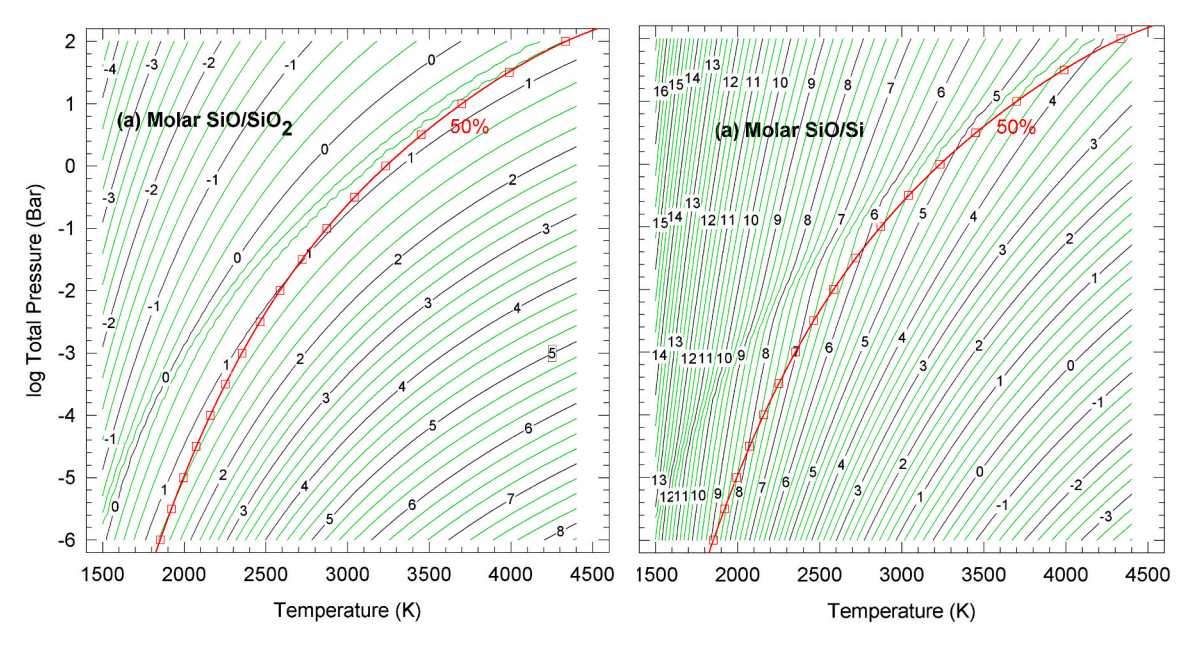
# 3.3.4. Aluminum

Fig. 4b shows the "50%" condensation curve for aluminum, which coincides with the curve in Fig. 1. Aluminum, like Ca, is >50% condensed where melt forms. At  $10^{-6}$  bar Al is 98% condensed and at  $10^2$  bar Al is 79% condensed. CONDOR code calculations used activity coefficients from the Ban-Ya model, the MAGMA code, and the FactSage code (see Table 2). Table 6 lists the "50%" condensation temperatures for the three sets of activity coefficients and for ideal solution calculations done in this work and by Lock et al. (2018). The range between the highest and lowest condensation temperatures from the three activity coefficient models varies from 2 K (0.1%) at  $10^{-6}$  bar to 19 K (0.4%) at  $10^{-6}$  bar. Fig. 2 shows the  $Al_2O_3$  content of the melt increases with

decreasing pressure and as this occurs the ideal solution model becomes more realistic and all condensation temperatures approach the same value as seen in Fig. 4b.

Aluminum gas chemistry is complex. Depending on P and T, monatomic Al or AlO is the major Al-bearing gas along the condensation curve; their relative abundances (Al/AlO) vary from 0.99 to 1 (2159 K,  $10^{-6}$  bar) to 0.18 to 1 (4894 K,  $10^2$  bar). Either Al<sub>2</sub>O, AlO<sub>2</sub>, or Al<sub>2</sub>O<sub>2</sub> is the next most abundant gas with Al<sub>2</sub>O favored at lower pressure and AlO<sub>2</sub> or Al<sub>2</sub>O<sub>2</sub> favored at higher pressure. The other Al-bearing gases in the calculations (Al<sup>+</sup>, Al<sup>2+</sup>, Al<sup>-</sup>, Al<sub>2</sub>, AlO<sup>+</sup>, Al<sub>2</sub>O<sub>3</sub>) are less abundant.

Fig. 6 shows the thick red colored alumina condensation curve superimposed on logarithmic grids of the AlO/Al and AlO/AlO<sub>2</sub> molar



**Fig. 7.** The distribution of silicon between monatomic and oxide gases as a function of temperature and total pressure. The red colored 50% condensation curve for silicon is superimposed on the logarithmic molar contours. Molar ratios of SiO/SiO<sub>2</sub> and of SiO/Si are in (a) and (b), respectively. (For interpretation of the references to colour in this figure legend, the reader is referred to the web version of this article.)

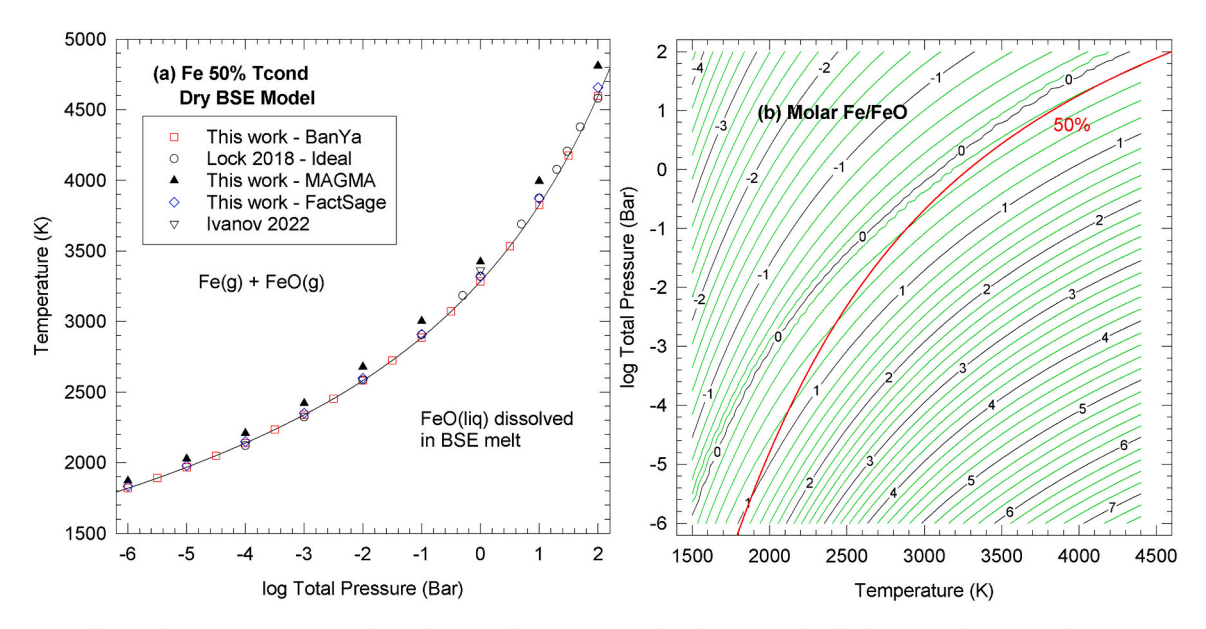


**Fig. 8.** (a) Iron equilibrium chemistry in BSE material as a function of temperature and total pressure. The black curve is the 50% condensation curve for FeO. (b) The distribution of iron between Fe and FeO gases as a function of temperature and total pressure. The logarithmic contours give the Fe/FeO molar ratios. The red colored 50% condensation curve for iron is superimposed on the contours. (For interpretation of the references to colour in this figure legend, the reader is referred to the web version of this article.)

ratios over the 1500–4500 K and  $10^{-6}$  to  $10^2$  bar range. Fig. 6a and b show the same trend: lower T and higher P favors the more complex gas in each pair (i.e., AlO vs Al) and higher T and lower P favors the less complex gas in each pair (i.e., AlO vs AlO<sub>2</sub>). Consistent with our results, the KEMS data of DeMaria et al. (1971) and Markova et al. (1986) show Al > AlO > Al<sub>2</sub>O over molten lunar basalts up to 2500 K at pressures to the left of the red curve in Fig. 6.

### 3.3.5. Magnesium

Fig. 4c shows the 50% condensation curve for magnesium computed using the three sets of MgO activity coefficients from Table 2, and comparison with the Lock et al. (2018) ideal solution values. The dry

and wet condensation temperatures are the same within 2 K. The 50% condensation temperatures for the three sets of activity coefficients agree very well with each other and with ideal solution calculations at lower pressures but diverge into two groups with increasing pressure. The Ban-Ya and MAGMA results form one cluster whereas the FactSage and two sets of ideal solution calculations form another cluster (see Table 6). The difference is 260 K (6%) at 100 bar total pressure. Magnesium oxide shows negative deviations from ideality in the BSE melt. Fig. 4c and Table 6 show the ideal solution condensation temperatures are lower than those from the activity coefficient models, as they should be. Our ideal solution 50% condensation temperatures are slightly lower than those of Lock et al. (2018). The small disagreements could be due to

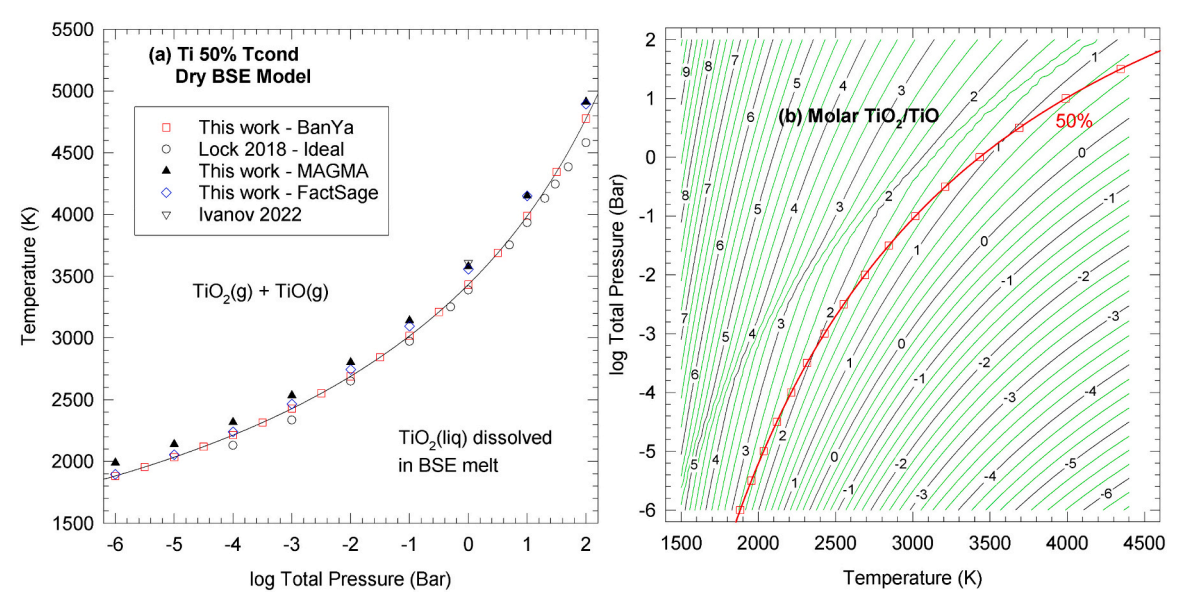
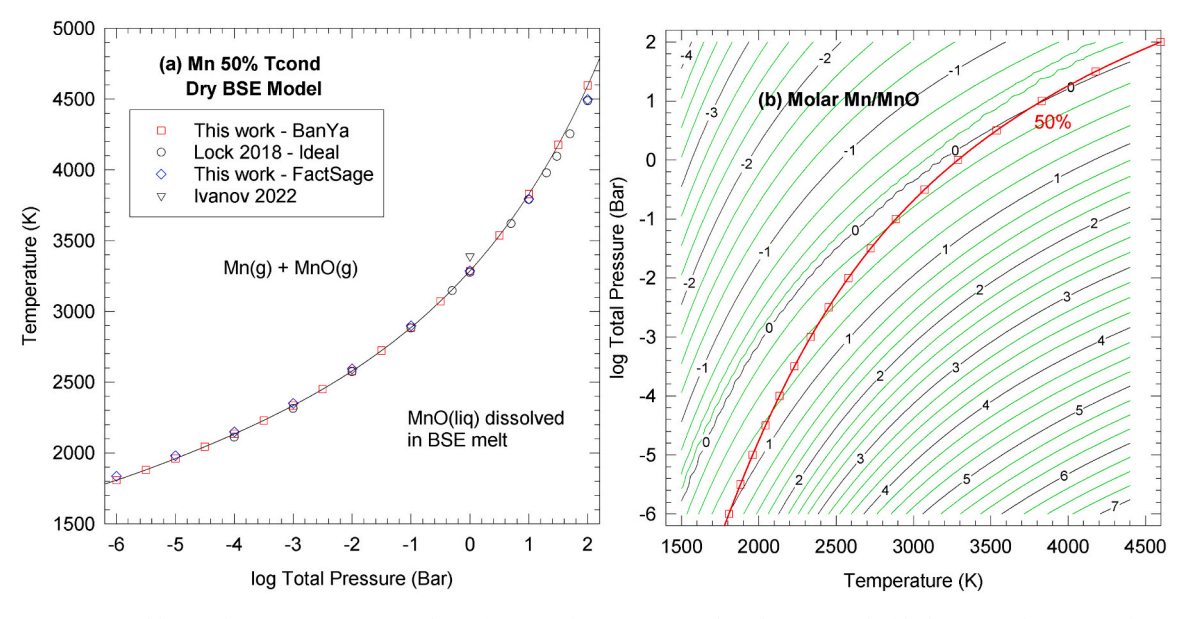


Fig. 9. (a) Titanium equilibrium chemistry in BSE material as a function of temperature and total pressure. The black curve is the 50% condensation curve for  $TiO_2$ . (b) The distribution of titanium between TiO and  $TiO_2$  gases as a function of temperature and total pressure. The logarithmic contours give the  $TiO_2/TiO$  molar ratios. The red colored 50% condensation curve for titanium is superimposed on the contours. The other Ti-bearing gases included in the calculations are less important (Ti, Ti<sup>+</sup>, Ti<sup>2+</sup>). (For interpretation of the references to colour in this figure legend, the reader is referred to the web version of this article.)



**Fig. 10.** (a) Manganese equilibrium chemistry in BSE material as a function of temperature and total pressure. The black curve is the 50% condensation curve for MnO. (b) The distribution of manganese between Mn and MnO gases as a function of temperature and total pressure. The logarithmic contours give the Mn/MnO molar ratios. The red colored 50% condensation curve for MnO is superimposed on the contours. (For interpretation of the references to colour in this figure legend, the reader is referred to the web version of this article.)

different data sources or extrapolation of data from lower to higher temperatures.

The chemical equilibrium calculations include Mg, Mg<sup>+</sup>, Mg<sup>2+</sup>, Mg<sub>2</sub>, and MgO; but only Mg and MgO are important along the condensation curve as seen in Fig. 5b. Monatomic Mg is dominant at high temperature and low pressure (lower right) while MgO is dominant at low temperature and high pressure (upper left); the two gases have comparable abundances along the condensation curve at the highest P and T (upper right corner) in Fig. 5b. KEMS studies of molten lunar basalts (DeMaria et al., 1971, Markova et al., 1986), molten olivine (Costa et al., 2017), and molten MgO-SiO<sub>2</sub> (Kambayashi and Kato, 1984) show Mg is the major Mg-bearing gas in agreement with our low-pressure results. A

comparison of Fig. 5a and b shows CaO gas is more stable than MgO gas at a given temperature and pressure, i.e., the CaO/Ca log zero contour is at higher T than the Mg/MgO contour at any P.

### 3.3.6. Silicon

Fig. 4d shows the 50% condensation curve for silicon computed using  $SiO_2$  activity coefficients from Table 2 and comparison with the Lock et al. (2018) ideal solution values. Table 6 shows the dry and wet 50% condensation temperatures are identical within 1–7 K. As seen for magnesium in Fig. 4c, the 50% condensation temperatures for silicon agree well with one another and with ideal solution calculations at low pressures but disagree with increasing pressure; the difference is 274 K

(6%) at 100 bar total pressure (see Table 6). The condensation temperatures using activity coefficients from Ban-Ya, FactSage, and ideal solution are closer to one another than those using MAGMA code activity coefficients. The latter give higher condensation temperatures because the associated solution model in MAGMA computes  $\gamma(\text{SiO}_2) < 1$ . Molten SiO<sub>2</sub> has activity coefficients near unity with either positive or negative deviations from ideality (Ryerson, 1985; Turkdogan, 1983) and has a small partial molal enthalpy of solution that can be endothermic or exothermic (Morishita et al., 2004; Wilding and Navrotsky, 1998) depending on temperature and melt composition.

Fig. 7 shows the Si condensation curve imposed on graphs of SiO/SiO<sub>2</sub> molar ratios and SiO/Si molar ratios. The calculations include Si, Si<sup>+</sup>, Si<sup>2</sup>, Si<sub>2</sub>, Si<sub>2</sub>, Si<sub>3</sub>, SiO, and SiO<sub>2</sub>; but SiO and SiO<sub>2</sub> are the only important gases and SiO is always dominant along the condensation curve in the dry and wet models. Fig. 7b shows SiO is orders of magnitude more abundant than Si in the vicinity of the condensation curve. Unlike calcium, magnesium, and aluminum, monatomic silicon vapor is never important for gas – melt equilibria. Several KEMS studies show SiO is the major Si-bearing gas over molten silicates at low pressures (e.g., DeMaria et al., 1971; Markova et al., 1986; Stolyarova et al., 1996; Costa et al., 2017)

#### 3.3.7. Iron

CONDOR calculations included FeO, Fe $_3O_4$ , and Fe $_2O_3$  with FeO having the largest activity. The FeO/FeO $_{1.5}$  ratio along the 50% condensation curve varies from 35 (1818 K,  $10^{-6}$  bar) to 540 (4599 K,  $10^2$  bar). FactSage calculations give smaller FeO/FeO $_{1.5}$  ratios, e.g., 30 (3300 K, 1 bar) vs. 228 (3284 K, 1 bar) than CONDOR. The differences arise from differences in thermodynamic data for the pure liquid oxides and their solution parameters, which are magnified because of the exponential dependence of equilibrium constants on  $\Delta G^\circ$  values.

Fig. 8a shows the 50% condensation curve for FeO computed using FeO activity coefficients from Table 2 and comparison with the Lock et al. (2018) ideal solution values. The small temperature coefficients of  $\gamma$ (FeO) values in Table 2 are consistent with the small temperature dependence of FeO activity coefficients in CMAS melts (Holzheid et al., 1997)

Table 6 and Fig. 8a show the 50% condensation temperatures for FeO agree well with one another and with ideal solution calculations at low pressures but increasing disagreement with increasing pressure, reaching 230 K (5%) at 100 bar. Condensation temperatures from the MAGMA code are always higher because the associated solution model in MAGMA computes  $\gamma(\text{FeO}) < 1$  versus  $\gamma(\text{FeO}) \geq 1$  from ideal solution and the Ban-Ya and FactSage models. However, Figs. 7 and 8 of Schaefer and Fegley (2004) display good agreement between MAGMA code calculations and experimental measurements for the amounts of FeO left in vaporization residues as a function of the fraction vaporized for two chondritic compositions (Hashimoto, 1983; Wang et al., 2001) and an Apollo 16 lunar basalt (Markova et al., 1986). Schaefer and Fegley (2004) found good agreement for all other oxides in both the experiments and MAGMA code (SiO<sub>2</sub>, MgO, CaO, Al<sub>2</sub>O<sub>3</sub>, and TiO<sub>2</sub>).

Fig. 8b displays the FeO 50% condensation curve superimposed on logarithmic contours of the Fe/FeO gas molar ratios. Monatomic Fe is the major gas along the condensation curve and Fe/FeO ratios vary from  $\approx 10$  at lower pressures to  $\approx 2$  at higher pressures in the dry and wet models. The calculations also include Fe<sup>+</sup>, Fe<sup>2+</sup>, and Fe<sup>-</sup>, which are insignificant. Gas – melt chemical equilibrium calculations for a Type B1 CAI composition (Schaefer and Fegley, 2004) and for chondrule melts (Ebel, 2005) give similar results. KEMS studies of saturated vapor over molten silicates show Fe is the major Fe-bearing gas and FeO is less abundant (Dhima et al., 1986; Markova et al., 1986; Costa et al., 2017).

### 3.3.8. Titanium

CONDOR calculations included TiO,  $\rm Ti_2O_3$ ,  $\rm Ti_3O_5$ ,  $\rm Ti_4O_7$ , and  $\rm TiO_2$ , which has the largest activity. The  $\rm TiO_2/\rm TiO_{1.5}$  ratio varies from 6 (1882 K,  $\rm 10^{-6}$  bar) to 0.35 (4778 K,  $\rm 10^2$  bar) along the 50% condensation

curve. FactSage calculations give different values for the  $\rm TiO_2/TiO_{1.5}$  ratio, e.g., 33 vs. 0.75 (CONDOR) at 3433 K, 1 bar. The melting point, enthalpy of fusion, and liquid heat capacity of titanium oxides are different in different databases (e.g., JANAF and IVTAN); titanium condensation was modeled as dissolution of  $\rm TiO_2$  (liq) in the BSE melt.

Fig. 9a shows 50% condensation calculations using the TiO<sub>2</sub> activity coefficients in Table 2 and comparison with the Lock et al. (2018) ideal solution values. Table 7 and Fig. 9a show good agreement between the real solution TiO<sub>2</sub> 50% condensation temperatures within 110–150 K (about 5%) over the  $10^{-6}$  to  $10^2$  bar range. The MAGMA code results are always higher because the associated solution model in MAGMA computes  $\gamma(\text{TiO}_2) < 1$  but the FactSage  $\gamma(\text{TiO}_2)$  values shift from positive to negative deviations from ideality with increasing temperature instead of trending toward ideality as do the Ban-Ya and MAGMA code values.

Fig. 9b displays the  $TiO_2$  50% condensation curve superimposed on logarithmic contours of the  $TiO_2/TiO$  gas molar ratios. Titanium dioxide is the major gas along the condensation curve, TiO is less abundant, and Ti,  $Ti^+$ ,  $Ti^{2+}$ , and  $Ti^-$  are insignificant. DeMaria et al. (1971) found  $TiO \approx TiO_2$  and Markova et al. (1986) found  $TiO \gtrsim TiO_2$  in their KEMS studies; however, these two studies are in the region where  $TiO/TiO_2 \ge 1$  at lower P and higher T than the thick red curve in Fig. 9b.

# 3.3.9. Manganese

CONDOR calculations included MnO, MnO<sub>2</sub>, and Mn<sub>3</sub>O<sub>4</sub> with MnO having the largest activity. FactSage calculations included Mn<sub>2</sub>O<sub>3</sub> (but not Mn<sub>3</sub>O<sub>4</sub>). Neither IVTAN, JANAF, nor Robie and Hemingway (1995) give data for Mn<sub>2</sub>O<sub>3</sub> liquid and it is not considered in the CONDOR code calculations. Fig. 10a is the 50% condensation curve for MnO dissolving in the BSE melt. The black curve is the Ban-Ya (1993) model. Fig. 10a and Table 8 show good agreement between the Ban-Ya, FactSage, and ideal solution models. Fig. 10b overlays the MnO 50% condensation curve on logarithmic contours of constant Mn/MnO gas molar ratios. Manganese monoxide is the major gas along the condensation curve at higher pressure and Mn is the major gas at lower pressure. The KEMS results of Zaitsev and Mogutnov (1995) show monatomic Mn is the major Mn-bearing gas over MnO-SiO<sub>2</sub> melts in the 1369–1817 K range at low pressures in agreement with Fig. 10b.

# 3.3.10. Chromium

CONDOR calculations included  $Cr_2O_3$  but not CrO because there are no tabulated data for CrO (s, liq) in IVTAN, JANAF, or Robie and Hemingway (1995). Toker et al. (1991) and Pretorius and Muan (1992) give data for pure CrO (liquid) and its activity coefficients in CaO –  $Al_2O_3$  –  $CrO_x$  –  $SiO_2$  melts, but including CrO (s, liq) in the CONDOR code is beyond the scope of this work and chromium condensation was computed as  $Cr_2O_3$  dissolution in BSE melt as done by Lock et al. (2018).

Fig. 11a is the 50% condensation curve for  $Cr_2O_3$  dissolving in the BSE melt based on FactSage  $\gamma(Cr_2O_3)$  values in Table 2. Table 9 shows excellent agreement between the 50% condensation temperatures in the dry and wet BSE models and good agreement with ideal solution results within 1–100 K ( $\leq$ 2%) from  $10^{-6}$  to  $10^2$  bar total pressure. Ivanov et al. (2022) used the FactSage code and give a 50% condensation temperature of 3346 K at one bar total pressure. Using the FactSage code, which includes CrO (liquid), we obtained a similar value of 3358 K at one bar total pressure and a molar ratio of  $\simeq$ 0.3 for  $CrO_{1.5}/CrO$  at the 50% condensation temperature. This is 162 K higher than the 50% condensation temperature 3196 K computed by CONDOR using FactSage activity coefficients for  $Cr_2O_3$ .

Chromium gas chemistry is complex and Cr, Cr $^+$ , CrO, CrO $_2$ , and CrO $_3$  are included in the calculations. The four most abundant Crbearing gases along the condensation curve are CrO $_2 \gtrsim$  CrO > Cr > CrO $_3$ . This is the same sequence as Grimley et al. (1961) found over Cr $_2$ O $_3$  under oxidizing conditions in his KEMS study.

# 3.3.11. Sodium

Fig. 12a shows the 50% condensation curve for Na<sub>2</sub>O dissolving in

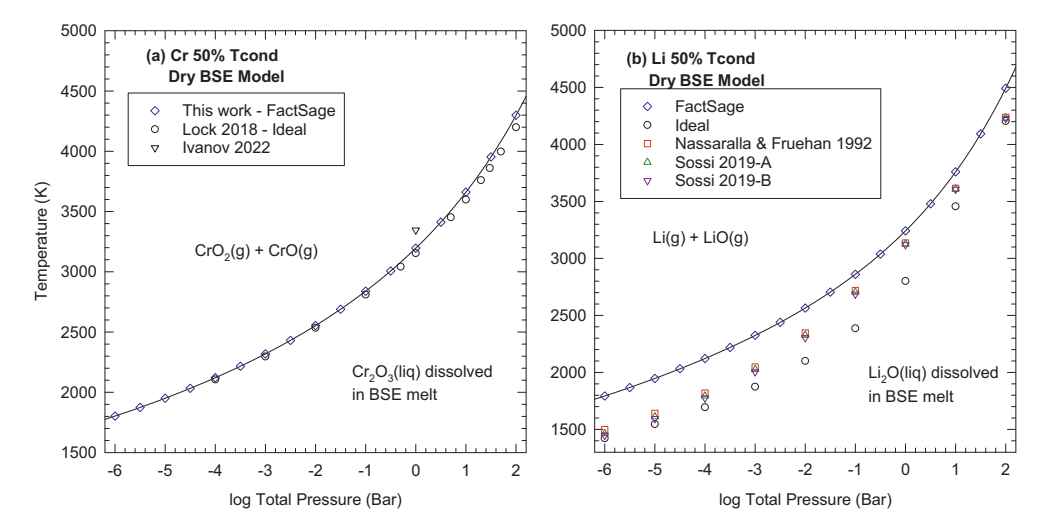


Fig. 11. (a) Chromium equilibrium chemistry in BSE material as a function of temperature and total pressure. The black curve is the 50% condensation curve for chromium. (b) Lithium equilibrium chemistry in BSE material as a function of temperature and total pressure. The black curve is the 50% condensation curve for lithium.

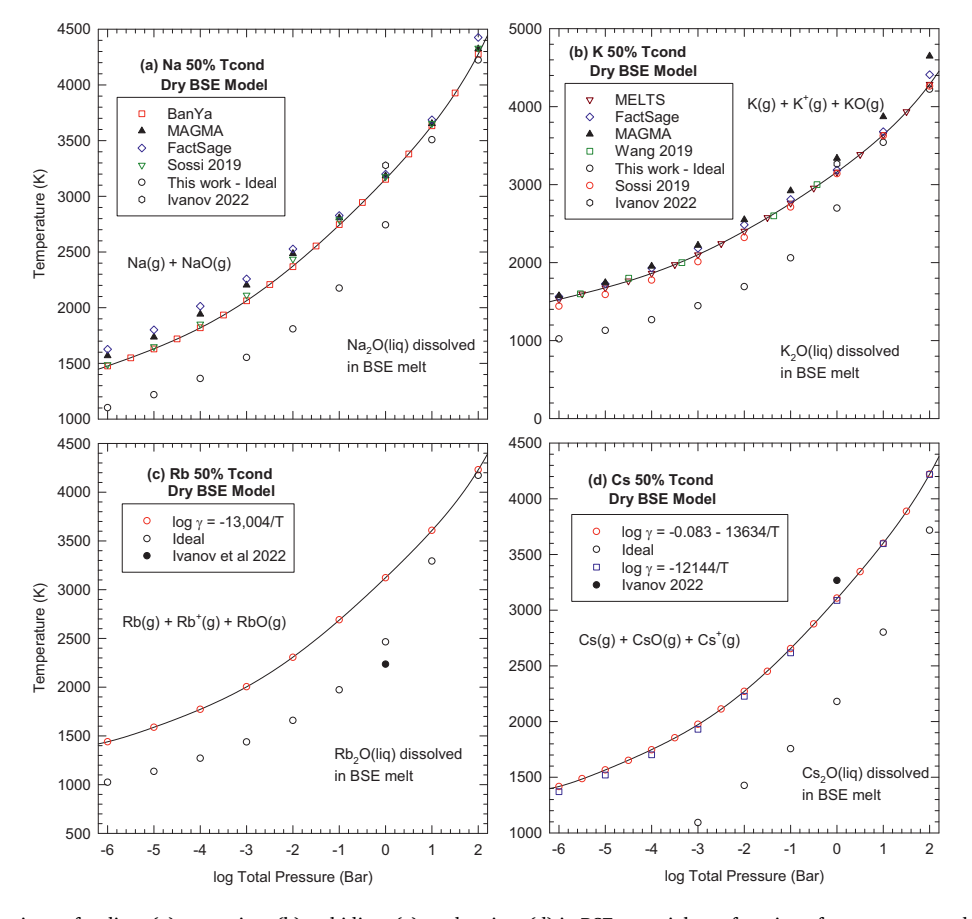


Fig. 12. Equilibrium chemistry of sodium (a), potassium (b), rubidium (c), and cesium (d) in BSE material as a function of temperature and total pressure. The black curves are the 50% condensation curves. See the text for a detailed discussion of this figure.

the BSE melt based on the Ban-Ya model and comparison with similar calculations using activity coefficients from Sossi et al. (2019), the FactSage and MAGMA code models (see Table 2) and our ideal solution values. Fig. 12a and Table 10 show 50% condensation temperatures from the four activity coefficient models agree within 45–190 K (1–11%) with 50% condensation temperatures from the MAGMA code values intermediate between those from FactSage (high) and Ban-Ya (low) and

better agreement at higher pressures. The ideal solution condensation temperatures from Lock et al. (2018) and this work are significantly lower than the real solution values because Na<sub>2</sub>O has large negative deviations from ideality in binary, ternary, and more complex silicate melts (Charles, 1967; Gaskell, 1989; Itoh and Yokokawa, 1984; Lambotte and Chartrand, 2013; Mathieu et al., 2008, 2011; Sossi et al., 2019; Zaitsev et al., 1999).

The chemical equilibrium calculations include Na, Na<sup>+</sup>, Na<sup>-</sup>, Na<sub>2</sub>, NaBO<sub>2</sub>, NaK, NaO, Na<sub>2</sub>O, and Na<sub>2</sub>O<sub>2</sub> but only Na and NaO are important. Monatomic Na is the major gas along the condensation curve with Na/NaO ratios increasing from  $\simeq$ 3 at 100 bar to  $\simeq$ 10<sup>4</sup> at 10<sup>-6</sup> bar. The KEMS studies of molten basalt vaporization by DeMaria et al. (1971) and Markova et al. (1986) show monatomic Na is the major sodium gas in agreement with our calculations.

#### 3.3.12. Potassium

Fig. 12b shows the 50% condensation curve for K<sub>2</sub>O dissolving in the BSE melt based on the MELTS activity coefficients and comparisons with similar calculations using the three other activity coefficient models in Table 2, our ideal solution values, and results from Wang et al. (2019). Fig. 12b and Table 11 show 50% condensation temperatures from the four activity coefficient models agree within 133-385 K with the FactSage values intermediate between the higher MAGMA and lower values from our regular solution fit to the 1673 K point of Sossi et al. (2019). The disagreement increases with increasing total pressure. The ideal solution temperatures of Lock et al. (2018) and this work are much lower than those for the real solution models as expected from the large negative deviations from ideality displayed by K<sub>2</sub>O in binary, ternary, and higher order silicate melts (Charles, 1967; Hastie et al., 1982; Sossi et al., 2019; Yazhenskikh et al., 2011; Zaitsev et al., 2000a, 2000b). Fig. 12b also shows good agreement between the present work and the results of Wang et al. (2019).

The chemical equilibrium calculations include K,  $K^+$ ,  $K_2$ , KBO<sub>2</sub>, NaK, KO,  $K_2O$ , and  $K_2O_2$  but only K,  $K^+$ , and KO are important. Monatomic K gas is the major gas along the condensation curve with  $K^+$ , and KO the second and third most important gases. The KEMS studies of molten basalt vaporization by DeMaria et al. (1971) and Markova et al. (1986) show monatomic K is the major potassium gas in agreement with our calculations.

#### 3.3.13. Other elements

The remaining elements in the dry BSE model are systematically considered starting with alkalis in group 1 and ending with actinides (Th, U, Pu). As discussed earlier, we exclude H, C, N, F, Cl, Br, I, S, Se, and Te from consideration because their solubilities and activity coefficients in molten silicates are not well known, but must be considered for their correct equilibrium distribution, 50% condensation temperatures, and mass balance. This is beyond the scope of this paper but is planned for subsequent calculations for a wet BSE model.

The gas phase speciation over the BSE melt for many elements is similar to that in the saturated vapor over their respective pure oxides, e. g., Ca, Al, Mg, Si, Fe, Ti, Mn, Cr, Na, and K. However, there are significant changes for elements such as As, B, Cs, Ga, In, Li, Mo, P, Re, Sb, Tl, V, and W. For example, the saturated vapor over pure oxides of As, B, Li is dominated by gaseous  $As_4O_6$ ,  $B_2O_3$ , and  $Li_2O$ , but over the BSE melt the dominant gases of As, Ga, and Li are AsO, Ga, and Li, respectively. These changes occur because the gas chemistry of all elements is coupled and (in particular) because the fO<sub>2</sub> of the BSE melt is superimposed onto the gas phase equilibria of individual minor and trace elements. This is described in the Lithium section below.

Activity coefficient models or estimates were used for several elements (Li, Rb, Cs; V, Mo, W) but ideal solution calculations were done for other elements where estimates of activity coefficients in BSE melt were not done for various reasons (Be, Sr, Ba; Sc, Y, La; the rare earth elements REE; Zr, Hf; Nb, Ta; Re; Ru, Os; Rh, Ir; Pd, Pt, Au, Hg; Th, U, Pu). Most of the latter elements are lithophile refractory or siderophile trace elements (Kornacki and Fegley, 1986).

# 3.3.14. Group 1 (Li, Rb, Cs)

Sodium and potassium were discussed earlier; lithium, rubidium, and cesium are considered now. Several measurements show negative deviations from ideality increasing from Li<sub>2</sub>O to Na<sub>2</sub>O to K<sub>2</sub>O; a smaller number of measurements show the trend continues from K<sub>2</sub>O to Rb<sub>2</sub>O to

Cs<sub>2</sub>O. This is seen from alkali oxide activities derived from phase diagrams for Li<sub>2</sub>O-SiO<sub>2</sub>, Na<sub>2</sub>O-SiO<sub>2</sub> and K<sub>2</sub>O-SiO<sub>2</sub> melts (Charles, 1967), Langmuir vaporization measurements of alkali oxide activities (Li, Na, K, Rb) in basaltic melt (Sossi et al., 2019), the partial molal enthalpy of solution for SiO<sub>2</sub> in Li, Na, K, and Cs oxide - silica binary melts (Morishita et al., 2004), and the position of silica liquidus curves in binary alkali oxide - silica melts (Rey, 1948). Increasing optical basicity (Duffy, 2004) and decreasing cationic potential (Z/r), which relate to electronegativity and metal - oxygen bond strengths, suggest increasingly negative deviations from ideality downward in group 1 from Li to Cs. Smooth, often linear correlations between optical basicity and log  $\gamma$ (oxide) in melts exist for CaO, MgO, SiO<sub>2</sub>, Al<sub>2</sub>O<sub>3</sub>, Na<sub>2</sub>O and P<sub>2</sub>O<sub>5</sub> (Duffy et al., 1978; Gaskell, 1989; Beckett, 2002; Mathieu et al., 2011).

#### 3.3.15. Lithium condensation

Fig. 11b and Table 12 compare the 50% condensation temperatures for Li<sub>2</sub>O computed using the four sets of activity coefficients in Table 2 and ideal solution. Li<sub>2</sub>O, like Na<sub>2</sub>O and K<sub>2</sub>O, has negative deviations from ideality in binary melts with SiO<sub>2</sub> although the database is smaller (Charles, 1967; Shakhmatkin and Vedishcheva, 1994). Sossi et al. (2019) report positive deviations from ideality, which is consistent with the known immiscibility in some regions of the Li<sub>2</sub>O - SiO<sub>2</sub> - Al<sub>2</sub>O<sub>3</sub> system (e.g., Konar et al., 2018). Nassaralla and Fruehan (1992) measured  $\gamma(\text{Li}_2\text{O}) = 0.05$  at 1573 K in a CaO - Al<sub>2</sub>O<sub>3</sub> - CaF<sub>2</sub> - Li<sub>2</sub>O melt. Sossi et al. (2019) measured two different  $\gamma(\text{Li}_2\text{O})$  values at 1673 K; one for fO<sub>2</sub> =  $10^{-8}$  bar and one in air. The large spread of condensation temperatures shows the poor state of knowledge about Li<sub>2</sub>O activity coefficients in multicomponent silicate melts.

# 3.3.16. Lithium gas chemistry

Monatomic Li and LiO are the two major Li-bearing gases and Li (g) is the major species along the condensation curve. KEMS studies of Li<sub>2</sub>SiO<sub>3</sub>, Li<sub>2</sub>TiO<sub>3</sub>, and Li<sub>2</sub>ZrO<sub>3</sub> vaporization (Asano and Nakagawa, 1989; Kato et al., 1993; Nakagawa et al., 1982) show monatomic Li and the less abundant LiO are the major lithium gases in agreement with the calculations for saturated vapor over BSE melt. But this is different than in saturated vapor over pure Li<sub>2</sub>O where Li<sub>2</sub>O  $\gtrsim$  Li > LiO with minor amounts of Li<sub>3</sub>O and Li<sub>2</sub>O<sub>2</sub> (Table 1, Sossi and Fegley, 2018). The difference arises because the fO<sub>2</sub> of saturated Li<sub>2</sub>O vapor is different than that over the BSE melt and because the partial pressure of Li<sub>2</sub>O (g) is independent of oxygen fugacity.

The major vaporization reactions, equilibrium constants, and gas partial pressures are

$$Li_2O\left(s,liq\right) = Li_2O\left(g\right)$$

$$K_{Li_2O} = \frac{P_{Li_2O}}{a_{Li_2O(s,liq)}} \label{eq:KLi2O}$$

$$P_{Li_2O} = K_{Li_2O} {\cdot} a_{Li_2O(s,liq)}$$

$$Li_2O(s, liq) = 2 Li(g) + \frac{1}{2} O_2(g)$$

$$K_{Li} = \frac{P_{Li}^2 f_{O_2}^{1/2}}{a_{Li_2O(s,liq)}}$$

**Table 12**Li 50% condensation temperatures – real and ideal models.

Log P (bar)	FactSage	NF92	Sossi-A	Sossi-B	Ideal
-6	1793	1499	1463	1447	1422
-4	2122	1819	1794	1775	1694
-2	2564	2346	2326	2304	2100
0	3242	3135	3127	3119	2801
2	4493	4238	4233	4228	4205
-2 0	2564 3242	2346 3135	2326 3127	2304 3119	2100 2801

NF-92: Nassaralla and Fruehan (1992). Sossi-A:  $LiO_{.5} \gamma = 1.8$ , Sossi-B:  $LiO_{.5} \gamma = 15.4$ , both at 1673 K from Sossi et al. (2019).

$$P_{Li} = \frac{\left(K_{Li} \!\cdot\! a_{Li_2O(s,liq)}\,\right)^{1/2}}{f_{O_2}^{1/4}}$$

$$Li_2O(s, liq) = LiO(g) + Li(g)$$

$$K_{LiO} = \frac{P_{LiO}P_{Li}}{a_{Li_2O(s,liq)}}$$

$$P_{LiO} = \frac{K_{LiO} \cdot a_{Li_2O(s,liq)}}{P_{Li}} = \frac{K_{LiO} \cdot f_{O_2}^{1/4}}{K_{1:i}^{1/2}}$$

Some thermal dissociation of O2 occurs via

$$O_2(g) = 2O(g)$$

$$K_{O} = \frac{P_{O}^{2}}{P_{O_{2}}} = \frac{P_{O}^{2}}{f_{O_{2}}}$$

$$P_{O} = (K_{O} \cdot f_{O_{2}})^{1/2}$$

Neglecting the minor gases  ${\rm Li_3O}$ ,  ${\rm Li_2O_2}$ , and ions does not alter the conclusions.

A comparison of the  $\rm Li_2O$ ,  $\rm Li$ , and  $\rm LiO$  equilibrium partial pressures in saturated  $\rm Li_2O$  vapor (denoted by the subscript "pure") and in saturated BSE melt vapor (denoted by the subscript "BSE") is instructive. Starting with  $\rm Li_2O$  gas,

$$\frac{P_{\text{Li2O,BSE}}}{P_{\text{Li2O,pure}}} = \frac{X_{\text{Li2O,BSE}} \cdot \gamma_{\text{Li2O,BSE}}}{a_{\text{Li2O,pure}}} = X_{\text{Li2O,BSE}} \cdot \gamma_{\text{Li2O,BSE}}$$

The Li<sub>2</sub>O partial pressure over the BSE melt is independent of the fO<sub>2</sub> of melt vapor but is proportional to the Li<sub>2</sub>O mole fraction in the melt, which is about  $6\times 10^{-6}$  (see Table 1). Unless the Li<sub>2</sub>O activity coefficient is  $\gg 1$ , the Li<sub>2</sub>O activity in the melt is  $\ll 1$  and the Li<sub>2</sub>O partial pressure is lower than that over pure Li<sub>2</sub>O which has an activity of unity.

The Li and LiO equilibrium partial pressure ratios are

$$\frac{P_{\text{Li,BSE}}}{P_{\text{Li,pure}}} = \left(X_{\text{Li2O,BSE}} \bullet \gamma_{\text{Li2O,BSE}}\right)^{1/2} \left(\frac{f_{\text{O_2,pure}}}{f_{\text{O_2,BSE}}}\right)^{1/4}$$

$$\frac{P_{\text{LiO,BSE}}}{P_{\text{LiO,pure}}} = \left(X_{\text{Li2O,BSE}} \bullet \gamma_{\text{Li2O,BSE}}\right)^{1/2} \left(\frac{f_{O_2,\text{BSE}}}{f_{O_2,\text{pure}}}\right)^{1/4}$$

The partial pressure ratios of monatomic Li and LiO are both proportional to the square root of the Li<sub>2</sub>O activity in the BSE melt. However, their dependence on oxygen fugacity is different. At constant temperature, fO<sub>2,pure</sub> over pure Li<sub>2</sub>O is constant while fO<sub>2,BSE</sub> for the BSE melt can be variable. For the case of fO<sub>2,BSE</sub> > fO<sub>2,pure</sub>, the LiO partial pressure ratio decreases (proportional to the 4th root of the fO<sub>2</sub> ratio (BSE/pure), whereas the monatomic Li gas partial pressure ratio increases by the same factor. Conversely for fO<sub>2,BSE</sub> < fO<sub>2,pure</sub>, the LiO partial pressure ratio increases and that of monatomic Li decreases.

The oxygen fugacity  $fO_{2,pure}$  in saturated vapor over pure  $\text{Li}_2O$  is fixed at any temperature by stoichiometry and is

$$f_{O2,pure} = \frac{1}{4} \left( P_{Li,pure} - P_{LiO,pure} - 2 P_{O,pure} \right).$$

However,  $fO_{2,BSE}$  is not controlled by trace  $Li_2O$  evaporation but instead comes from evaporation and dissociation of major oxides such as  $SiO_2$  from the melt. There is no simple expression for  $fO_{2,BSE}$  because several evaporating oxides can contribute oxygen to the vapor phase and non-linear coupled equations for all gas species equilibria must be solved simultaneously.

#### 3.3.17. Rubidium

The activity coefficient data of Sossi et al. (2019) for  $Rb_2O$  in molten ferrobasalt seem to be the only data for  $\gamma(Rb_2O)$  in multicomponent

silicate melts. The nominal value for  $\gamma(Rb_2O)$  is a regular solution extrapolation of the 1673 K point of Sossi et al. (2019) for a synthetic ferrobasalt. This regular solution equation was used because a linear least square fit of log  $\gamma$  vs. 1/T to all three Rb data points in Table 4 of Sossi et al. (2019) gave increasingly negative deviations from ideality with increasing temperature, which is unreasonable.

Initially we used the published  $Rb_2SiO_3 - SiO_2$  phase diagram of Alekseeva (1963) to estimate an equation for  $\gamma(Rb_2O)$  from the eutectic reaction between  $Rb_2Si_4O_9$ ,  $Rb_2O$  (melt), and  $SiO_2$  (quartz), and derived  $log \gamma(Rb_2O) = -15,200$ /T using data from Knacke et al. (1991). However, Lapshin et al. (2006a) claim the phase diagram is incorrect because they crystallized (and identified via X-ray diffraction)  $Rb_6Si_{10}O_{23}$  from glass with the composition  $Rb_2Si_4O_9$ . These two silicates have similar Rb/Si molar ratios of 0.25 ( $Rb_2Si_4O_9$ ) versus 0.30 ( $Rb_6Si_{10}O_{23}$ ). Kracek (1933) published the liquidus curve for the  $Rb_2Si_2O_5 - SiO_2$  part of the phase diagram and he does not find the existence of a tetrasilicate. We do not use either our thermodynamic analysis of the  $Rb_2SiO_3 - SiO_2$  phase diagram or that of Kim and Sanders (1991).

Fig. 12c and Table 13 compare the Rb 50% condensation temperatures for our real and ideal solution models. The ideal solution is a strict lower limit although the nominal activity coefficient equation may not give an upper limit to the 50% condensation temperatures if the "true"  $Rb_2O$  activity coefficients are even smaller, i.e., larger negative deviations from ideality.

The chemical equilibrium calculations considered nine Rb-bearing gases (Rb, Rb $^+$ , Rb $^-$ , Rb2, RbK, RbBO2, RbO, Rb2O, and Rb2O2) but only Rb, Rb $^+$ , and RbO are significant with Rb more important. Rubidium gas chemistry in BSE material is like that in the saturated vapor over liquid Rb2O because Rb is the major gas in both cases (see Table 1 of Sossi and Fegley, 2018). A KEMS study of Rb2O – B2O3 – SiO2 melt vaporization shows Rb is the major gas (Lopatin et al., 2007) for Rb2O/B2O3 ratios >1. Molecular gases such as Rb2O and Rb2O2 are less important in BSE vapor as expected from the discussion of Li2O vaporization.

# 3.3.18. Cesium

Little is known about thermodynamic properties of Cs<sub>2</sub>O-bearing silicate melts. Borisov (2009) measured relative activity coefficients of alkali oxides in aluminosilicate melts and found  $\gamma(Cs_2O)$  just below  $\gamma(Rb_2O)$  and a few times smaller than  $\gamma(Na_2O)$ . The existence of two Cs—Na silicates in the Cs<sub>2</sub>O – SiO<sub>2</sub> – Na<sub>2</sub>O system (CsNaSiO<sub>3</sub> and CsNaSi<sub>2</sub>O<sub>5</sub>) means there are negative deviations from ideality between Na<sub>2</sub>O and Cs<sub>2</sub>O in the ternary system (Bennour et al., 1996a). Bennour et al. (1996b, 1999) studied mixing in Cs<sub>2</sub>O - SiO<sub>2</sub> - Na<sub>2</sub>O melts by KEMS and successfully modeled their data using the interaction parameters  $W_{Cs\text{-Si}} = -232,500 \text{ J} \text{ mol}^{-1}$ , and  $W_{Cs\text{-Na}} = 0 \text{ J} \text{ mol}^{-1}$ . The  $W_{Cs\text{-Si}}$  parameter corresponds to log  $\gamma(Cs_2O) = -12,144/T$ .

The situation with the  $Cs_2O-SiO_2$  phase diagram of Alekseeva (1966) is like that above for the  $Rb_2SiO_3-SiO_2$  phase diagram. Initially we estimated  $\gamma(Cs_2O)$  from the eutectic reaction between  $Cs_2Si_4O_9$ ,  $Cs_2O$  (melt), and  $SiO_2$  (quartz), and derived  $log \ \gamma(Cs_2O) = -13,700/T$  with data from Knacke et al. (1991). Then we found Lapshin et al. (2006b) who claim the  $Cs_2O-SiO_2$  phase diagram of Alekseeva (1966) is

**Table 13**Rb, Cs 50% condensation temperatures – real and Ideal.

Log P (bar)	Real	Real			Ideal		
	Rb	Rb Cs-1 Cs-2		Rb	Cs		
-6	1439	1416	1371	1024	626		
-4	1772	1746	1702	1270	864		
-2	2305	2270	2227	1658	1426		
0	3122	3108	3088	2464	2802		
2	4230	4221	4218	4172	3718		

Real solution models: Cs-1: log  $\gamma = -0.083 - 13,634.1/T$ . Cs-2: log  $\gamma = -12,144/T$ .

incorrect because they crystallized (and identified)  $Cs_6Si_{10}O_{23}$  from glass with the composition  $Cs_2Si_4O_9$ . Suzuki et al. (2020) synthesized and measured the X-ray diffraction pattern of  $Cs_2Si_4O_9$ , found some discrepancies with the XRD pattern of Alekseeva (1966), but used the sample for low temperature heat capacity measurements and published data for  $Cs_2Si_4O_9$  thermal properties from 0 to 300 K. Cordfunke and Ouweltjes (1993) published the standard enthalpy of formation for  $Cs_2Si_4O_9$  at 298 K. Whether or not  $Cs_2Si_4O_9$  exists, we do not use either our thermodynamic analysis of the  $Cs_2O - SiO_2$  phase diagram or that of Kim and Sanders (1991) in our work.

Cesium is an instance where analogy to molten salts (of elements in the same group of the periodic table) helped to estimate the activity coefficient. Molten Cs and Na fluorides were used because of (1) the similar VI coordinate radii of oxide (140 pm) and fluoride (133 pm) ions (Shannon, 1976), (2) the oxide  $O^{2-}$  and fluoride  $F^{1-}$  ions are isoelectronic, and (3) ideal (or nearly so) Temkin mixing of fluoride ions with oxide ions is documented for PbO-PbF<sub>2</sub>, (Jeffes and Sridhar, 1968) CaO-CaF<sub>2</sub>, and MgO-MgF<sub>2</sub> (Kim et al., 2012). Lumsden (1966) derived log<sub>10</sub>  $\gamma^{\circ} = 175/T$  for CsF dilute solution in molten NaF; a small positive deviation from ideality. Based on the work of Borisov (2009) suggesting  $\gamma(Cs_2O) < \gamma(Na_2O)$ , Bennour et al. (1996b, 1999) suggesting  $\gamma(Cs_2O) =$  $\gamma(Na_2O)$ , and Lumsden (1966) suggesting  $\gamma(Cs_2O) > \gamma(Na_2O)$ , we adopted an equation setting  $\log \gamma(Cs_2O) = \log \gamma(Na_2O)$  from FactSage (see Table 2). This equation gives  $\gamma(Cs_2O) < \gamma(Na_2O)$  from the Ban-Ya (1993) equation for  $\log \gamma(\text{Na}_2\text{O})$  in Table 2. Table 13 and Fig. 12d show the 50% condensation temperatures and condensation curve for Cs<sub>2</sub>O using the two estimated activity coefficient equations and comparison to ideal solution. The ideal solution 50% condensation temperatures at  $10^{-6}$  to  $10^{-2}$  bar for cesium are below the solidus temperature of peridotite; the same is true for Li at  $10^{-6}$  bar and for Na, K, and Rb at  $10^{-6}$  to  $10^{-4}$  bar.

Nine Cs-bearing gases are included in the chemical equilibrium calculations: Cs, Cs $^+$ , Cs $^-$ , Cs $_2$ , CsBO $_2$ , CsO, Cs $_2$ O, Cs $_2$ O $^+$ , and Cs $_2$ O $_2$ , but only Cs, Cs $^+$ , and CsO are significant with Cs dominant along the condensation curve. The KEMS study of crystalline cesium aluminosilicates by Odoj and Hilpert (1980a, 1980b) showed Cs is the major Csbearing gas. Cesium gas chemistry in BSE material is different than the speciation in saturated vapor over liquid Cs $_2$ O in which Cs $_2$ O is the major gas (Table 1, Sossi and Fegley, 2018). The difference is due to the same reasons that discussed above for lithium.

#### 3.3.19. Group 2 (alkaline earths Be, Mg, Ca, Sr, Ba)

Table 6 and Figs. 4a, c, and 5 give the results for Ca and Mg gas chemistry and real and ideal solution 50% condensation temperatures into BSE melt. Table 14 summarizes ideal solution 50% condensation temperatures for all alkaline earth oxides dissolved in BSE melt and shows BeO is the most refractory alkaline earth oxide in BSE melt assuming ideal solution.

The existence of Be<sub>2</sub>SiO<sub>4</sub> (phenakite), BeAl<sub>2</sub>O<sub>4</sub> (chrysoberyl), and Al<sub>2</sub>Be<sub>3</sub>Si<sub>6</sub>O<sub>18</sub> (beryl) suggests  $\gamma$ (BeO) < 1. We did not try to constrain the BeO activity coefficient using periodic trends because beryllia (BeO) does not have the NaCl crystal structure as do the other alkaline earth oxides. It has the wurtzite structure like zincite (ZnO). Chemically, Be is more like Al than the alkaline earths, and its optical basicity ( $\Lambda$  = 0.48) is closer to that of Al<sub>2</sub>O<sub>3</sub> ( $\Lambda$  = 0.60) than to other alkaline earth oxides (Lebouteiller and Courtine, 1998). The optical basicity of BeO suggests

**Table 14**Alkaline Earth 50% condensation temperatures – ideal solution.

Log P (bar)	Ве	Mg	Ca	Sr	Ba
-6	2101	1817	1880	1866	1791
-4	2466	2135	2216	2203	2124
-2	2960	2592	2700	2695	2571
0	3645	3303	3448	3473	3303
2	4894	4561	4758	4894	4794

amphoteric behavior in melts (Navrotsky, 1994).

Negative deviations from ideality are expected for SrO and BaO in BSE melt because of (1) the existence of Sr and Ba aluminates, aluminosilicates, and titanates, (2) KEMS measurements showing negative deviations from ideality for SrO and BaO in binary and ternary silicate melts (Lopatin et al., 2006; Stolyarova and Lopatin, 2005; Tyurnina et al., 2005), and (3) thermodynamic analyses of the SrO –  $SiO_2$  and BaO –  $SiO_2$  phase diagrams of Eskola (1922). However, the activity coefficients from the KEMS studies, the phase diagrams, and FactSage disagree enough that we did not use them and did ideal solution calculations for BaO and SrO.

The major alkaline earth gases in BSE vapor are Be  $\approx$  BeO, Mg, Ca, Sr  $\approx$  SrO, and BaO, which are the same as those in the saturated vapor over the pure alkaline earth monoxides (see Table 1, Sossi and Fegley, 2018). Note that Be does not follow the trend of decreasing M/MO gas ratios from Mg to Ba. The twelve Be-bearing gases in the chemical equilibrium calculations are Be, Be<sup>+</sup>, Be<sub>2</sub>, (BeO)<sub>1-6</sub>, Be<sub>2</sub>O, BeBO<sub>2</sub>, and BeB<sub>2</sub>O<sub>4</sub>. Monatomic Be and BeO are the two major gases along the 50% condensation curve; at one bar total pressure Be is 54.4%, BeO is 45.6%, and BeBO<sub>2</sub> is  $7 \times 10^{-4}$ % of all Be in the gas. The BeO gas polymers are unimportant. The BeO/Be ratio increases along the condensation curve to 2.1 at 4894 K, 100 bar pressure. The major Mg and Ca gases were discussed earlier. The major Sr-bearing and Ba-bearing gases along the SrO and BaO 50% condensation curves are Sr and SrO, and BaO. The SrO/Sr ratio increases from 0.40 to 4.2 and the BaO/Ba ratio decreases from 3400 to 28 from  $10^{-6}$  to  $10^2$  bar total pressure. The approximate equality of SrO and Sr and the dominance of BaO in BSE vapor are also seen in saturated vapor over solid SrO (1575-2100 K) and solid BaO (1200-1917 K).

# 3.3.20. Group 3 (Sc, Y)

Yttrium is similar to light rare earth elements (REE) and we mention studies relevant to REE below. Table 15 gives 50% condensation temperatures for ideal solution of Sc2O3 and Y2O3 in BSE melt. These temperatures are higher than the oxide 50% condensation temperatures in solar composition gas at the same total pressure (Kornacki and Fegley, 1986; Lodders, 2003). The necessary data for real solution calculations are unavailable. Evidence for negative deviation from ideality includes double oxide formation between group 3 oxides and CaO, phase diagrams for group 3 oxides with CaO, formation of group 3 and REE silicates, and KEMS studies of Sc<sub>2</sub>O<sub>3</sub>, Y<sub>2</sub>O<sub>3</sub>, and La<sub>2</sub>O<sub>3</sub> in oxide melts (e.g., Costa et al., 2019; Jacobson, 1989; Jacobson et al., 2001a; Stolyarova and Semenov, 1994; Stolyarova et al., 2020; Zhi et al., 2019). Evidence for positive deviations from ideality includes high-temperature liquid unmixing in the La<sub>2</sub>O<sub>3</sub> - SiO<sub>2</sub> and Y<sub>2</sub>O<sub>3</sub> - SiO<sub>2</sub> binary systems (Hageman and Oonk, 1986). The major gases of Sc and Y in BSE vapor are ScO and YO, which are the same as the major gases in saturated vapor over pure group 3 sesquioxides (Sossi and Fegley, 2018).

#### 3.3.21. Rare earth elements (REE, La to Lu)

Table 16 lists ideal solution 50% condensation temperatures for the REE, which are higher than the oxide 50% condensation temperatures in solar composition gas at the same total pressure (Kornacki and Fegley, 1986, Lodders, 2003). The necessary data for calculations are unavailable but non-ideal solution of the REE in BSE melt is expected because REE form compounds with the major oxides in BSE melt, e.g., oxyapatite

Table 15
Sc, Y, Ti, Zr, Hf, Th, U, Pu 50% condensation temperatures – ideal solution.

Log P (bar)	Sc	Y	Ti	Zr	Hf	Th	U	Pu
-6	2054	2060	1879	2159	2159	2067	1805	1924
-4	2352	2350	2192	2498	2498	2371	2129	2253
-2	2771	2759	2650	2960	2961	2806	2568	2733
0	3444	3430	3378	3645	3646	3520	3275	3459
2	4614	4578	4694	4894	4900	4837	4792	4685

**Table 16**REE 50% condensation temperatures – ideal solution.

Log P (bar)	La	Ce <sup>a</sup>	Pr	Nd	Sm	Eu <sup>b</sup>	Gd
-6	1850	1808	1841	1857	1864	1934	1910
-4	2147	2122	2141	2159	2167	2293	2207
-2	2565	2564	2562	2578	2584	2825	2624
0	3195	3229	3193	3209	3214	3645	3237
2	4270	4514	4268	4285	4280	4894	4289

Log P (bar)	Tb	Dy	Но	Er	Tm	Yb	Lu
-6	1964	1956	1952	1994	2017	1958	2012
-4	2256	2242	2236	2276	2288	2264	2286
-2	2690	2673	2662	2694	2733	2699	2694
0	3342	3300	3277	3327	3365	3341	3310
2	4433	4350	4320	4370	4384	4374	4333

a Ideal solution of CeO2 and Ce2O3.

compounds with CaO and SiO<sub>2</sub> (Costa et al., 2019), aluminates such as LaAlO<sub>3</sub>, and titanates such as CeTi<sup>3+</sup>O<sub>3</sub>. Different activity coefficients are expected for Ce<sub>2</sub>O<sub>3</sub> and CeO<sub>2</sub> and for EuO and Eu<sub>2</sub>O<sub>3</sub> dissolved in BSE melt because different activity coefficients are derived for Ce and Eu oxides dissolved in silicate melts at much lower temperatures (Johnston, 1965; Morris et al., 1974; Cachia et al., 2006; Burnham et al., 2015), but there are insufficient data to do calculations.

# 3.3.22. Group 4 (Ti, Zr, Hf)

Titanium chemistry was discussed earlier, and Table 7 and Fig. 9 give 50% condensation temperatures for non-ideal dissolution of TiO<sub>2</sub> in the BSE melt, a comparison to ideal solution results, and shows the major Tibearing gases. Table 15 compares ideal solution 50% condensation temperatures for TiO<sub>2</sub>, ZrO<sub>2</sub>, and HfO<sub>2</sub> in BSE melt. Zirconia and hafnia are more refractory than titania and are more than 50% condensed as soon as BSE melt forms. Fig. 13a shows the ideal solution 50% condensation curves for ZrO<sub>2</sub> and HfO<sub>2</sub> from  $10^{-6}$  to  $10^2$  bar total pressure. The major gases are ZrO<sub>2</sub> > ZrO and HfO > HfO<sub>2</sub>; monatomic Zr and Hf gases are insignificant. The HfO<sub>2</sub> (g) data have an uncertainty of  $\pm 30$  kJ mol<sup>-1</sup> and are of low accuracy (6-F class of the IVTAN database). The HfO<sub>2</sub> condensation calculations are preliminary because of the uncertain HfO<sub>2</sub> (g) thermodynamic data.

The necessary interaction coefficients to model non-ideal solutions of  $\rm ZrO_2$  and  $\rm HfO_2$  in BSE melt do not exist. However, negative deviations from ideality are expected for  $\rm ZrO_2$  and  $\rm HfO_2$  in BSE melt based on

existing calorimetry. Linard et al. (2008) measured  $\Delta H^{\circ}_{soln} = -20 \pm 3$  kJ mol $^{-1}$  at infinite dilution for HfO $_2$  solution in Na $_2$ O·3SiO $_2$  melt at 1733 K. Costa et al. (2018) found  $\Delta H^{\circ}_{soln} = -14.07 \pm 3.35$  kJ mol $^{-1}$  for solution of 7 mol% Y $_2$ O $_3$ - 93 mol% ZrO $_2$  in a CMAS melt at 1723 K. Both results indicate negative deviations from ideality but neither melt has identical composition to BSE melt. In contrast, Linard et al. (2008) found  $\Delta H^{\circ}_{soln} = +25.26$  kJ mol $^{-1}$  for TiO $_2$  solution in Na $_2$ O·3SiO $_2$  melt at 1731 K. An endothermic  $\Delta H^{\circ}_{soln}$  implies positive deviations from ideality, as seen for FactSage  $\gamma(TiO_2)$  values at lower temperatures in BSE melt.

# 3.3.23. Group 5 (V, Nb, Ta)

Table 17 gives 50% condensation temperatures for V (real and ideal solution), and ideal solution values for Nb, and Ta. The dioxides and monoxides are the major gases for V, Nb, and Ta. The MO<sub>2</sub>/MO ratios decrease from  $10^{-6}$  to  $10^2$  bar along the 50% condensation curves; from 10,750 to 34 for VO<sub>2</sub>/VO, from 23,800 to 23 for NbO<sub>2</sub>/NbO, and from 46,200 to 140 for TaO<sub>2</sub>/TaO. The following solid (liquid) oxides are in the condensation calculations: VO, V2O3, V2O4, and V2O5 for V, NbO, NbO<sub>2</sub>, and Nb<sub>2</sub>O<sub>5</sub> for Nb, and Ta<sub>2</sub>O<sub>5</sub> for Ta. Tantalum pentoxide Ta<sub>2</sub>O<sub>5</sub> is the only stable solid oxide of tantalum (Garg et al., 1996; Jacob et al., 2009). Table 2 shows the real solution vanadium condensation calculations use the estimates  $\gamma(VO) = \gamma(FeO)$  and  $\gamma(V_2O_3) = \gamma(Ti_2O_3)$ . Ideal solution condensation was used for the other V, Nb, and Ta oxides in the absence of reliable estimates. The existence of stable vanadates, niobates, and tantalates (Kubaschewski, 1972, Jacob and Rajput, 2015) implies negative deviations from ideality but the amphoteric V and Nb oxides and acidic Ta oxides may have positive interaction parameters ( $\alpha$ ) with SiO<sub>2</sub>, like Fe<sub>2</sub>O<sub>3</sub> and TiO<sub>2</sub> (amphoteric) and P<sub>2</sub>O<sub>5</sub> (acidic) with SiO<sub>2</sub> (Ban-Ya, 1993).

# 3.3.24. Group 6 (Cr, Mo, W)

Chromium chemistry in BSE material was discussed earlier (see Table 9 and Fig. 11a). The oxides  $MoO_2$ ,  $MoO_3$ , and  $WO_3$  are included in

**Table 17** Group 5 (V, Nb, Ta) 50% condensation temperatures.

Log P (bar)	V (real)	V (ideal)	Nb (ideal)	Ta (ideal)
-6	1729	1610	1858	1828
-4	2072	2043	2181	2124
-2	2533	2532	2654	2537
0	3190	3197	3410	3160
2	4354	4417	4825	4243

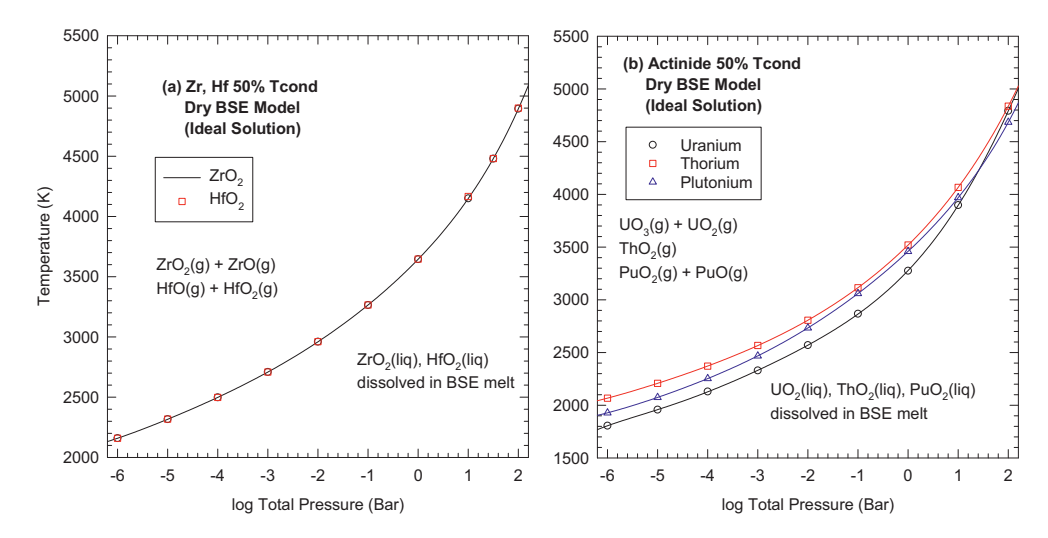


Fig. 13. (a) Equilibrium chemistry of zirconium and hafnium (a) and actinides (b) in BSE material as a function of temperature and total pressure. The black curves are the ideal solution condensation curves. See the text for a detailed discussion of this figure.

 $<sup>^{\</sup>rm b}$  Ideal solution of EuO and Eu<sub>2</sub>O<sub>3</sub>.

the calculations and their activity coefficients are estimated from basicity and ionic potential comparisons. Tungsten dioxide decomposes before melting and neither JANAF nor IVTAN gives thermodynamic data for WO<sub>2</sub> liquid. Only liquid WO<sub>3</sub> is considered in the calculations, which use JANAF data (Chase, 1998). Neglect of WO<sub>2</sub> liquid (not in either JANAF or IVTAN) does not introduce errors because O'Neill et al. (2008) report W<sup>6+</sup> (WO<sub>3</sub>) is the dominant tungsten species at fO<sub>2</sub> of  $10^{-11}$  bar in CMAS melts at 1673 K. An fO<sub>2</sub> of  $10^{-11}$  bar is five orders of magnitude lower than the lowest fO<sub>2</sub> in equilibrium with BSE melts in the P, T range we studied (see Fig. 3).

The optical basicity of  $MoO_2$  ( $\Lambda=0.96$ ) lies between FeO (1.00) and TiO<sub>2</sub> (0.75). The ionic potential for Mo<sup>4+</sup> is 6.15, closer to that of Ti<sup>4+</sup> (6.61) than to Fe<sup>2+</sup> (3.28). The geometric mean of FeO and TiO<sub>2</sub> activity coefficients was used as the nominal value for MoO2 in Table 2. Optical basicity values show WO<sub>3</sub> (0.51) and MoO<sub>3</sub> (0.52) are strong acids lying between SiO<sub>2</sub> (0.48) and Al<sub>2</sub>O<sub>3</sub> (0.60). The estimate  $\gamma(WO_3) = \gamma(SiO_2)$ was used because the optical basicity of WO<sub>3</sub> (0.51) and SiO<sub>2</sub> (0.48) are similar and the ionic potentials of W<sup>6+</sup> and Si<sup>4+</sup> are identical (10). The ionic potential of  $Mo^{6+}$  (10.2) is much closer to that of  $Si^{4+}$  (10) than that of Al<sup>3+</sup> (5.61). Two studies show  $\gamma(WO_3)$  is slightly smaller than y(MoO<sub>3</sub>). O'Neill et al. (2008) found the activity coefficient ratio  $\gamma(\text{MoO}_3)/\gamma(\text{WO}_3) \approx 4$  in CMAS melts at 1673 K. The EMF measurements of Lin and Elliott (1983, 2001) on Na<sub>2</sub>O - MoO<sub>3</sub> and Na<sub>2</sub>O - WO<sub>3</sub> melts give  $\gamma(\text{MoO}_3)/\gamma(\text{WO}_3)\approx 2$  at 1200 K. The MoO<sub>3</sub> activity coefficient  $\gamma(MoO_3)$  is set four times larger than  $\gamma(WO_3)$ , i.e., a smaller negative deviation from ideality.

Table 18 gives 50% condensation temperatures for real and ideal solution of Cr<sub>2</sub>O<sub>3</sub>, MoO<sub>2</sub> + MoO<sub>3</sub> and WO<sub>3</sub> in BSE melt. The real solution calculations show tungsten is the most refractory and molybdenum is the most volatile of the group 6 elements, except at 100 bar total pressure where Cr is more volatile than Mo. The major Mo-bearing gases are  $\text{MoO}_3 > \text{MoO}_2 > \text{MoO} \gg \text{Mo}$  with  $\text{Mo}_2\text{O}_6 \gtrsim \text{MoO}$  at the lowest total pressures. The major W-bearing gases follow a similar pattern:  $WO_3>$  $\text{WO}_2 > \text{WO} \gg \text{W}$  with  $\text{W}_2\text{O}_6 \gtrsim \text{WO}$  at the lowest total pressures. Condensation of Mo and W oxides dissolved in BSE melt occurs because Mo and W oxide gases are dominant while monatomic Mo and W are trace species. Along the 50% condensation curves from 10<sup>-6</sup> to 10<sup>2</sup> bar total pressure, the MoO<sub>3</sub>/Mo ratio varies from  $8 \times 10^{13}$  to  $2 \times 10^3$  and the WO<sub>3</sub>/W ratio varies from  $9 \times 10^{11}$  to  $3 \times 10^3$ . Molybdenum and W gas chemistry in BSE material is different than the speciation in saturated vapor over pure MoO2, MoO3, and WO3 (Table 1 of Sossi and Fegley, 2018) for the same reasons as discussed above for lithium.

3.3.25. Group 7 (Mn, Tc, Re), Group 8 (Fe, Ru, Os), Group 9 (Co, Rh, Ir), Group 10 (Ni, Pd, Pt)

These four groups are discussed together because their chemistry is similar, especially Mn and Fe; Co and Ni; Re, Ru, Os; and Rh, Ir, Pd, and Pt. The chemistry of Mn and Fe was discussed earlier. Table 6 and Fig. 8 show Fe chemistry and Table 8 and Fig. 10 show Mn chemistry. Experimental studies indicate noble metals (M) dissolve as oxides in silicate melts via redox sensitive reactions such as

$$M + \frac{x}{4}O_2 = MO_{x/2}(in \ melt)$$

Table 18
Group 6 (Cr, Mo, W) 50% condensation temperatures – real and ideal solution.

Log P (bar)	Real solution			Ideal sol	Ideal solution		
	Cr Mo W		Cr	Мо	W		
-6	1803	1527	1846	1802	1640	1815	
-4	2121	1921	2160	2113	2058	2132	
-2	2554	2496	2618	2540	2539	2584	
$0^a$	3196	3186	3356	3173	3211	3303	
2	4299	4376	4708	4253	4511	4625	

 $<sup>^{\</sup>rm a}$  Ivanov et al. (2022) report 3346 K (Cr), 3385 K (Mo), and 3337 K (W) 50% condensation temperatures at one bar total pressure.

(e.g., O'Neill and Nell, 1997; Borisov and Walker, 2000 and references therein). As discussed in Section 2, activity coefficients of the dissolved metal oxide liquids are needed to compute solubilities. Neither the melting points nor the enthalpies of fusion of noble metal oxides are known and solubility calculations cannot be done. However, 50% condensation temperatures of the stable condensates (either liquid metals or solid metal oxides) were computed to estimate noble metal volatility in BSE material.

*3.3.25.1. Technetium.* Technetium is unstable and the longest-lived isotopes (<sup>97</sup>Tc, <sup>98</sup>Tc) have half-lives of about 4.2 million years. Technetium chemistry is not considered because insufficient thermodynamic data exist to do so.

3.3.25.2. Rhenium, ruthenium, and osmium. These three elements are considered together because they form volatile oxide gases and as a result two competing factors affect their chemistry in BSE material. The first factor is their refractory nature, i.e., the low vapor pressure of metallic Re, Ru, and Os at a given temperature. The second factor is their high affinity for oxygen, i.e., the formation of well-known oxide gases such as Re<sub>2</sub>O<sub>7</sub> (rhenium heptoxide), RuO<sub>4</sub> (ruthenium tetroxide), and OsO<sub>4</sub> (osmium tetroxide) and solid oxides such as ReO<sub>2</sub>, RuO<sub>2</sub>, and OsO<sub>2</sub> (Pownceby and O'Neill, 1994; O'Neill and Nell, 1997). Mass spectrometric and other experimental studies show Re, Ru, and Os form monoxide, dioxide, and trioxide gases (e.g., Hildenbrand and Lau, 1992; Nuta et al., 2021; Skinner and Searcy, 1973; Watson et al., 1991). This complicates their chemistry at the high fO2 of the BSE melt - vapor system at 10<sup>-6</sup> to 10<sup>2</sup> bar total pressure and leads to consideration of multiple oxide gases and solids in the condensation calculations. Rhenium, ruthenium, and osmium condense as dioxide solids (Table 19). The data thermodynamic data used in the calculations are from Barin (1989), Fegley and Palme (1985), O'Neill and Nell (1997), and Pownceby and O'Neill (1994).

Initially the high volatility of Re, Ru, and Os in dry BSE material was surprising. However, Jacobson et al. (2001a, 2001b) found Re oxidized rapidly at 600–1400 °C (873–1673 K) in O2—Ar gas mixtures with fO2  $\geq$  3  $\times$  10 $^{-4}$  bar. Borisov and Jones (1999) found Re wire loops in gas mixing furnaces evaporate within a few hours at 1673 K at the fO2 of the quartz - fayalite - magnetite (QFM) oxygen fugacity buffer (fO2 = 3.6  $\times$  10 $^{-7}$  bar). Watson et al. (1991) reported that Os metal coatings on satellite optics decayed in low Earth orbit at O atom partial pressures of about 10 $^{-10}$  bar. Fig. 3 shows the fO2 at 1673 K in the dry BSE model is up to a factor of 5 lower than the total pressure below 10 $^{-3}$  bar and is about the same as the total pressure from 10 $^{-3}$  to 10 $^2$  bars.

We also wondered why similar behavior was not seen in earlier calculations about refractory metal nugget formation in Ca,Al-rich inclusions under oxidizing conditions (Fegley and Palme, 1985). The reason is that the oxygen fugacities in the dry BSE model are orders of magnitude higher than those in the metal nugget calculations (at the

**Table 19**Noble metal 50% condensation temperatures.

Log P (bar)	Re	Ru	Os	Rh	Ir	Pd	Pt	Au
Dry BSE								
-6	755	1003	855	1451	1491	1091	1464	1100
-4	1380	1089	1480	1681	1761	1197	1772	1245
-2	2301	1183	2307	1743	1115	1328	2080	1440
0	3100	1268	3064	1752	1211	1490	2247	1713
2	4188	1312	4236	1754	1333	1701	2271	2114
Wet BSE								
-6	1518	1498	1618	1360	1633	1043	1408	686
-4	1750	1679	1850	1517	1807	1169	1538	734
-2	2146	1957	2152	1712	2039	1331	1673	824
0	2611	2301	2575	1946	2347	1539	1822	940
2	3036	2718	3084	2224	2739	1794	1994	1094

same P and T). For example, the most oxidizing  $fO_2$  in Fig. 1 of Fegley and Palme (1985) is about  $10^{-12.3}$  bar at 1600 K and  $10^{-3}$  bar total pressure versus  $fO_2=10^{-3}$  bar in the dry BSE model at  $10^{-3}$  bar total pressure.

3.3.25.3. Cobalt and nickel. Table 20 and Fig. 14 show equilibrium chemistry of Co and Ni in BSE material. The real solution 50% condensation curves are computed using activity coefficients from FactSage (Table 2). Holzheid et al. (1997) give similar values of CoO ( $\gamma=1.51\pm0.28$ ) and NiO ( $\gamma=2.70\pm0.52$ ) activity coefficients in silicate melts over a range of temperatures (1573–1873 K) and oxygen fugacities (log fO $_2=-3$  to +1.5 relative to the Fe-Fe $_{1.x}$ O buffer). The real and ideal 50% condensation curves agree within  $\leq$ 34 K for both Ni and Co with the real solution curves lying at slightly lower temperature due to the small positive deviations from ideality.

We also find Ni metal condensation in agreement with Lock et al. (2018). This occurs over a P - T range where the  $fO_2$  of BSE material is along the Ni - NiO oxygen fugacity buffer.

3.3.25.4. Rhodium, iridium, palladium, and platinum. The condensation temperatures and volatility sequence for the noble metals are different in BSE material than solar composition material. The dry BSE calculations in Table 19 show Pt is the most refractory noble metal in BSE material except at  $10^{-6}$  bar where Ir condenses 27 K higher. At  $10^{-4}$  bar total pressure, the volatility sequence from most refractory to least refractory in dry and wet BSE material (Table 19), and in solar composition material (Lodders, 2003) is

Dry BSE  $Pt \ge Ir > Rh > Os > Re \gg Au > Pd > Ru$ 

Wet BSE Os > Ir > Re > Ru >  $Pt \ge Rh$  > Pd > Au

Solar  $Re < Os \ll Ir < Ru < Pt < Pd \ll Au$ 

With increasing pressure, the stable Ir condensate in BSE material changes from metal to  $\rm IrO_2$  with a range in which metal plus oxide are stable at fO<sub>2</sub> values on the Ir -  $\rm IrO_2$  oxygen fugacity buffer (O'Neill and Nell, 1997). Depending on total pressure either oxide or monatomic metal gases are the major noble metal gases except gold which is always Au gas in dry BSE material.

3.3.26. Group 11 (Cu, Ag, Au)
Gold was discussed with the Pt-group metals.

3.3.26.1. Copper. Fig. 14c shows the 50% condensation curve for copper computed using Altman's (1978) regular solution model and comparisons to calculations using regular solution fits to the 1573 K point of Holzheid and Lodders (2001), the 1673 K point of Sossi et al. (2019), the 1923 K point of Wood and Wade (2013), and ideal solution. Table 2 lists the activity coefficient equations for the four regular solution models. Fig. 14c and Table 21 show good agreement between the four different activity coefficient models and the ideal solution model. The three major Cu-bearing gases are Cu  $\gg$  CuO > Cu<sub>2</sub> gas in all models. Monatomic copper is the only Cu-bearing gas observed by KEMS studies of Cu<sub>2</sub>O evaporation (Table 1, Sossi and Fegley, 2018).

The calculations do not include CuO dissolution into BSE melt

**Table 20**Co, Ni 50% condensation temperatures – real and ideal solution.

Log P (bar)	Cobalt		Nickel	
	FactSage	Ideal	FactSage	Ideal
-6	1781	1794	1722	1755
-4	2112	2118	2051	2085
-2	2557	2560	2503	2530
0	3225	3239	3166	3181
2	4474	4508	4262	4287

because there are no thermodynamic data for liquid CuO in the JANAF or FactSage databases. The IVTAN data for liquid CuO at one bar are incorrect, as found during this work. Tenorite (CuO) melts incongruently to solid Cu $_2{\rm O}$  + melt at one bar  ${\rm O}_2$  pressure. Reported temperatures of this peritectic point and oxygen content of the melt vary slightly; Roberts and Smyth (1921) measured 1101 °C and  $X_{\rm O}=0.399$  while Kosenko and Emel'chenko (2001) give 1102 °C and  $X_{\rm O}=0.397$ . The congruent melting point of CuO is not known and estimates include 1228 °C and 24.7 bar  ${\rm O}_2$ , 1278 °C and 1268 bar  ${\rm O}_2$ , and 1347 °C and 10 $^4$  bar  ${\rm O}_2$  (Schmid, 1983; Schramm et al., 2005; Kosenko and Emel'chenko, 2001).

3.3.26.2. Silver. Table 22 and Fig. 14d show a comparison of 50% condensation temperatures for Ag<sub>2</sub>O computed with ideal solution and two different activity coefficient models. Monatomic Ag gas is the major gas in all models. Sossi et al. (2019) report  $\gamma(AgO_{0.5}) = 0.67$  at 1673 K for solid silver oxide dissolved in a synthetic ferrobasalt melt. (Silver oxide decomposes prior to melting and there are no experimental data for Ag<sub>2</sub>O liquid.) The regular solution model in Table 2 based on this point agrees well with the ideal solution model but the second model assuming Ag<sub>2</sub>O has the same activity coefficient as Cu<sub>2</sub>O gives temperatures about 140–500 K lower than the other two models over the  $10^{-6}$  - $10^2$  bar range. Prior work on silver solubility in melts in the Ag<sub>2</sub>O – B<sub>2</sub>O<sub>3</sub> - Na<sub>2</sub>O - Al<sub>2</sub>O<sub>3</sub> system (Willis and Hennessy, 1953; Maekawa et al., 1969; Wakasugi et al., 1997) shows negative deviations from ideality for Ag<sub>2</sub>O. The existence of Ag<sub>4</sub>SiO<sub>4</sub> and other silver silicates (Klein and Jansen, 2008) indicates negative deviations from ideality in the Ag<sub>2</sub>O – SiO<sub>2</sub> system. For now, all that can be said is that Ag is more volatile than Cu in BSE material and further measurements of the Ag<sub>2</sub>O activity coefficient are needed.

# 3.3.27. Group 12 (Zn, Cd, Hg)

3.3.27.1. Zinc. Table 23 and Fig. 15a show a comparison of 50% condensation temperatures for ZnO computed with ideal solution and the four different activity coefficient models listed in Table 2. The five models agree within ≤72 K. The FactSage and MAGMA code models agree with one another better than with the other two real solution models. This is plausibly due to using BSE composition for these two models versus a CAS eutectic melt (Reyes and Gaskell, 1983) and a ferrobasalt melt (Sossi et al., 2019). But all models give 50% condensation temperatures within a few percent of each other. Fig. 15a also shows 50% condensation temperatures calculated by Wang et al. (2019) and they agree well with the present work. Monatomic Zn is the major Zn-bearing gas in saturated BSE vapor over the  $10^{-6}$  to  $10^2$  bar range, in agreement with KEMS studies showing ≤0.1% ZnO in the saturated vapor over pure ZnO (Wriedt, 1987a).

3.3.27.2. Cadmium. Table 24 and Fig. 15b compare 50% condensation temperatures for CdO computed with ideal and real solution models. The real solution model has negative deviations from ideality and always lies above the ideal solution model. Sossi et al. (2019) report  $\gamma(CdO) = 0.15$  at 1400 °C for CdO dissolved in a synthetic ferrobasalt melt. Assuming regular solution behavior, their datum yields  $\log \gamma(CdO)$ = -1378.5/T. Two arguments support a negative deviation from ideality for CdO. The larger optical basicity (1.12 for CdO vs 0.92 for ZnO) and smaller ionic potential (2.10 for Cd<sup>2+</sup> vs 2.70 for Zn<sup>2+</sup>) suggest CdO is a stronger base than ZnO with larger negative interaction parameters. Second, the CdF<sub>2</sub> – CaF<sub>2</sub> cigar-shaped phase diagram (O'Horo and White, 1971) would have a different topology if  $\gamma(CdF_2)$  was significantly different than  $\gamma(CaF_2)$  and would look like those for the  $CdF_2 - ZnF_2$  or CdF<sub>2</sub> – PbF<sub>2</sub> systems. Using the fluoride as a proxy for the oxide suggests CdO, like CaO, should display negative deviations from ideality in oxide melts. Monatomic Cd is the major Cd-bearing gas in agreement with vaporization studies done by KEMS and other methods (Wriedt, 1987b).

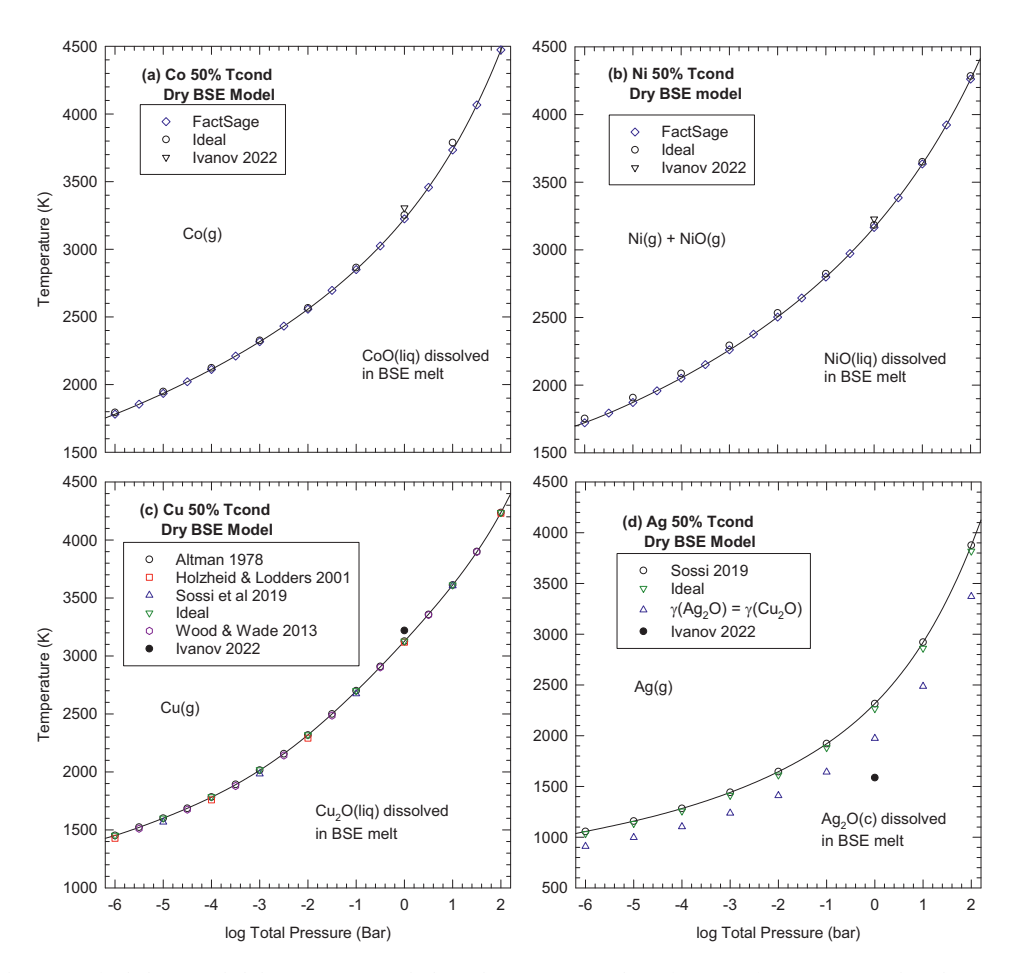


Fig. 14. Equilibrium chemistry of cobalt (a), nickel (b), copper (c), and silver (d) in BSE material as a function of temperature and total pressure. The black curves are the 50% condensation curves. See the text for a detailed discussion of this figure.

**Table 21**Copper 50% condensation temperatures – real and ideal solution.

Log P (bar)	Cu-1	Cu-2	Cu-3	Cu-4	Ideal
-6	1452	1428	1421	1441	1454
-4	1783	1759	1752	1771	1786
-2	2317	2291	2285	2303	2320
0	3127	3119	3117	3122	3128
2	4236	4231	4231	4233	4236

Cu real solution models: (1) Altman (1978). (2) Holzheid and Lodders (2001). (3) Sossi et al. (2019). (4) Wood and Wade (2013). See text for details.

**Table 22** Silver 50% condensation temperatures – real and ideal solution.

Log P (bar)	Ideal	Ag-1	Ag-2
-6	1035	1056	910
-4	1257	1283	1104
-2	1612	1645	1410
0	2266	2315	1974
2	3819	3876	3372

Real solution models: (1) log  $\gamma=-582.0/T$  Sossi et al. (2019) 1673 K point. (2) log  $\gamma=\log\gamma(Cu_2O)=3582.8/T$ , Sossi et al. (2019) Cu $_2O$  1673 K point. See text for details.

3.3.27.3. Mercury. Mercury stays in the gas as Hg (g) and does not condense into BSE melt. Condensation temperatures were computed using extrapolations of  $\log_{10}$  a(HgO) vs. 1/T from the higher temperature CONDOR code results. Mercury (II) oxide condenses at higher temperature than Hg and the temperatures for initial condensation of

**Table 23**Zinc 50% condensation temperatures - real and ideal solution.

Log P (bar)	Zn-1	Zn-2	Zn-3	Zn-4	ideal
-6	1453	1451	1467	1463	1450
-4	1785	1787	1793	1787	1787
-2	2319	2330	2309	2288	2330
0	3129	3137	3103	3065	3132
2	4242	4259	4223	4213	4256

Models:(1) FactSage. (2) MAGMA. (3) Reyes and Gaskell (1983). (4) Sossi et al. (2019).

HgO (a <sub>HgO</sub>	= 1) are:				
log P <sub>T</sub>	-6	-4	-2	0	2
T/K	339	393	468	579	758

Mercury is the most volatile element in BSE material and in solar composition material.

#### 3.3.28. Group 13 (B, Al, Ga, In, Tl)

Aluminum was discussed earlier; see the results in Table 7 and Figs. 4b and 6. Group 13 elements, except for thallium, are more stable as sesquioxides  $M_2O_3$  than suboxides  $M_2O$ , and are acidic or amphoteric in oxide melts. Boric oxide  $B_2O_3$  is a strong acid and lead borate (2PbO· $B_2O_3$ ) is a solvent used for high-temperature molten oxide calorimetry (Navrotsky, 1977). Optical basicity  $\Lambda$  increases, acidity decreases, and cation ionic potential Z/r decreases down group 13; the

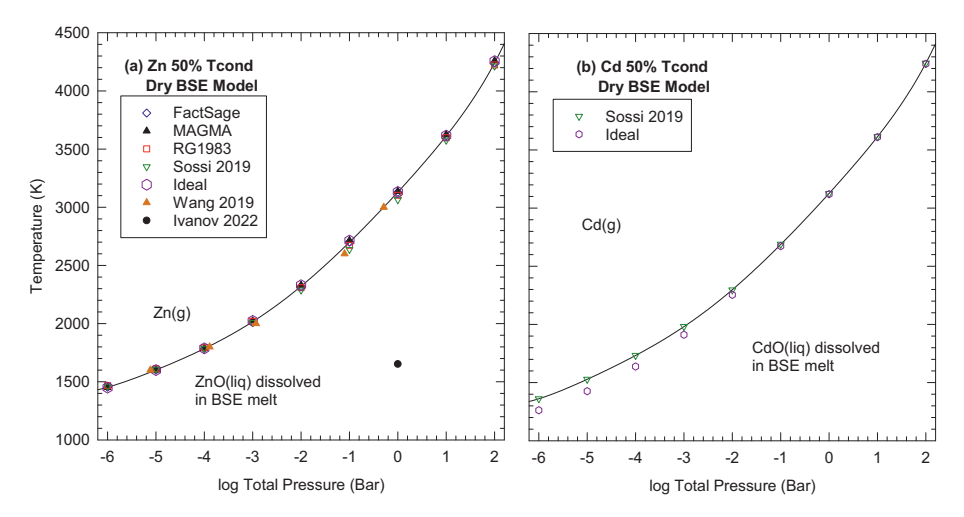


Fig. 15. Equilibrium chemistry of zinc (a) and cadmium (b) in BSE material as a function of temperature and total pressure. The black curves are the 50% condensation curves

**Table 24** Cd 50% condensation temperatures - real and ideal solution.

Log P (bar)	Real	Ideal
-6	1361	1262
-4	1733	1638
-2	2296	2254
0	3125	3120
2	4246	4240

val	lues	are

	$B_2O_3$	Al <sub>2</sub> O <sub>3</sub>	Ga <sub>2</sub> O <sub>3</sub>	$In_2O_3$
Λ	0.42	0.60	0.71	1.25
Z/r	11.1	5.56	4.84	3.70

(Duffy, 2004, 2005; Shannon, 1976). This trend suggests larger negative interaction parameters and larger negative deviations from ideality down the group, which is seen from the activity coefficients of 0.28–0.37 (1573–1773 K) for AlO $_{1.5}$  and 0.02 (1923 K) for InO $_{1.5}$  in CMAS melts (Table 2, Sossi and Fegley, 2018). However, the activity coefficients of Group 13 oxides in silicate melts are poorly known and need more study.

3.3.28.1. Boron. Table 25 and Fig. 16a show 50% condensation temperatures for boron as  $B_2O_3$  for real and ideal solution models. The black line in Fig. 16a is computed with the FactSage activity coefficient in Table 2; the ideal solution condensation temperatures are much lower as seen in Fig. 16a and Table 25. Boron gas chemistry is complex. The

Table 25
Group 13 (B, Al, Ga, In, Tl) 50% condensation temperatures.

Log P (bar)	В	Al	Ga	In	Tl
Ideal solution					
-6	1113	2134	1615	1446	924
-4	1355	2460	1891	1757	1137
-2	1756	2952	2350	2205	1490
0	2574	3632	3127	2890	2209
2	4193	4825	4228	4057	4064
Real solution					
-6	1447	2159	1739	1473	1405
-4	1784	2498	2033	1789	1729
-2	2336	2960	2452	2299	2252
0	3147	3645	3143	3070	3106
2	4281	4894	4238	4206	4223

major gases are alkali metaborates (MBO $_2$  with M = Na, K, Rb, Cs) > BO $_2$  > BO > B $_2$ O $_3$   $\gg$  B over the  $10^{-6}$  to  $10^2$  bar range. Lithium metaborate is not an important gas because lithium is fully condensed in the BSE melt at temperatures where boron is 50% condensed.

3.3.28.2. Gallium. Table 25 and Fig. 16b show 50% condensation temperatures for  $Ga_2O_3$  for real and ideal solution in BSE melt. The existence of gallium analogs of albite (NaGaSiO\_3) and anorthite (CaAl-GaSi\_2O\_8) and metal – silicate partitioning experiments indicate  $Ga_2O_3$  displays negative deviations from ideality in silicate melts (Goldsmith, 1950; Capobianco et al., 1999) despite positive deviations from ideality in the  $Ga_2O_3$  -  $SiO_2$  binary (Glasser, 1959). The logarithm of the  $Ga_2O_3$  activity coefficient log  $\gamma(Ga_2O_3)$  is interpolated from the logarithms of activity coefficient values for  $Al_2O_3$  and  $In_2O_3$  as a function of optical basicity (Table 2). The major Ga-bearing gases in saturated BSE vapor are  $Ga > GaO > Ga_2O$  over the  $10^{-6}$  to  $10^2$  bar range, while  $Ga_2O$  is the major Ga-bearing gas in the saturated vapor over pure  $Ga_2O_3$  (Table 1, Sossi and Fegley, 2018). The different speciation arises for the same reasons discussed above for lithium.

3.3.28.3. Indium. Table 25 and Fig. 16c show 50% condensation temperatures for ideal and real solution of indium in BSE melt. CONDOR calculations used two real solution models; one is a regular solution fit to the 1923 K point of Wood and Wade (2013) and the other one sets the In<sub>2</sub>O<sub>3</sub> activity coefficient equal to the FactSage value for Al<sub>2</sub>O<sub>3</sub> (see Table 2). The differences between the 50% condensation temperatures from the two real solution models are 13–62 K while the ideal solution temperatures are 150–640 K lower than the real solution values. The major In-bearing gases in saturated BSE vapor are In > InO > In<sub>2</sub>O over the  $10^{-6}$  to  $10^{2}$  bar range. Several KEMS studies show In<sub>2</sub>O is the major In-bearing gas in the saturated vapor over pure In<sub>2</sub>O<sub>3</sub> (Table 1, Sossi and Fegley, 2018). The different indium gas speciation arises for the same reasons discussed above for lithium.

3.3.28.4. Thallium. Thallous oxide  $Tl_2O$  is the major thallium – bearing oxide in the melt. This is consistent with thallium chemistry in two other ionic solvents – water and molten salts. Monovalent Tl chemistry is qualitatively different than that of the other Group 13 elements, which are trivalent, and its chemistry has similarities to alkali element chemistry (e.g., chapter 9 of Cotton and Wilkinson (1972). For example, boric oxide is a network former while  $Tl_2O$  is a network modifier like  $K_2O$  or  $Ag_2O$ . Aluminum, gallium, and indium oxides are all amphoteric and can serve as network formers or modifiers (Reddy et al., 2001). The molten salt chemistry of thallous halides is like that of alkali halides and

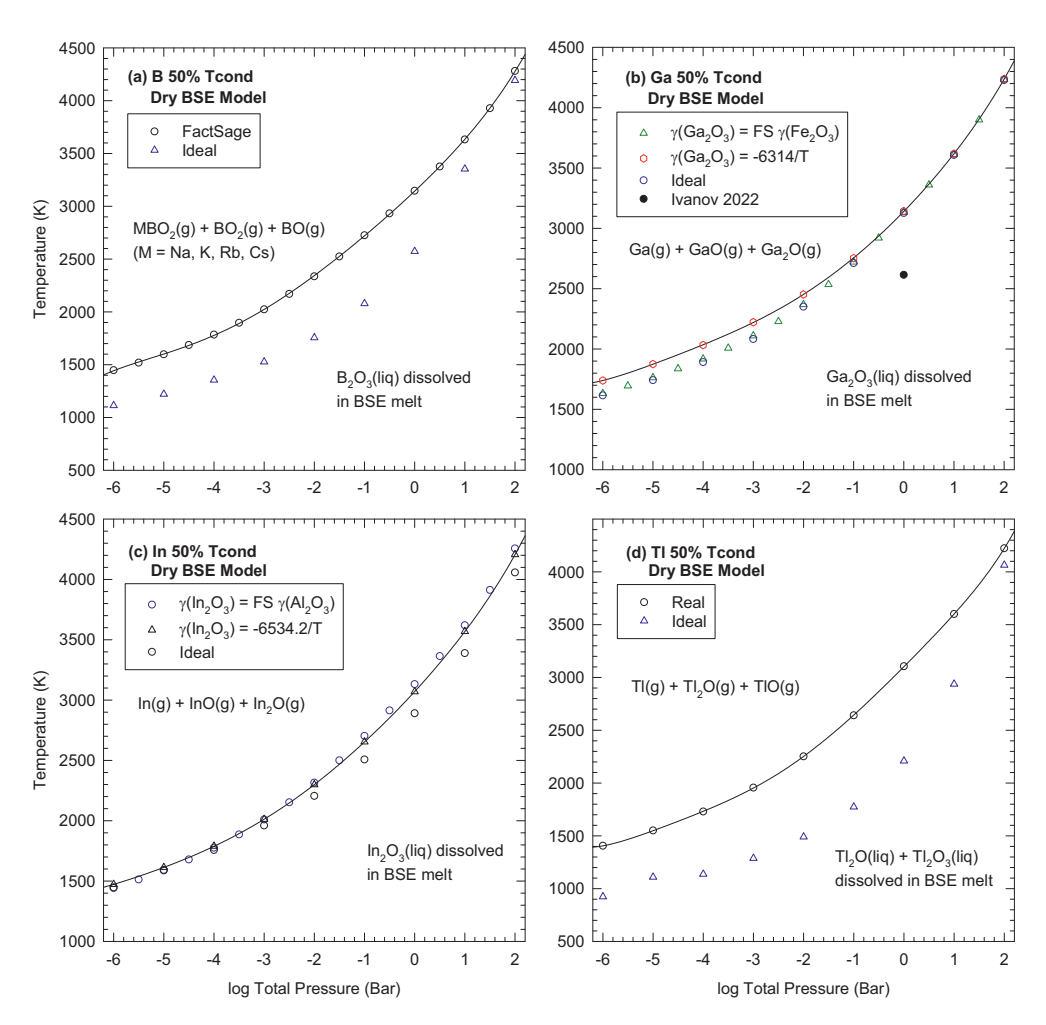


Fig. 16. Equilibrium chemistry of boron (a), gallium (b), indium (c), and thallium (d) in BSE material as a function of temperature and total pressure. The black curves are the 50% condensation curves. Fig. 4b shows the same for aluminum.

silver halides (Lumsden, 1966). The ionic potential of six-coordinate  $TI^{+1}$  is 0.67 and is closer to that of  $Rb^{+1}$  (0.66) than to  $K^{+1}$  (0.72) or  $Ag^{+1}$  (0.87). Thus, the estimate  $\gamma(Tl_2O) = \gamma(Rb_2O)$  was used in the condensation calculations. The ionic potential of  $TI^{3+}$  is closer to  $Fe^{3+}$  than  $AI^{3+}$  and  $\gamma(Tl_2O_3) = \gamma(Fe_2O_3)$  was used in the calculations.

Table 25 and Fig. 16d show the results for thallium. The ideal solution 50% condensation temperatures in Table 25 show Tl is the most volatile Group 13 element in BSE material over the  $10^{-6}$  to  $10^2$  bar range. The sequence from most volatile (lowest 50%  $T_{cond}$ ) to most refractory (highest 50%  $T_{cond}$ ) is Tl < B < In < Ga < Al. Table 25 shows effects of non-ideal solution on volatility; Tl is the most or 2nd most volatile element but the subsequent volatility sequence changes from Tl < B  $\simeq$  In < Ga < Al at  $10^{-6}$  bar to In < Tl  $\simeq$  Ga < B  $\simeq$  Al at  $10^2$  bar.

The major Tl-bearing gases in saturated BSE vapor are Tl > TlO > Tl<sub>2</sub>O over the  $10^{-6}$  to  $10^2$  bar range. Knudsen effusion, KEMS, and transpiration studies show Tl<sub>2</sub>O is the major Tl-bearing gas in the saturated vapor over pure Tl<sub>2</sub>O, Tl<sub>4</sub>O<sub>3</sub>, and Tl<sub>2</sub>O<sub>3</sub> (Table 1, Sossi and Fegley, 2018). The different thallium gas speciation in saturated vapor above BSE melt and thallium oxides arises for the same reasons discussed above for lithium.

# 3.3.29. Group 14 (C, Si, Ge, Sn, Pb)

All group 14 elements except carbon, which is not discussed further, are in the dry BSE model. The results for silicon dissolution as  $SiO_2$  in the BSE melt and Si gas chemistry in saturated BSE vapor are in Table 6 and Figs. 4d and 7.

Silicon, Ge, Sn, and Pb all form stable dioxide solids and Pb also

forms a stable monoxide solid. Brewer and Greene (1957) showed SiO solid is unstable at all temperatures. Brewer and Zavitsanos (1957) studied the  $Ge-GeO_2$  phase diagram by differential thermal analysis and concluded "it is of the simple eutectic type with a miscibility gap for the liquids". They found no evidence for the existence of GeO solid. The KEMS study of Drowart et al. (1965b) shows GeO solid is metastable and disproportionates to solid  $GeO_2+Ge$ . Platteeuw and Meyer (1956) showed GeO solid is unstable and decomposes into GeO at and above GeO solid is unstable and decomposes into GeO at and above GeO solid is stable at high temperature (Drowart et al., 1965a).

Knudsen effusion mass spectrometry studies show the stable dioxides of Si, Ge, and Sn evaporate incongruently to a mixture of monoxide, dioxide, and monatomic gas with a bulk oxygen/metal ratio of two in the saturated vapor over the pure solid or liquid oxide (Table 1, Sossi and Fegley, 2018). Thermogravimetric and KEMS studies show PbO2 decomposes upon heating to lower lead oxides PbOx (x < 2) plus O2 (gas), ultimately forming PbO, which evaporates incongruently to a mixture of PbO, Pb, and (PbO)2–6 gases with a bulk Pb/O ratio of unity (Drowart et al., 1965a, 1965b, Otto, 1966).

The calculations show monoxides are the major gases for Si, Ge, and Sn in saturated BSE vapor and that the dioxide and monatomic gases are less abundant along the 50% condensation curves. The major Ge-bearing gases are GeO > GeO $_2$  > Ge > Ge $_2O_2$  over the  $10^{-6}$  to  $10^2$  bar total pressure range. The major Sn-bearing gases are SnO > Sn > SnO $_2$  over the same total pressure range. Lead chemistry is different. The major Pb-bearing gases in saturated BSE vapor are Pb  $\gtrsim$  PbO  $\gg$  PbO $_2$  over the  $10^{-6}$  to  $10^2$  bar total pressure range, with Pb a few times more abundant than

PbO, which is never the major gas. Table 26 summarizes gas chemistry at  $10^{-4}$  bar total pressure for Si, Ge, Sn, and Pb at the temperatures where each element is 50% condensed. The gaseous M/MO, M/MO<sub>2</sub>, and MO/MO<sub>2</sub> molar ratios increase downward in Group 14 from Si to Ge to Sn to Pb. The monatomic and monoxide gases become more important and the dioxide gases less important going down Group 14. Except for PbO (liquid), where PbO polymer gases are important (Drowart et al., 1965a, 1965b), the major gases in saturated BSE vapor are the same as those in saturated vapor over the pure Group 14 oxides.

3.3.29.1. Germanium. Table 27 and Fig. 17a show the results for Ge chemistry in BSE material. Literature reports indicate germanium dissolves in CMAS, CMS-FeO, and CAS-FeO silicate melts as GeO2 and/or GeO (Kegler and Holzheid, 2011; Mare et al., 2020; Yan and Swinbourne, 2003; Shuva et al., 2016). There are no thermodynamic data for formation of GeO (solid, liquid) from its constituent elements in any of the standard data compilations, so only  $Ge^{4+}$  (GeO<sub>2</sub>) was considered. FactSage calculations give  $\gamma(GeO_2) = 7.4$  independent of temperature for the six-component BSE melt, but Sossi et al. (2019) found negative deviations from ideality in a ferrobasalt melt (see Table 2). Magnesia and  $SiO_2$  are the two major oxides in BSE melt (Table 1) and the  $GeO_2$  – MgO phase diagram (Robbins and Levin, 1959) and activity measurements in GeO<sub>2</sub> - SiO<sub>2</sub> melts (Yoshikawa et al., 2004) show negative deviations from ideality at low GeO2 concentrations. Unless there are large positive interaction parameters of GeO2 with the less abundant oxides (FeO, CaO, Al<sub>2</sub>O<sub>3</sub>, Na<sub>2</sub>O, etc.) in BSE melt negative deviations from ideality are expected for GeO2 dissolved in BSE melt. Table 27 shows the maximum  $\Delta T$  between the five models ranges from 41 K at  $10^{-6}$  bar total pressure to 155 K at 100 bar total pressure. This is about a 3.3% difference across the entire pressure range.

3.3.29.2. Tin. Table 28 and Fig. 17b show the results for tin chemistry in BSE material. The 50% condensation temperatures are for dissolution of liquid SnO + SnO $_2$  in BSE melt. (Gurvich et al., 1989) give thermodynamic data for solid and liquid SnO and SnO $_2$  in the IVTAN database and a discussion of their thermodynamic data assessment and choices. The real solution model uses FactSage values for  $\gamma(\text{SnO})$  and sets  $\gamma(\text{SnO}_2) = \gamma(\text{GeO}_2)$  from FactSage. Fig. 17b shows good agreement between the present work and results from Wang et al. (2019). Carbo-Nover and Richardson (1972) reported ideal solution for SnO in SnO - SiO $_2$  melts (with <1% SnO $_2$ ) at 1273–1523 K. However, Kozuka et al. (1968) and Grau and Flengas (1976) found  $\gamma(\text{SnO}) > 1$  in the same system.

3.3.29.3. Lead. Table 28 and Fig. 17c show the results for lead chemistry in BSE material. Table 2 lists the activity coefficients for the four real solution models used. Two of these are from Sossi et al. (2019) who assumed either PbO (liquid) vaporization to PbO (gas)

or the dissociative congruent vaporization of PbO (liquid) via

PbO (liquid) = Pb (gas) + 1/2 O<sub>2</sub> (gas)

Table 26 Group 14 (Si, Ge, Sn, Pb) gas chemistry at  $10^{-4}$  bar for the dry BSE model.

Z	Element	$T_{50}/K^a$	Major gas	M/MO	$M/MO_2$	$MO/MO_2$
14	Si	2159	SiO	$2.3\times10^{-8}$	$3.2\times10^{-7}$	$1.4 \times 10^{1}$
32	Ge	1781	GeO	$2.3\times10^{-7}$	$7.2  imes 10^{-3}$	$3.1 \times 10^{4}$
50	Sn	1791	SnO	$4.3 \times 10^{-4}$	$5.2 \times 10^2$	$1.2 \times 10^6$
82	Pb	1782	Pb	4	$7.1 \times 10^8$	$1.7\times10^8$

 $<sup>^{\</sup>rm a}$  Nominal values. The  $\rm T_{50}$  ranges from different activity coefficient models are 2159–2221 K for Si, 1725–1783 K for Ge, and 1782–1789 K for Pb. See text for details.

**Table 27**Ge 50% condensation temperatures - real and ideal solution.

Log P (bar)	Ge-1	Ge-2	Ge-3	Ge-4	Ideal
-6	1464	1423	1449	1456	1445
-4	1781	1725	1775	1783	1768
-2	2269	2195	2296	2260	2283
0	2960	2992	3113	3118	3107
2	4072	4212	4224	4227	4222

Ge real solution models: (1) Sossi et al. (2019). (2) FactSage. (3)  $\gamma$ (GeO<sub>2</sub>) =  $\gamma$ (SiO<sub>2</sub>). (4) Regular solution fit to 1673 K point of Sossi et al. (2019).

depending upon the oxygen fugacity in their experiments. Our regular solution fits to their derived activity coefficients at 1673 K are in Table 2. The other real solution models are from FactSage and Wood and Wade (2013).

The condensation temperatures from the four real solution models agree within 8 K over the  $10^{-6}$  to  $10^2$  bar range. The ideal solution condensation temperatures are lower by 10–15 K over the same total pressure range. This difference occurs because the real solution models predict PbO has negative deviations from ideality in the BSE melt. Table 28 shows similar condensation temperatures for PbO and SnO + SnO<sub>2</sub> dissolved in the BSE melt. Lead is more volatile than tin at lower total pressure but the two are equally volatile at higher total pressure.

# 3.3.30. Group 15 (N, P, As, Sb, Bi)

All group 15 elements except nitrogen are in the dry BSE model. Optical basicities of group 15 oxides vary from strongly acidic to basic down the group: 0.27 ( $N_2O_5$ ), 0.33 ( $P_2O_5$ ), 1.02 ( $As_2O_3$ ), 1.14 ( $Sb_2O_3$ ), and 1.19 ( $Bi_2O_3$ ). The optical basicities suggest less strongly negative deviations from ideality down Group 15 and similar activity coefficients for Sb and Bi oxides.

3.3.30.1. Phosphorus. Table 29 and Fig. 18a give the results for three different real solution models of  $P_2O_5$  condensation in BSE melt and show the result from Ivanov et al. (2022) for comparison. Table 2 gives the activity coefficient equation for the Ban-Ya (1993) model. The equation for  $\gamma(P_2O_5)$  from Suito et al. (1981) is

$$log_{10}\gamma_{P_2O_5}(Suito) = -1.01(23X_{CaO} + 17X_{MgO} + 8X_{FeO}) - \frac{26,270}{T} + 11.24$$

Using the BSE melt composition in Table 1 gives the equation listed in Table 2. The differences between calculated 50% condensation temperatures are about 200 K at  $10^{-6}$  bar and  $10^2$  bar but smaller at the intermediate pressures. No ideal solution calculations were done for  $P_2O_5$  condensation it displays large negative deviations from ideality in silicate melts.

Phosphorus oxide gas chemistry is complex. Knudsen effusion mass spectrometry shows  $P_4O_{10}$  is the major gas and  $P_4O_9$  the minor gas in the saturated vapor over commercial "phosphorus pentoxide" at  $\leq 150~^\circ C$  (Muenow et al., 1970). [Commercial "phosphorus pentoxide" is the metastable hexagonal polymorph, which is composed of  $P_4O_{10}$  molecules (Jung and Hudon, 2012)]. Muenow et al. (1970) found increasing amounts of other phosphorus oxide gases in the saturated vapor with increasing temperature, e.g.,  $P_4O_{6-10}$ ,  $P_3O_{4-7}$ ,  $P_2O_{2-5}$ , and  $PO_{1-3}$ . Kazenas and Petrov (1997) confirmed their results. In contrast, the two major P-bearing gases in saturated BSE vapor are  $PO_2 \gtrsim PO$  with less abundant gases being  $P_2O_{3-5} \gtrsim P > P_4O_6$ . Markova et al. (1986) state that PO and  $PO_2$  are the phosphorus gases in the saturated vapor over molten lunar basalts. The different phosphorus gas speciation in saturated vapor above BSE melt and "phosphorus pentoxide" arises for the same reasons discussed above for lithium.

3.3.30.2. Arsenic. Tables 29 and 30 and Fig. 18b give the results for  $As_2O_3$  condensation in BSE melt. Arsenic condensation was computed as  $As_2O_3$  ( $AsO_{1.5}$ ) dissolution in molten silicate and used activity

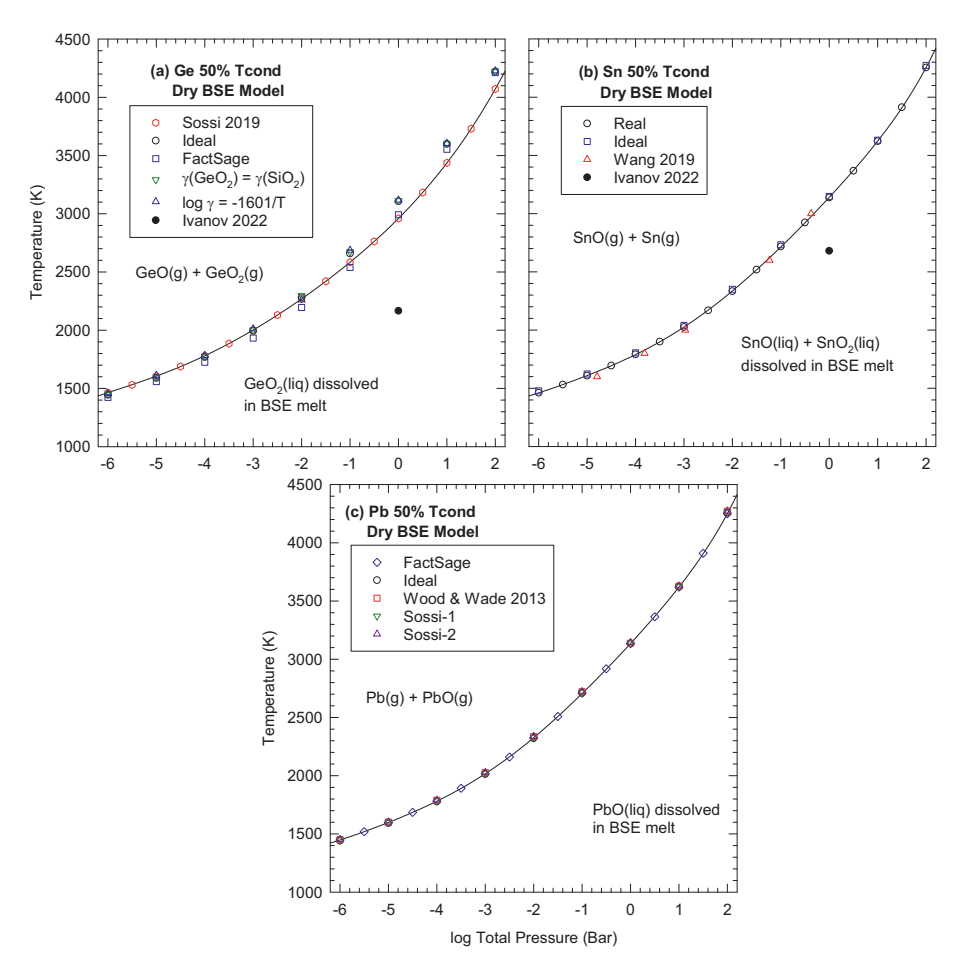


Fig. 17. Equilibrium chemistry of germanium (a), tin (b), and lead (c) in BSE material as a function of temperature and total pressure. The black curves are the 50% condensation curves. Silicon equilibrium chemistry is in Fig. 4d.

Table 28
Sn and Pb 50% condensation temperatures - real and ideal solution.

Log P (bar)	Sn-1	Sn-2	Pb-1	Pb-2	Pb-3	Pb-4	Pb-5
-6	1461	1478	1448	1452	1448	1452	1442
-4	1791	1805	1782	1789	1784	1789	1778
-2	2333	2350	2324	2336	2329	2337	2322
0	3138	3148	3134	3138	3140	3144	3136
2	4254	4273	4250	4272	4265	4273	4258

Sn-1: real. Sn-2: ideal. Pb-1: FactSage. Pb-2: Wood and Wade (2013) log  $\gamma=-1265/T$ . Pb-3: Sossi et al. (2019) log  $\gamma=-689/T$ . Pb-4: Sossi et al. (2019) log  $\gamma=-1320/T$ . Pb-5: ideal.

Table 29
Group 15 (P, As, Sb, Bi) 50% condensation temperatures - real solution.

Log P (bar)	P <sub>2</sub> O <sub>5</sub> -1	P <sub>2</sub> O <sub>5</sub> -2	P <sub>2</sub> O <sub>5</sub> -3	$As_2O_3$	$\mathrm{Sb_2O_3}$	$Bi_2O_3$
-6	1583	1737	1761	1544	1552	1461
-4	1948	1996	2028	1804	1804	1781
-2	2474	2376	2400	2302	2293	2291
0	3176	3082	3103	2958	2870	3072
2	4322	4084	4126	3831	3619	4211

Real solution models for  $P_2O_5$ :(1) Ban-Ya (1993). (2) FactSage. (3) Suito et al. (1981).

coefficients from FactSage and regular solution fits to the low ( $\gamma=0.03$ ) and high ( $\gamma=0.56$ ) values at 1573 K for AsO<sub>1.5</sub> dissolved in FeO<sub>x</sub> - CaO - SiO<sub>2</sub> copper smelting slags (Chen and Jahanshahi, 2010). The equations for the three different real solution models for As<sub>2</sub>O<sub>3</sub> activity coefficients

are in Table 2.

Fig. 18b shows the two curves based on Chen and Jahanshahi (2010) lie at much lower temperature than the FactSage curve. This difference could be due to the difference between activity coefficients in BSE melt and the copper smelting slags. The FactSage condensation curve was used in this work. The choice (of As<sup>3+</sup>) is consistent with literature studies, which conclude trivalent As dissolves in molten silicates (Canali et al., 2017; Chen and Jahanshahi, 2010; Hidayat et al., 2021;d Maciag and Brenan, 2020; Shuva et al., 2016).

Arsenic gas chemistry is complex and Knudsen effusion mass spectrometry (Brittain et al., 1982; Kazenas and Petrov, 1997) shows  $As_4O_6$  is the major gas in the saturated vapor over pure arsenolite (octahedral  $As_2O_3$ ). In contrast, the major As-bearing gases in saturated BSE vapor are AsO>As with  $As_2>As_4>As_4O_6$  much less abundant. The different arsenic gas speciation in saturated vapor above BSE melt and octahedral  $As_2O_3$  arises for the same reasons discussed above for lithium.

3.3.30.3. Antimony. Tables 29 and 30 and Fig. 18c show 50% condensation temperatures for  $Sb_2O_3$  dissolution in BSE melt. Maciag and Brenan (2020) conclude antimony is  $Sb^{3+}$  in basaltic melts. Activity coefficient data in Shuva et al. (2016) show negative deviations from ideality increase from  $Bi_2O_3$  to  $Sb_2O_3$  to  $As_2O_3$  at constant T,  $fO_2$ , and melt composition in  $FeO_x$  - CaO -  $SiO_2$  copper smelting slags. Whether this trend applies to mafic and ultramafic melts is unknown. The existence of stable Mg and Ca antimonides such as MgSb2O4 and CaSb2O4 shows negative deviations from ideality in the MgO –  $Sb_2O_3$  and CaO –  $Sb_2O_3$  systems (Katayama et al., 1987, 1998). Negative deviations from ideality are assumed for  $Sb_2O_3$  dissolution in BSE melt and  $\gamma(Sb_2O_3)$  =

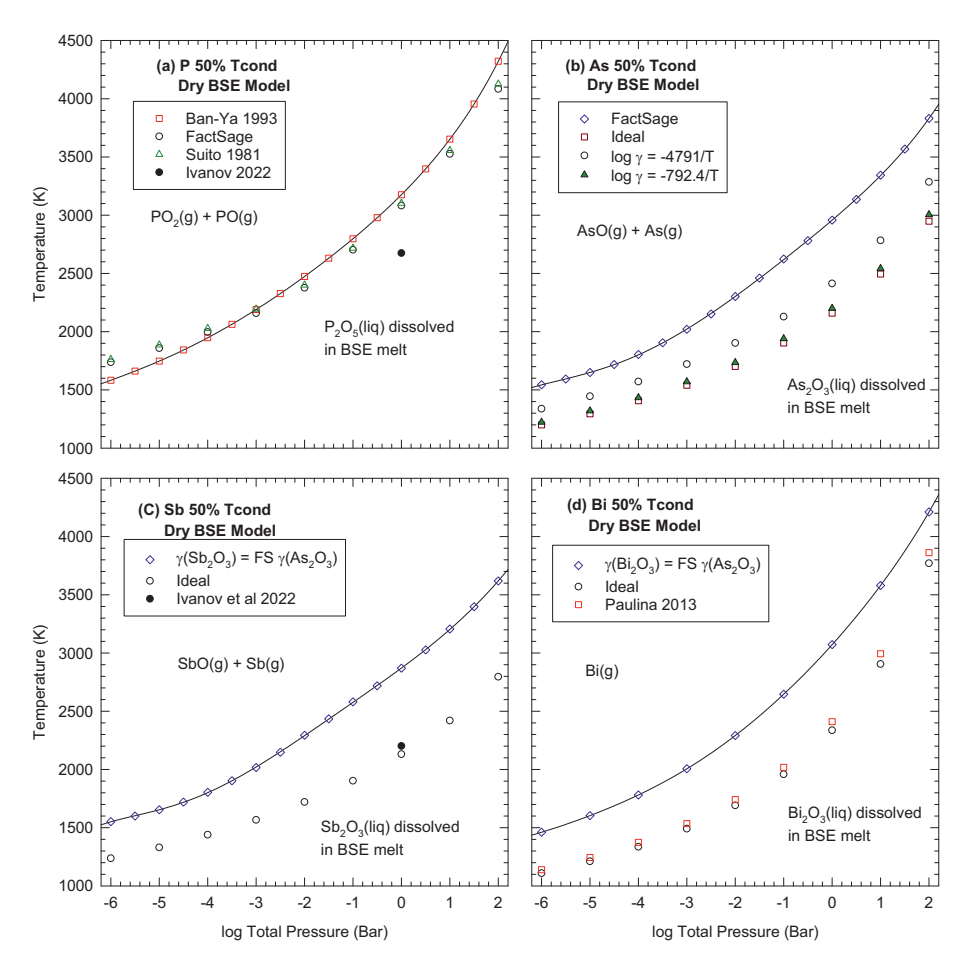


Fig. 18. Equilibrium chemistry of phosphorus (a), arsenic (b), antimony (c), and bismuth (d) in BSE material as a function of temperature and total pressure. The black curves are the 50% condensation curves.

**Table 30**As, Sb, Bi 50% condensation temperatures - ideal solution.

Log P (bar)	$As_2O_3$	$\mathrm{Sb_2O_3}$	$Bi_2O_3$
-6	1200	1237	1109
-4	1407	1439	1336
-2	1702	1720	1691
0	2159	2131	2336
2	2949	2796	3770

 $\gamma(As_2O_3)$  is estimated in the absence of other data.

Knudsen effusion (Behrens and Rosenblatt, 1973) and KEMS (Semenov et al., 1983) show  $\mathrm{Sb_4O_6}$  is the major gas in the saturated vapor over subliming orthorhombic  $\mathrm{Sb_2O_3}$  (valentinite). In contrast, the major Sb-bearing gases in saturated BSE vapor are SbO > Sb followed by  $\mathrm{Sb_2} > \mathrm{Sb_4O_6} > \mathrm{Sb_4}$  along the Sb 50% condensation curve. The different antimony gas speciation in saturated vapor above BSE melt and octahedral  $\mathrm{Sb_2O_3}$  arises for the same reasons discussed above for lithium.

3.3.30.4. Bismuth. Tables 29 and 30 and Fig. 18d show  $Bi_2O_3$  condensation in BSE melt. Three sets of calculations were done: (1) ideal solution, (2) estimating  $\gamma(Bi_2O_3) = \gamma(As_2O_3)$  from FactSage, and (3) a regular solution fit to  $\gamma(BiO_{1.5}) = 0.4$  at 1573 K in FeO<sub>x</sub> - CaO - SiO<sub>2</sub> copper smelting slags (Paulina et al., 2013), which is given in Table 2.

Fig. 18d shows the large differences between 50% condensation temperatures between the three sets of calculations. There are no intermediate compounds in the MgO –  $Bi_2O_3$  system, but the binary systems of  $Bi_2O_3$  with  $Al_2O_3$ ,  $Na_2O$ , and  $TiO_2$  contain intermediate compounds (Kargin et al., 2008; Jiang et al., 2021). Consequently, the

activity coefficient equation based on Bi $_2$ O $_3$  dissolution in FeO $_x$  - CaO - SiO $_2$  copper smelting slags (Paulina et al., 2013), may underestimate the negative deviations from ideality for Bi $_2$ O $_3$  dissolved in BSE melt. Based on Shuva et al. (2016) cited above, the "true" Bi $_2$ O $_3$  activity coefficient and 50% condensation temperature should lie between the two sets of curves in Fig. 18d.

The major Bi-bearing gases in saturated BSE vapor are Bi  $\gg$  BiO, which are also the major gases in saturated vapor over Bi<sub>2</sub>O<sub>3</sub> (Table 1, Sossi and Fegley, 2018).

# 3.3.31. Groups 16–18 (Chalcogens, halogens, noble gases)

Oxygen is the only Group 16–18 element in the dry BSE model. Table 31 gives 50% condensation temperatures for oxygen computed using the nominal activity coefficients for oxides in the BSE melt and a comparison to the 50% oxygen condensation temperature from Ivanov et al. (2022) at one bar total pressure. Sulfur, selenium, and tellurium are in the wet BSE model and their condensation chemistry is complicated. For example, the dissolved form of sulfur depends upon oxygen

**Table 31**Oxygen 50% condensation temperatures - real and ideal solution.

Log P (bar)	Real	Ideal
-6	1858	1819
-4	2173	2134
-2	2617	2581
O <sup>a</sup>	3294	3260
2	4463	4427

<sup>&</sup>lt;sup>a</sup> Ivanov et al. (2022) give 3409 K for 50% condensation of oxygen at one bar total pressure.

fugacity with sulfide favored at lower  $fO_2$  and sulfate favored at higher  $fO_2$  (Fig. 12 and associated discussion in Zolotov and Fegley, 1999). Ivanov et al. (2022) list 2983 K for the 50% condensation temperature of sulfur in BSE melt at one bar total pressure but do not provide details necessary to evaluate their result. The dissolution of selenium and tellurium is also  $fO_2$  dependent with reduced selenium and tellurium species favored at lower  $fO_2$  and oxidized selenium and tellurium species favored at higher oxygen fugacity. However, the solubilities and activity coefficients of chalcogens in BSE melt are not known and must be estimated using Temkin mixing or another method. The solubilities of halogens in BSE melt are not known and need to be estimated from existing solubility data in basaltic melt at lower temperatures. This work is beyond the scope of this paper.

#### 3.3.32. Actinides (Th. U. Pu)

Table 15 and Fig. 13b give 50% condensation temperatures for ideal solution of ThO2, UO2, and PuO2 in BSE melt. Uranium is most volatile, and thorium is the most refractory. The major uranium-bearing gases are UO3 > UO > > U with UO2 (g) becoming more important with increasing pressure. The major thorium-bearing gases are ThO2 > ThO > Th with ThO2 always dominant. Plutonium gas chemistry is unique. The major Pu-bearing gases are PuO2 > PuO > Pu > Pu $^+$  from  $10^{-6}$  to  $10^2$  bar total pressure.

# 3.3.33. Thermal ionization

Thermal ionization is included in the chemical equilibrium calculations as discussed earlier. Fig. 19 shows logarithmic contours of the electron partial pressure over 1500–4500 K and  $10^{-6}$  to  $10^2$  bar total pressure. Thermal ionization increases electrical conductivity and magnetic fields in the proto-lunar disk, which drive turbulence and bipolar outflows that remove mass from the Earth – Moon system (Gammie et al., 2016). Cesium has the lowest ionization potential (3.89 eV) of any naturally occurring element, but calcium is significantly more abundant with a low ionization potential of 6.11 eV making Ca $^+$  the major cation and major electron source in a proto-lunar disk composed of silicate vapor and melt.

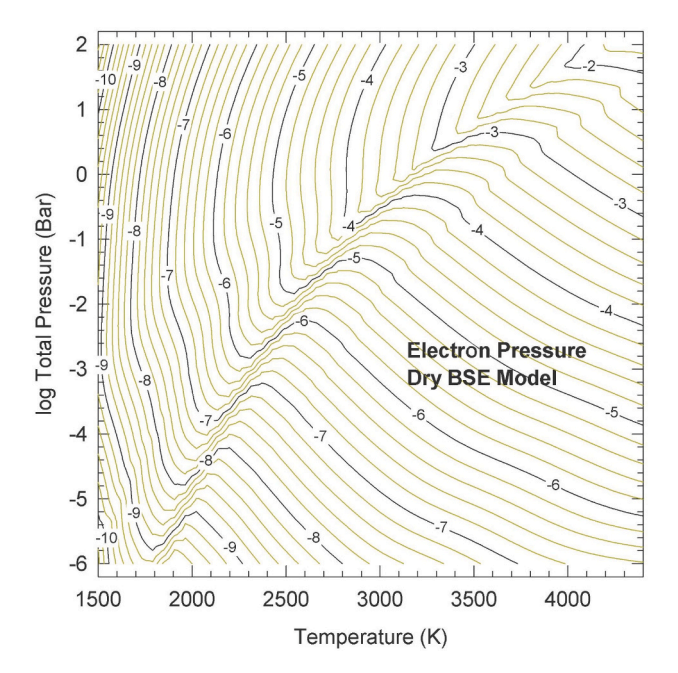


**Fig. 19.** Logarithmic contours of the electron partial pressure in equilibrium with BSE material as a function of temperature and total pressure. The kinks in the contours are due to size of the P and T steps in the grid.

#### 4. Discussion

# 4.1. Comparison of condensation temperatures in silicate and solar composition material

Calculated 50% condensation temperatures for the  $10^{-6}$  to  $10^2$  bar total pressure range are in the preceding tables and figs. A summary at  $10^{-4}$  bar total pressure is in Table 32. Comparison of Table 32 with Table 8 of Lodders (2003) shows condensation temperatures in BSE material are significantly higher than those in solar composition material. Even mercury condenses about 140 K higher in silicate than in solar composition material. Two factors are responsible for the large differences.

The first factor is the absence in dry BSE material of hydrogen and helium, which dilute the partial pressures of rocky element gases in solar composition material. In other words, the metallicity of silicate vapor is significantly higher than that of solar composition material. The hydrogen and helium abundances in wet BSE material are orders of magnitude lower than in solar composition material and the same argument holds.

The second factor is the significantly higher oxygen fugacity of silicate material. This follows from Goldschmidt's (1928) observation that oxygen is the most abundant element in silicates (on an atomic basis). Fig. 1 of Fegley et al. (2020) shows the large difference between the  $fO_2$  of silica vapor, BSE vapor, and solar composition gas as a function of temperature. The reader can make a similar quantitative comparison using Fig. 3a (dry BSE) and Fig. 3b (wet BSE) and the equation below, which gives the temperature dependent oxygen fugacity ( $fO_2$ ) of solar composition gas from 300 to 2500 K, which is controlled by reaction of hydrogen with water vapor (p. 33, Lodders and Fegley, 2011):

$$2H_2 + O_2 = 2H_2O$$

$$log_{10}f_{O_{2}}(solar) = 2log\bigg(\frac{X_{H_{2}O}}{X_{H_{2}}}\bigg) + 5.67 - \frac{25,664}{T}$$

Previous chemical equilibrium calculations by Schaefer and Fegley (2010) for H chondritic material give the same conclusion, significantly higher condensation temperatures in H chondritic silicate than in solar composition material (see their Table 4 and Figs. 3–5). We do not belabor this point further and refer the reader to prior papers making the same point (Fegley and Cameron, 1987; O'Neill, 1991; Visscher and Fegley, 2013; Canup et al., 2015; Lock et al., 2018; Sossi and Fegley, 2018; Sossi et al., 2019; Fegley et al., 2020).

# **4.2.** Condensation coefficients and non-equilibrium condensation (evaporation)

At thermodynamic equilibrium condensation and evaporation temperatures are identical. However, not all vapor molecules that strike the surface of a condensed phase (liquid or solid) will equilibrate with the surface and condense (Searcy, 1970). The fraction of molecules that strike the surface and condense is defined as the condensation coefficient,  $\alpha_{\text{c}}$ . Similarly, a vaporization coefficient,  $\alpha_{\text{v}}$ , is defined as the ratio of measured vapor flux to the flux calculated from the equilibrium pressure. Searcy (1970) notes that in non-equilibrium vaporization the condensation and vaporization coefficients are not strictly equal. In practice, they are probably close.

Measurements of vaporization and condensation coefficients are limited. Most measurements are for vaporization coefficients. They have been reported for some solid and liquid oxides and range from 1 to  $10^{-2}$ . Schaefer and Fegley (2004) gave a detailed discussion with their Table 10 and we briefly recapitulate some of their major points. Condensation (vaporization) coefficients are less than unity for solid oxides, e.g., Jacobson et al. (2017) report  $\alpha_v = (2 \rightarrow 5) \times 10^{-3}$  for SiO<sub>2</sub> (solid) from 1800 to 1950 K. This is about a factor of 2–3 lower than  $\alpha_v = (11-15) \times 10^{-3}$  found by Hashimoto (1990); similar differences occur

**Table 32** Dry BSE material chemistry at  $10^{-4}$  bar.

Z	SE materia Symbol	T <sub>50</sub> /K	T-range	Gas	M/MO	M/M <sup>+</sup>
	-					
3 11	Li Na	2122 1820	1775–2122 1820–2013	Li Na	65 1200	4300 46,300
19	K	1863	1863–1954	K	1300	190
37	Rb	1772	1772	Rb	400	100
55	Cs	1746	1702–1746	Cs	160	20
4	Ве	2466	-	Be	9	$1.1 \times 10^{9}$
12	Mg	2198	2197-2228	Mg	20	$1.8 \times 10^{7}$
20 38	Ca Sr	2498 2203	2411–2498 <sup>a</sup>	Ca Sr	50 8	260 35
56	Ba	2124	_	BaO	$7.9 \times 10^{-4}$	330
21	Sc	2352	_	ScO	$5.5\times10^{-5}$	9700
39	Y	2350	_	YO	$6.2 \times 10^{-6}$	2800
57	La	2147		LaO	$5.4 \times 10^{-9}$	1400
22 40	Ti Zr	2213 2498	2213–2318	${ m TiO_2} \ { m ZrO_2}$	$1.5 \times 10^{-5}$ $2.4 \times 10^{-5}$	$1.8 \times 10^{5}$ $8.0 \times 10^{3}$
72	Hf	2498	_	HfO <sup>c</sup>	$1.4 \times 10^{-6}$	$1.3 \times 10^4$
23	V	2072	_	VO <sub>2</sub>	$5.2 \times 10^{-5}$	$1.4 \times 10^7$
41	Nb	2181	_	$NbO_2$	$8.4\times10^{-8}$	$1.3\times10^6$
73	Ta	2124	-	$TaO_2$	$3.7\times10^{-10}$	$1.3 \times 10^{9}$
24	Cr	2121	_	CrO <sub>2</sub>	0.2	$5.0 \times 10^6$
42 74	Mo W	1921	-	MoO <sub>3</sub>	$1.9 \times 10^{-4}$ $1.8 \times 10^{-6}$	$3.1 \times 10^9$ $4.7 \times 10^8$
25	vv Mn	2160 2134	- 2134-2149	WO <sub>3</sub> Mn	1.8 × 10 5	$7.4 \times 10^{7}$
75	Re	1559	-	Re <sub>2</sub> O <sub>7</sub>	$6.8 \times 10^{-9}$	$1.3 \times 10^{13}$
26	Fe	2138	2138-2208	Fe	6	$5.6  imes 10^8$
44	Ru	1089	-	$RuO_3$	$4.4 \times 10^{-9}$	$8.6 \times 10^{16}$
76	Os	1404	_	OsO <sub>4</sub>	$9.4 \times 10^{-8}$	$7.5 \times 10^{16}$
27 45	Co Rh	2112 1681	_	Co RhO <sub>2</sub>	30 0.6	$2.9 \times 10^9$ $9.7 \times 10^{11}$
77	Ir	1761	_	Ir <sub>2</sub> O <sub>3</sub>	0.8	9.7 × 10 -
28	Ni	2051	_	Ni	120	$1.4\times10^{10}$
46	Pd	1197	_	PdO	$6.8  imes 10^{-3}$	$1.3\times10^{19}$
78	Pt	1772		Pt	25	
29 47	Cu	1783	1752–1783	Cu	1500 $5.6 \times 10^4$	$\begin{array}{c} 1.3 \times 10^{12} \\ 8.0 \times 10^{15} \end{array}$
47 79	Ag Au	1283 1245	1104–1283 –	Ag Au	$5.6 \times 10^4$	$1.1 \times 10^{23}$
30	Zn	1785	1785-1793	Zn	$1.1 \times 10^7$	$8.5 \times 10^{15}$
48	Cd	1733	_	Cd	$3.0\times10^4$	$3.2\times10^{15}$
80	Hg	393	-	Hg	$1.5 \times 10^{8}$	$1.7 \times 10^{86}$
5	B	1784	-	NaBO <sub>2</sub>	$1.2 \times 10^{-11}$	$1.1 \times 10^{14}$
13 31	Al Ga	2498 <sup>a</sup> 2033	2495–2498 –	AlO Ga	0.6 32	$1500 \\ 1.3 \times 10^6$
49	In	1789	_	In	32	$5.5 \times 10^6$
81	Tl	1729	_	Tl	1900	$5.4 \times 10^7$
14	Si	2159	2159–2221	SiO	$2.3 \times 10^{-8}$	$2.2 \times 10^{9}$
32	Ge	1781	1725–1783	GeO	$2.4 \times 10^{-7}$	$3.2 \times 10^{12}$
50 82	Sn Pb	1791 1782	- 1782–1789	SnO Pb	$4.4 \times 10^{-4}$	$4.8 \times 10^{10}$ $4.5 \times 10^{10}$
82 15	PD P	1782	1948–2028	PO <sub>2</sub>	$3.6 \times 10^{-5}$	$2.6 \times 10^{17}$
33	As	1804	-	AsO	$4.8 \times 10^{-2}$	$9.8 \times 10^{17}$
51	Sb	1804	-	SbO	0.25	$5.2\times10^{14}$
83	Bi	1781	-	Bi	110	$1.5 \times 10^{11}$
8 58	O Ce	2173	-	O <sub>2</sub>	$0.5$ $3.1 \times 10^{-9}$	$9.9\times10^{21}$
59	Pr	2122 2141	_	CeO <sub>2</sub> PrO	$3.1 \times 10$ $3.5 \times 10^{-8}$	-
60	Nd	2159	_	NdO	$4.7 \times 10^{-7}$	
62	Sm	2167	-	SmO	$8.1  imes 10^{-4}$	
63	Eu	2293 <sup>b</sup>	-	EuO	0.14	
64	Gd	2207	-	GdO	$7.1 \times 10^{-7}$	
65 66	Tb Dy	2256 2242	_	TbO DyO	$3.5 \times 10^{-6}$ $2.7 \times 10^{-4}$	
67	Но	2236	_	HoO	$1.2 \times 10^{-4}$	
68	Er	2276	_	ErO	$1.0 \times 10^{-4}$	
69	Tm	2288	-	TmO	$2.5  imes 10^{-2}$	
70	Yb	2264	-	Yb	2.9	
71	Lu	2286	-	LuO	$1.7 \times 10^{-5}$ $6.4 \times 10^{-9}$	060
90 92	Th U	2371 2129	_	$ThO_2$ $UO_3$	$6.4 \times 10^{-8}$ $1.6 \times 10^{-8}$	960 $8.4 \times 10^4$
94	Pu	2253	_	PuO <sub>2</sub>	$2.8 \times 10^{-6}$	250
					-	

Notes: Columns list atomic number (Z), element symbol, nominal 50% condensation temperature, the range of 50% condensation temperatures for the available activity coefficients, the major gas at the 50% condensation temperature, the molar ratio of monatomic gas to monoxide gas, and the molar ratio of monatomic gas to singly ionized monatomic gas. Dashes indicate missing data;

for example, the T-range column is blank for many elements where ideal solution calculations were done or where only one activity coefficient estimate was available. There are no data in the CONDOR code for computing the  $\rm M/M^+$  ratios for Ce to Lu.

- <sup>a</sup> Greater than 50% condensed where melt initially forms.
- $^{\rm b}\,$  Ideal solution of EuO + Eu $_2{\rm O}_3$  in the BSE melt.
- $^{\rm c}$  HfO/HfO $_2=1.01$ , see text.

for  $\alpha_v$  values for  $\alpha\text{-Al}_2O_3$  (corundum) listed in Table 10 of Schaefer and Fegley (2004). Burns (1966) found  $\alpha_v=1$  for liquid  $\text{Al}_2O_3$ ,  $\text{Ga}_2O_3$ , and  $\text{In}_2O_3$  at their melting points. However, Hashimoto (1990) reported vaporization coefficients less than unity for liquid silica and liquid Mg\_2SiO\_4. Shornikov (2015) estimated the following values for these solid rock-forming oxides:  $0.66\pm0.15$  (CaO),  $0.50\pm0.20$  (MgO),  $0.33\pm0.02$  (Al\_2O\_3),  $0.23\pm0.02$  (TiO\_2), (2.2  $\pm0.3)\times10^{-2}$  (SiO\_2), and values of unity for all the liquid oxides. More experimental data is needed to confirm or refute values of unity for all liquid oxides. The preceding discussion is only for pure solid compounds.

There are limited measurements of vaporization coefficients for specific components of complex melts (e.g., Richter et al., 2002, 2007). These are determined by taking the measured vapor flux from a free surface and comparing it to the calculated equilibrium flux using solution models (e.g., Berman, 1983; Berman and Brown, 1984). Richter et al. (2002) report vaporization coefficients from CAI-like melts for Mg and SiO ranging from 0.1 to 0.2. There is some correlation with increasing MgO content leading to larger vaporization coefficients. In their calculation of evaporation of forsterite, Tsuchiyama et al. (1999) use a vaporization coefficient of 0.1. The value of the vaporization coefficient for a particular species such as Mg or SiO depends upon the calculated activity coefficient for the parent species in the melt (e.g., MgO, SiO<sub>2</sub>). As shown in Table 2 and in figures throughout this paper, different melt models give different values for activity coefficients and thus different equilibrium flux values. The "true" values of vaporization coefficients from multicomponent melts are not yet known.

If condensation coefficients for oxide dissolution in BSE melt are less than unity the condensing flux would be reduced, and the "true" 50% condensation temperature would be higher. In the absence of constraints on condensation coefficients we assume they are unity, as done by other authors (Canup et al., 2015; Lock et al., 2018; Wang et al., 2019; Ivanov et al., 2022).

# 5. Summary

The gas – melt chemistry of bulk silicate Earth (BSE) material was modeled using ideal gas, non-ideal melt chemical equilibrium calculations over the 1000–4500 K temperature range and  $10^{-6}$  to  $10^2$  bar pressure range. The virial equation of state was used to verify the near ideality of silicate vapor (within 2%) in this pressure – temperature range. The effects of different activity coefficients and ideal solution upon the results were studied. The results presented are 50% condensation temperatures, major gases of each element, and the pressure and temperature dependent oxygen fugacity (fO2) of dry and wet BSE material. The dry BSE model has no water because it excludes hydrogen; it also excludes the volatile elements (C, N, F, Cl, Br, I, S, Se, Te). The wet BSE model has water because it includes hydrogen; it also includes the other volatiles. Key conclusions include the following: (1) much higher condensation temperatures in silicate vapor than in solar composition gas at the same total pressure because of the higher total metallicity and higher oxygen fugacity of silicate vapor, (2) a different condensation sequence in silicate vapor than in solar composition gas, (3) good agreement between different activity coefficient models except for the alkali elements, which show the largest differences between models, (4) agreement, where overlap exists, with published silicate vapor condensation calculations (e.g., Canup et al., 2015; Lock et al., 2018; Wang et al., 2019), (5) condensation of Mo and W oxides instead of metals, (6) a stability field for Ni metal as reported by Lock et al. (2018),

(7) agreement between ideal solution (from this work and from Lock et al., 2018) and real solution condensation temperatures for elements with minor deviations from ideality in the oxide melt, (8) similar 50% condensation temperatures, within a few degrees, in the dry and wet BSE models for Al, Ca, Co, Cr, Fe, Li, Mg, Mn, Si, Ti, V, and (9) much lower 50% condensation temperatures for elements such as B, Cu, K, Na, Pb, Rb, which form halide, hydroxide, sulfide, selenide, telluride and oxyhalide gases. The latter results are preliminary because solubilities and activities of volatile elements in silicate melts are not well known, but must be used for the correct equilibrium distribution, 50% condensation temperatures and mass balance of halide (F, Cl, Br, I), hydrogen, sulfur, selenium and tellurium bearing species between silicate melt and vapor.

# **Declaration of competing interest**

The authors declare that they have no known competing financial interests or personal relationships that could have appeared to influence the work reported in this paper.

# Acknowledgements

Even though we chose a different journal for publication, we thank Sasha Krot for contacting us in October 2020 about authoring a paper in Meteoritics and Planetary Science (MAPS) in memory of John Wasson, whom BF and KL knew for many years. John Wasson was a practitioner of condensation calculations and his study of moderately volatile element (MVE) condensation in the solar nebula (Wai and Wasson, 1977) strongly motivated one of us to follow suit (Fegley and Lewis, 1980). We thank Misha Petaev for sharing his 50% condensation temperatures with us, helpful discussions, and his formal review. We also thank an anonymous referee, Donna Knaster-Duvall, Astrid Holzheid, Oleg Yakovlev, Herbert Palme, Sara Port, Paolo Sossi, Channon Visscher, and Zhe Zhang for helpful comments. BF and KL thank the staff of the Interlibrary Loan Service of the Washington Universities Libraries for their superb efforts in obtaining references for us. The McDonnell Center for the Space Sciences and NSF Astronomy Program Grant AST-1517541 and AST-2108172 supported the work at Washington University.

#### References

- Alekseeva, Z.D., 1963. Equilibrium diagram of the  $\rm Rb_2SiO_3$   $\rm SiO_2$  system. Russ. J. Inorg. Chem. 8, 741–744.
- Alekseeva, Z.D., 1966. The Cs<sub>2</sub>O SiO<sub>2</sub> system. Russ. J. Inorg. Chem. 11, 626–629.
   Altman, R., 1978. Influence of Al<sub>2</sub>O<sub>3</sub> and CaO on solubility of copper in silica-saturated iron silicate slag. Trans. Inst. Min. Metall. 87, C23–C28.
- Apfelbaum, E.M., Vorob'ev, V.S., 2009. Correspondence between the critical and the Zeno-line parameters for classical and quantum liquids. J. Phys. Chem. B 113, 3521–3526.
- Apfelbaum, E.M., Vorob'ev, V.S., 2015. The wide range method to construct the entire coexistence liquid - gas curve and to determine the critical parameters of metals. J. Phys. Chem. B 119, 11825–11832.
- Aristova, N.M., Belov, G.V., Morozov, I.V., Sineva, M.A., 2018. Thermodynamic properties of condensed uranium dioxide. High Temp. 56, 652–661.
- Asano, M., Nakagawa, H., 1989. Vaporization of lithium metasilicate in a graphite Knudsen cell. J. Nucl. Mater. 161, 190–196.
- Avice, G., Marty, B., 2014. The iodine plutonium xenon age of the moon earth system revisited. Philos. Trans. R. Soc. A372, 20130260.
- Bale, C.W., Chartrand, P., Degterov, S.A., Eriksson, G., Hack, K., Mahfoud, R.B., Melançon, J., Pelton, A.D., Petersen, S., 2002. FactSage thermochemical software and databases. CALPHAD 26 (2), 189–228.
- Bale, C.W., Bélisle, E., Chartrand, P., Decterov, S.A., Eriksson, G., Hack, K., Jung, I.H., Kang, Y.B., Melançon, J., Pelton, A.D., Robelin, C., 2009. FactSage thermochemical software and databases—recent developments. CALPHAD 33 (2), 295–311.
- Bale, C.W., Belisle, E., Chartrand, P., Decterov, S.A., Eriksson, G., Gheribi, A.E., Hack, K., Jung, I.-H., Kang, Y.-B., Melançon, J., Pelton, A.D., Petersen, S., Robelin, C., Sangster, J., Spencer, P., Van Ende, M.-A., 2016. FactSage thermochemical software and databases, 2010–2016. CALPHAD 55, 1–19. https://doi.org/10.1016/j.calphad.2016.07.004.
- Ban-Ya, S., 1993. Mathematical expression of slag-metal reactions in steelmaking process by quadratic formalism based on the regular solution model. ISIJ Int. 33, 2–11.
- Ban-Ya, S., Shim, J.D., 1982. Application of the regular solution model for the equilibrium of distribution of oxygen between liquid iron and steelmaking slags. Can. Metall. Q. 21, 319–328.

- Ban-Ya, S., Hino, M., Takezoe, H., 1984. Thermodynamic properties of Fe<sub>t</sub>O Na<sub>2</sub>O, Fe<sub>t</sub>O SiO<sub>2</sub> Na<sub>2</sub>O, Fe<sub>t</sub>O P<sub>2</sub>O<sub>5</sub> Na<sub>2</sub>O, and Fe<sub>t</sub>O P<sub>2</sub>O<sub>5</sub> SiO<sub>2</sub> Na<sub>2</sub>O slags in equilibrium with solid iron. In: Fine, H.A., Gaskell, D.R. (Eds.), Proceedings of the Second International Symposium on Metallurgical Slags and Fluxes. The Metallurgical Society of AIME, Warrendale PA, pp. 395–416.
- Barin, I., 1989. Thermochemical Data of Pure Substances, Two volumes. VCH Publishing,
  Weinheim Germany
- Beckett, J.R., 2002. Role of basicity and tetrahedral speciation in controlling the thermodynamic properties of silicate liquids part 1: the system CaO MgO Al $_2$ O $_3$  SiO $_2$ . Geochim. Cosmochim. Acta 66, 93–107.
- Behrens, R.G., Rosenblatt, G.M., 1973. Vapor pressure and thermodynamics of orthorhombic antimony trioxide (valentinite). J. Chem. Thermodyn. 5, 173–188.
- Belov, G.V., Iorish, V.S., Yungman, V.S., 1999. IVTANTHERMO for windows database on thermodynamic properties and related software. CALPHAD 23, 173–180.
- Bennour, F., Rogez, J., Mathieu, J.-C., 1996a. Phase equilibria in the Na<sub>2</sub>O Cs<sub>2</sub>O SiO<sub>2</sub> system. J. Am. Ceram. Soc. 79, 2752–2754.
- Bennour, F., Chastel, R., Mathieu, J.-C., Coutures, J.-P., Bergman, C., 1996b.
  Determination of the excess thermodynamic functions in ternary Cs<sub>2</sub>O SiO<sub>2</sub> Na<sub>2</sub>O melts by Knudsen effusion mass spectrometry. Phys. Chem. Liq. 33, 229–248.
- Bennour, F., Gilbert, M., Rogez, J., Mathieu, J.C., 1999. An interacting pair model for alkaline binary and ternary liquid silicates: application to the systems Na<sub>2</sub>O-K<sub>2</sub>O-SiO<sub>2</sub> and Na<sub>2</sub>O-Cs<sub>2</sub>O-SiO<sub>2</sub>. Metall. Mater. Trans. 30B, 67–74.
- Berman, R.G., 1983. A A Thermodynamic Model for Multicomponent Melts, With Applications to the System CaO MgO Al<sub>2</sub>O<sub>3</sub> SiO<sub>2</sub>. PhD thesis, 188 pages, University of British Columbia.
- Berman, R.G., Brown, T.H., 1984. A thermodynamic model for multicomponent melts, with applications to the system CaO Al<sub>2</sub>O<sub>3</sub> SiO<sub>2</sub>. Geochim. Cosmochim. Acta 48, 661–678.
- Borisov, A.A., 2009. Influence of  $SiO_2$  and  $Al_2O_3$  on the activity coefficients of alkalis in melts: an experimental study. Petrology 17, 579–590.
- Borisov, A.A., Jones, J.H., 1999. An evaluation of Re, as an alternative to Pt, for the 1 bar loop technique: an experimental study at 1400 °C. Am. Mineral. 84, 1528–1534.
- Borisov, A.A., Walker, R.J., 2000. Os solubility in silicate melts: new efforts and results. Am. Mineral. 85, 912–917.
- Braukmüller, N., Wombacher, F., Funk, C., Münker, C., 2019. Earth's volatile depletion pattern inherited from a carbonaceous chondrite-like source. Nat. Geosci. 12, 564–568.
- Brewer, L., Greene, F.T., 1957. Differential thermal analysis of the  $Si-SiO_2$  system. J. Phys. Chem. Solids 2, 286–288.
- Brewer, L., Zavitsanos, P., 1957. A study of the  $Ge-GeO_2$  system by an inductively heated DTA apparatus. J. Phys. Chem. Solids 2, 284–285.
- Brittain, R.D., Lau, K.H., Hildenbrand, D.L., 1982. Molecular species in the As O system. J. Phys. Chem. 86. 5072–5075.
- Burnham, A.D., Berry, A.J., Halse, H.R., Schofield, P.F., Cibin, G., Mosselmans, J.F.W., 2015. The oxidation state of europium in silicate melts as a function of oxygen fugacity, composition and temperature. Chem. Geol. 411, 248–259.
- Burns, R.P., 1966. Systematics of the evaporation coefficient  $Al_2O_3$ ,  $Ga_2O_3$ ,  $In_2O_3$ . J. Chem. Phys. 44, 3307–3319.
- Cachia, J.-N., Deschanels, X., Den Auwer, C., Pinet, O., Phalippou, J., Hennig, C., Scheinost, A., 2006. Enhancing cerium and plutonium solubility by reduction in borosilicate glass. J. Nucl. Mater. 352, 182–189.
- Canali, A.C., Brenan, J.M., Sullivan, N.A., 2017. Solubility of platinum-arsenide melt and sperrylite in synthetic basalt at 0.1 MPa and 1200° C with implications for arsenic speciation and platinum sequestration in mafic igneous systems. Geochim. Cosmochim. Acta 216, 153–168.
- Canup, R.S., Visscher, C., Salmon, J., Fegley, B., 2015. Lunar volatile depletion due to incomplete accretion within an impact-generated disk. Nat. Geosci. 8, 918–921. https://doi.org/10.1038/NGEO2574.
- Capitelli, M., Lamanna, U., 1976. Second virial coefficients of oxygen oxygen and carbon oxygen interactions in different electronic states. Chem. Phys. 14, 261–266.
- Capobianco, C.J., Drake, M.J., De'Aro, J., 1999. Siderophile geochemistry of Ga, Ge, and Sn: cationic oxidation states in silicate melts and the effect of composition in ironnickel alloys. Geochim. Cosmochim. Acta 63, 2667–2677.
- Carbo-Nover, J., Richardson, F.D., 1972. Activities in SnO + SiO $_2$  melts. Trans. Inst. Min. Metall. 81, C131–C136.
- Charles, R.J., 1967. Activities in  $\text{Li}_2\text{O-}$ ,  $\text{Na}_2\text{O-}$ , and  $\text{K}_2\text{O-SiO}_2$  solutions. J. Am. Ceram. Soc. 50, 631–641.
- Chase, M.W., 1998. J. Phys. Chem. Ref. Data Monograph, Vol. 9, NIST- JANAF Thermochemical Tables, 4th ed. ACS and Melville, NY: AIP, Washington, DC.
- Chen, C., Jahanshahi, S., 2010. Thermodynamics of arsenic in FeOx CaO  $SiO_2$  slags. Metall. Mater. Trans. 41B, 1166–1174.
- Connolly, J.A.D., 2016. Liquid vapor phase relations in the Si O system: a calorically constrained van der Waals-type model. J. Geophys. Res. Planets 121. https://doi. org/10.1002/2016JE005059.
- Cordfunke, E.H.P., Ouweltjes, W., 1993. The standard molar enthalpies of formation of Cs<sub>2</sub>MnO<sub>4</sub>, Cs<sub>2</sub>Si<sub>4</sub>O<sub>9</sub>, and Cs<sub>3</sub>PO<sub>4</sub>. J. Chem. Thermodyn. 25, 1011–1016.
- Costa, G., Jacobson, N.S., Fegley Jr., B., 2017. Vaporization and thermodynamics of forsterite - rich olivine and some implications for silicate atmospheres of hot rocky exoplanets. Icarus 289, 42–55.
- Costa, G., Harder, B.J., Wiesner, V.L., Zhu, D., Bansal, N., Lee, K.N., Jacobson, N.S., Kapush, D., Ushakov, S.V., Navrotsky, A., 2018. Thermodynamics of reaction between gas-turbine ceramic coatings and ingested CMAS corrodents. J. Am. Ceram. Soc. 102, 2948–2964.
- Costa, G., Harder, B.J., Bansal, N.P., Kowalski, B.A., Stokes, J.L., 2019. Thermochemistry of calcium rare-earth silicate oxyapatites. J. Am. Ceram. Soc. 103, 1446–1453.

- Cotton, F.A., Wilkinson, G., 1972. Advanced Inorganic Chemistry: A Comprehensive Text, 3rd Edition. Wiley-Interscience, New York.
- DeMaria, G., Balducci, G., Guido, M., Piacente, V., 1971. Mass spectrometric investigation of the vaporization process of Apollo 12 lunar samples. In: Proceedings of the 2nd Lunar Science Conference, vol 2, pp. 1367–1380.
- Dhima, A., Stafa, B., Allibert, M., 1986. Activity measurements in steelmaking related oxide melts by differential mass spectrometry. High Temp. Sci. 21, 143–159.
- Drowart, J., Colin, R., Exsteen, G., 1965a. Mass-spectrometric study of the vaporization of lead monoxide. Trans. Faraday Soc. 61, 1376–1383.
- Drowart, J., Degrève, F., Verhaegen, G., Colin, R., 1965b. Thermochemical study of the germanium oxides using a mass spectrometer. Dissociation energy of the molecule GeO. Trans. Faraday Soc. 61, 1072–1085.
- Duffy, J.A., 2004. Relationship between optical basicity and thermochemistry of silicates. J. Phys. Chem. 108B, 7641–7645.
- Duffy, J.A., 2005. Optical basicity analysis of glasses containing trivalent scandium, yttrium, gallium and indium. Phys. Chem. Glasses 46, 500–504.
- Duffy, J.A., Ingram, M.D., Sommerville, I.D., 1978. Acid-base properties of molten oxides and metallurgical slags. J. Chem. Soc., Faraday Trans. 1 74, 1410–1419.
- Ebel, D.S., 2005. Model evaporation of FeO-bearing liquids: application to chondrules. Geochim. Cosmochim. Acta 69, 3183–3193.
- Ebel, D.S., Grossman, L., 2005. Spinel-bearing spherules condensed from the Chicxulub impact-vapor plume. Geology 33, 293–296.
- Eskola, P., 1922. The silicates of strontium and barium. Am. J. Sci. 4, 331–375.
- Fegley Jr., B., Cameron, A.G.W., 1987. A vaporization model for iron/silicate fractionation in the mercury protoplanet. Earth Planet. Sci. Lett. 82, 207–222.
- Fegley, B., Lewis, J.S., 1980. Volatile element chemistry in the solar nebula: Na, K, F, Cl, Br, and P. Icarus 41, 439–455.
- Fegley, B., Lodders, K., 1994. Chemical models of the deep atmospheres of Jupiter andSaturn. Icarus 110, 117–154.
- Fegley, B., Lodders, K., 2017. Chemical constraints on formation of the Moon. In: LPI Contributions No. 1987, Abstract #6227.
- Fegley, B., Lodders, K., 2021. Condensation chemistry of dry bulk silicate Earth material. In: LPI Contributions No. 2609, Abstract #6131.
- Fegley, B., Palme, H., 1985. Evidence for oxidizing conditions in the solar nebula from Mo and W depletions in refractory inclusions in carbonaceous chondrites. Earth Planet. Sci. Lett. 72, 311–326.
- Fegley, B., Jacobson, N.S., Williams, K.B., Plane, J.M.C., Schaefer, L., Lodders, K., 2016.
  Solubility of rock in steam atmospheres of planets. Astrophys. J. 824, 103.
- Fegley, B., Lodders, K., Jacobson, N.S., 2020. Volatile element chemistry during accretion of the Earth. Geochemistry 80, 125594. https://doi.org/10.1016/j. chemer.2019.125594.
- Franck, E.U., Hensel, F., 1966. Metallic conductance of supercritical mercury gas at high pressures. Phys. Rev. 147, 109–110.
- Gammie, C.F., Liao, W.-T., Ricker, P.M., 2016. A hot big bang theory: magnetic fields and the early evolution of the protolunar disk. Astrophys. J. 828, 58.
- Garg, S.P., Krishnamurthy, N., Awasthi, A., Venkatraman, M., 1996. The O-Ta (oxygen-tantalum) system. J. Phase Equilib. 17, 63–77.
- Gaskell, D.R., 1973. Introduction to Metallurgical Thermodynamics. McGraw Hill New York.
- Gaskell, D.R., 1989. Optical basicity and the thermodynamic properties of slags. Metall. Trans. 20B, 113-118.
- Ghiorso, M.S., Sack, R.O., 1995. Chemical mass transfer in magmatic processes IV. A revised and internally consistent thermodynamic model for the interpolation and extrapolation of liquid solid equilibria in magmatic systems at elevated temperatures and pressures. Contrib. Mineral. Petrol. 119, 197–212.
- Ghiorso, M.S., Carmichael, I.S.E., Rivers, M.L., Sack, R.O., 1983. The Gibbs free energy of mixing of natural silicate liquids; an expanded regular solution approximation for the calculation of magmatic intensive variables. Contrib. Mineral. Petrol. 84, 107–145.
- Ghiorso, M.S., Hirschmann, M.M., Reiners, P.W., Kress, V.C.I.I.I., 2002. The pMELTS: a revision of MELTS for improved calculation of phase relations and major element partitioning related to partial melting of the mantle to 3 GPa. Geochem. Geophys. Geosyst. 3, 5.
- Glasser, F.P., 1959. The system gallium trioxide silica ( $Ga_2O_3$   $SiO_2$ ). J. Am. Ceram. Soc. 63, 2085–2086.
- Glushko, V.P., Gurvich, L.V., Bergman, G.A., Veitz, I.V., Medvedev, V.A., Khachcurvzov, G.A., Yungman, V.S., 1982. 1978-1982. Thermodynamic Properties of Individual Substances Parts 1–4. High Temperature Institute, Moscow.
- Goldschmidt, V.M., 1928. Über die Raumerfüllung der Atome (Ionen) in Kristallen und über das Wesen der Lithosphäre. Neues Jahrbuch f. Mineral Beilage Band Abt B, 57, pp. 1119–1130.
- Goldsmith, J.R., 1950. Gallium and germanium substitutions in synthetic feldspars. J. Geol. 58, 518–536.
- Grau, A.E., Flengas, S.N., 1976. Activities of SnO in the SnO  $\rm SiO_2$  system. J. Electrochem. Soc. 123, 852–856.
- Grimley, R.T., Burns, R.P., Inghram, M.G., 1961. Thermodynamics of the vaporization of Cr<sub>2</sub>O<sub>3</sub>: dissociation energies of CrO, CrO<sub>2</sub>, and CrO<sub>3</sub>. J. Chem. Phys. 34, 664–667.
- Grover, J., 1977. Chemical mixing in multicomponent solutions: an introduction to the use of Margules and other thermodynamic excess functions to represent non-ideal behavior. In: Fraser, D.G. (Ed.), Thermodynamics in Geology. D. Reidel Publishing Co., Dordrecht, Holland, pp. 67–97.
- Gurvich, L.V., Veyts, I.V., Alcock, C.B., 1989. Thermodynamic Properties of Individual Substances, Vol. 1 (1989), Vol. 2 (1991), Vol. 3 (1994). CRC Press, Boca Raton, FL.
- Hageman, V.B.M., Oonk, H.A.J., 1986. Liquid immiscibility in the  $SiO_2 + MgO$ ,  $SiO_2 + SrO$ ,  $SiO_2 + La_2O_3$ , and  $SiO_2 + Y_2O_3$  systems. Phys. Chem. Glasses 27, 194–198.

- Hashimoto, A., 1983. Evaporation metamorphism in the early solar nebula evaporation experiments on the melt FeO-MgO-SiO $_2$ -CaO-Al $_2$ O $_3$  and chemical fractionations of primitive materials. Geochem. J. 17, 111–145.
- Hashimoto, A., 1990. Evaporation kinetics of forsterite and implications for the early solar nebula. Nature 347, 53–55.
- Hastie, J.W., Plante, E.R., Bonnell, D.W., 1982. Alkali vapor transport in coal conversion and combustion systems. In: Gole, J.L., Stwalley, W.C. (Eds.), Metal Bonding and Interactions in High Temperature Systems. American Chemical Society, Washington, DC. pp. 543–600.
- Hidayat, T., Chen, J., Hayes, P.C., Jak, E., 2021. Distributions of As, Pb, Sn, and Zn as minor elements between iron silicate slag and copper in equilibrium with tridymite in the Cu Fe O Si system. Int. J. Mater. Res. 112, 178–188.
- Hildenbrand, D.L., Lau, K.H., 1992. Thermochemistry of the gaseous osmium oxides. J. Phys. Chem. 96, 2325–2328.
- Hirschfelder, J.O., Curtiss, C.F., Bird, R.B., 1964. Molecular Theory of Gases and Liquids, Corrected Printing with Notes Added. John Wiley, NY.
- Holland, P.M., Bilosi, L., 1987. Calculation of the thermophysical properties of ground state sodium atoms. J. Chem. Phys. 87, 1261–1266.
- Holzheid, A., Lodders, K., 2001. Solubility of copper in silicate melts as function of oxygen and sulfur fugacities, temperature, and silicate composition. Geochim. Cosmochim. Acta 65, 1933–1951.
- Holzheid, A., Palme, H., Chakraborty, S., 1997. The activities of NiO, CoO and FeO in silicate melts. Chem. Geol. 139, 21–38.
- Hudson, G.B., Kennedy, B.M., Podosek, F.A., Hohenberg, C.M., 1989. The early solar system abundance of <sup>244</sup>Pu as inferred from the St. Severin chondrite. In: Proceedings of the 19th Lunar and Planetary Science Conference, 19, pp. 547–557.
- Itoh, M., Yokokawa, T., 1984. Thermodynamic activity of Na<sub>2</sub>O in Na<sub>2</sub>O SiO<sub>2</sub> Al<sub>2</sub>O<sub>3</sub> melt. Trans. Jpn. Inst. Metals 25, 879–884.
- Ivanov, D., Fitoussi, C., Bourdon, B., 2022. Trace element volatility and the conditions of liquid vapor separation in the proto-lunar disk. Icarus 386, 115–143.
- Jacob, K.T., Rajput, A., 2015. Phase relations in the system Ca-Ta-O and thermodynamics of calcium tantalates in relation to calciothermic reduction of Ta<sub>2</sub>O<sub>5</sub>. J. Alloys Compd. 620, 256–262.
- Jacob, K.T., Shekhar, C., Waseda, Y., 2009. An update on the thermodynamics of Ta<sub>2</sub>O<sub>5</sub>.
  J. Chem. Thermodyn. 41, 748–753.
- Jacobson, N.S., 1989. Thermodynamic properties of some metal oxide zirconia systems. In: NASA Technical Memorandum 102351, NASA Lewis Research Center (63 pages).
- Jacobson, N.S., Copland, E.H., Kaufman, L., 2001a. Thermodynamic database for the NdO<sub>1.5</sub> - YO<sub>1.5</sub> - YDO<sub>1.5</sub> - ScO<sub>1.5</sub> - ZrO<sub>2</sub> system. In: NASA Technical Memorandum TM-2001-210753. NASA Glenn Research Center (50 pages).
- Jacobson, N.S., Myers, D.L., Zhu, D., Humphrey, D.L., 2001b. Rhenium/oxygen interactions at elevated temperatures. Oxid. Met. 55, 471–480.
- Jacobson, N.S., Ingersoll, N., Myers, D.L., 2017. Vaporization coefficients of SiO<sub>2</sub> and MgO. J. Eur. Ceram. Soc. 37, 2245–2252.
- Jeffes, J.H.E., Sridhar, R., 1968. Thermodynamics of PbO PbF $_2$  melts. Trans. Inst. Min. Metall. 77, C53–C56.
- Jiang, Y., Chen, H., Fegley Jr., B., Lodders, K., Hsu, W., Jacobsen, S.B., Wang, K., 2019. Implications of K, Cu and Zn isotopes for the formation of tektites. Geochim. Cosmochim. Acta 259, 170–187.
- Jiang, Y., Mofarah, S.S., Koshy, P., Chen, W.-F., Fang, X., Zheng, X., Wang, D., Sorrell, C. C., 2021. Na<sub>0.5</sub>Bi<sub>0.5</sub>TiO<sub>3</sub> phase relations: thermodynamics and phase equilibria in the systems Bi<sub>2</sub>O<sub>3</sub> TiO<sub>2</sub>, Na<sub>2</sub>O TiO<sub>2</sub>, and Na<sub>2</sub>O Bi<sub>2</sub>O<sub>3</sub> TiO<sub>2</sub>. J. Eur. Ceram. Soc. 41, 7005–7013
- Johnston, W.D., 1965. Oxidation reduction equilibria in molten  $Na_2O \cdot 2SiO_2$  glass. J. Am. Ceram. Soc. 48, 184–190.
- Jung, I.-H., Hudon, P., 2012. Thermodynamic assessment of  $P_2O_5$ . J. Am. Ceram. Soc. 95, 3665–3672.
- Kambayashi, S., Kato, E., 1984. A thermodynamic study of (magnesium oxide + silicon dioxide) by mass spectrometry at 1973 K. J. Chem. Thermodyn. 16, 241–248.
- Kargin, Yu.F., Ivicheva, S.N., Shvorneva, L.I., 2008. Phase relations in the MgO  $Bi_2O_3$   $B_2O_3$  system. Russ. J. Inorg. Chem. 53, 1297–1299.
- Katayama, I., Sugimura, S., Kozuka, Z., 1987. Measurements of standard molar Gibbs energies of formation of Sb<sub>2</sub>O<sub>3</sub>, ZnSb<sub>2</sub>O<sub>4</sub>, and MgSb<sub>2</sub>O<sub>4</sub> by EMF method with zirconia solid electrolyte. Trans. Jpn. Inst. Metals 28, 406–411.
- Katayama, I., Kemori, N., Denholm, W.T., 1998. Thermodynamic study of CaO  $Sb_2O_3$  system by emf method. Ber. Bunsenges. Phys. Chem. 102, 1272–1274.
- Kato, Y., Asano, M., Harada, T., Mizutani, Y., 1993. Mass-spectrometric study of vaporization and thermodynamic properties of  $\rm Li_2ZrO_3$  (s). J. Nucl. Mater. 203, 27–35.
- Kazenas, E.K., Petrov, A.A., 1997. Thermodynamics of processes of phosphorus oxides and arsenic. Russ. Metall. 1997 (1), 29–34.
- Kegler, P., Holzheid, A., 2011. Determination of the formal Ge-oxide species in silicate melts at oxygen fugacities applicable to terrestrial core formation scenarios. Eur. J. Mineral. 23, 369–378.
- Kim, S.S., Sanders, T.H., 1991. Thermodynamic modeling of phase diagrams in binary alkali silicate systems. J. Am. Ceram. Soc. 74, 1833–1840.
- Kim, D.G., Van Enge, M.-A., Van Hoek, C., Sieger, C.L., Jung, I.-H., 2012. A critical evaluation and thermodynamic optimization of the CaO CaF $_2$  system. Metall. Mater. Trans. 43B, 1315–1325.
- Klein, W., Jansen, M., 2008. Synthesis and crystal structure of silver neosilicate, Ag<sub>4</sub>SiO<sub>4</sub>.
  Z. Anorg, Allg. Chem. 634, 1077–1081.
- Knacke, O., Kubaschewski, O., Hesselmann, K., 1991. Thermochemical Properties of Inorganic Substances, Two volumes. Springer-Verlag, Berlin, Germany.
- Kobsch, A., Caracas, R., 2020. The critical point and supercritical state of alkali feldspars: implications for the behavior of the crust during impacts. J. Geophys. Res. Planets 125, e2020JE006412.

- Konar, B., Kim, D.-G., Jung, I.-H., 2018. Critical thermodynamic optimization of the  $\rm Li_2O$   $\rm Al_2O_3$   $\rm SiO_2$  system and its application for the thermodynamic analysis of the glass-ceramics. J. Eur. Ceram. Soc. 38, 3881–3904.
- Kornacki, A.S., Fegley, B., 1986. The abundance and relative volatility of refractory trace elements in Allende Ca,Al-rich inclusions: implications for chemical and physical processes in the solar nebula. Earth Planet. Sci. Lett. 79, 217–234.
- Kosenko, A.V., Emel'chenko, G.A., 2001. Equilibrium phase relations in the system Cu-O under high oxygen pressure. J. Phase Equilib. 22, 12–19.
- Koster van Groos, A.F., Wyllie, P.J., 1969. Melting relationships in the system NaAlSi $_3$ O $_8$  NaCl  $_4$ O at one kilobar pressure with petrological applications. J. Geol. 77, 581–605.
- Kozuka, Z., Siahaan, O.P., Moriyama, J., 1968. Thermodynamic study of molten SnO -SiO<sub>2</sub> system. Trans. Jpn. Inst. Metals 9, 200–204.
- Kracek, F.C., 1933. Studies on Alkali Silicates. Year Book Carnegie Institution of Washington, pp. 61–65.
- Kubaschewski, O., 1972. The thermodynamic properties of double oxides (a review). High Temp.–High Pressures 4, 1–12.
- Kubaschewski, O., Alcock, C.B., 1979. Metallurgical Thermochemistry, 5th ed. Pergamon.
- Lambotte, G., Chartrand, P., 2013. Thermodynamic modeling of the ( $Al_2O_3 + Na_2O$ ), ( $Al_2O_3 + Na_2O + SiO_2$ ), and ( $Al_2O_3 + Na_2O + AlF_3 + NaF$ ) systems. J. Chem. Thermodyn. 57, 306–334.
- Lapshin, A.E., Borisova, N.V., Ushakov, V.M., Shepelev, Yu.F., 2006a. Structure and some thermodynamic characteristics of the polymorphs of rubidium silicate  $Rb_6Si_{10}O_{23}$ . Russ. J. Inorg. Chem. 51, 438–444.
- Lapshin, A.E., Borisova, N.V., Ushakov, V.M., Shepelev, Yu.F., 2006b. Crystal structure and some thermodynamic characteristics of cesium silicate Cs<sub>6</sub>Si<sub>10</sub>O<sub>23</sub>. Russ. J. Inorg. Chem. 51, 1696–1700.
- Lebouteiller, A., Courtine, P., 1998. Improvement of a bulk optical basicity table for oxidic systems. J. Solid State Chem. 137, 94–103.
- Lin, R.Y., Elliott, J.F., 1983. Thermochemistry of  $Na_2O-WO_3$  system at 1065 to 1239 K. Met. Trans. 14A, 1713–1720.
- Lin, R.Y., Elliott, J.F., 2001. High-temperature electrochemical study of  $Na_2O-MoO_3$  melts. J. Alloys Compd. 321, 261–266.
- Linard, Y., Wilding, M.C., Navrotsky, A., 2008. High temperature calorimetric studies of heat of solution of NiO, CuO, La<sub>2</sub>O<sub>3</sub>, TiO<sub>2</sub>, HfO<sub>2</sub> in sodium silicate liquids. Geochim. Cosmochim. Acta 72, 590–601.
- Lock, S.J., Stewart, S.T., Petaev, M.I., Leinhardt, Z., Mace, M.T., Jacobsen, S.B., Ćuk, M., 2018. The origin of the moon within a terrestrial synestia. J. Geophys. Res. Planets 123, 910–951. https://doi.org/10.1002/2017JE005333.
- Lodders, K., 2003. Solar system abundances and condensation temperatures of the elements. Astrophys. J. 591, 1220–1247.
- Lodders, K., Fegley, B., 1993. Lanthanide and actinide chemistry at high C/O ratios in the solar nebula. Earth Planet. Sci. Lett. 117, 125–145.
- Lodders, K., Fegley Jr., B., 2011. Chemistry of the Solar System. RSC Publishing, Cambridge.
- Lopatin, S.I., Shugurov, S.M., Stolyarova, V.L., Tyurnina, N.G., 2006. Thermodynamic properties of silicate glass and melts: II. System SrO - SiO<sub>2</sub>. Russ. J. Gen. Chem. 76, 1878–1884.
- Lopatin, S.I., Shugurov, S.M., Stolyarova, V.L., 2007. Thermodynamic properties of silicate glasses and melts: III. System  $Rb_2O-B_2O_3-SiO_2$ . Russ. J. Gen. Chem. 77, 997–1001.
- Lumsden, J., 1961. The thermodynamics of liquid iron silicates. In: Pierre, G. St (Ed.), Physical Chemistry of Process Metallurgy Part 1. Wiley Interscience, New York, pp. 165–205.
- Lumsden, J., 1966. Thermodynamics of Molten. Salt Mixtures Academic Press, London. Lupu, R.E., Zahnle, K., Marley, M.S., Schaefer, L., Fegley, B., Morley, C., Cahoy, K., Freedman, R., Fortney, J.J., 2014. The atmospheres of Earthlike planets after giant impact events. Astrophys. J. 784 (27), 19.
- Maciag, B.J., Brenan, J.M., 2020. Speciation of arsenic and antimony in basaltic magmas. Geochim. Cosmochim. Acta 276, 198–218.
- Maekawa, T., Yokokawa, T., Niwa, K., 1969. Solubility of  $Ag_2O$  in  $Na_2O-B_2O_3$  melts. Bull. Chem. Soc. Jpn. 42, 677–681.
- Mare, E.R., O'Neill, H.S.T.C., Berry, A.J., Glover, C.J., 2020. The stability of divalent Ge in silicate melts and its geochemical properties. Chem. Geol. 532, 119306.
- Markova, O.M., Yakovlev, O.I., Semenov, G.A., Belov, A.N., 1986. Evaporation of natural melts in a Knudsen chamber. Geokhimiya 11, 1559–1569.
- Martin, E., Bell, H.B., 1974. Activities in the MnO TiO  $_2$  system at 1500  $^{\circ}$  C. Trans. Inst. Min. Metall. 83, C193–C196.
- Mason, E.H., Spurling, T.H., 1969. The Virial Equation of State. Pergamon Press, Oxford. Mathieu, R., Khedim, H., Libourel, G., Podor, R., Tissandier, L., Deloule, E., Faure, F., Rapin, C., Vilasi, M., 2008. Control of alkali-metal oxide activity in molten silicates. J. Non-Cryst. Solids 354, 5079–5083.
- Mathieu, R., Libourel, G., Deloule, E., Tissandier, L., Rapin, C., Podor, R., 2011. Na<sub>2</sub>O solubility in CaO MgO SiO<sub>2</sub> melts. Geochim. Cosmochim. Acta 75, 608–628.
- Melosh, H.J., 2007. A hydrocode equation of state for  $SiO_2$ . Meteorit. Planet. Sci. 42, 2079–2098.
- Morishita, M., Navrotsky, A., Wilding, M.C., 2004. Direct measurement of relative partial molar enthalpy of  $SiO_2$  in  $SiO_2 M_2O$  (M = Li, Na, K, Cs) binary and  $CaO SiO_2 Al_2O_3$  ternary melts. J. Am. Ceram. Soc. 87, 1550–1555.
- Morris, R.V., Haskin, L.A., Biggar, G.M., O'Hara, M.J., 1974. Measurement of the Effects of Temperature and Partial Pressure of Oxygen on the Oxidation State of Europium in Silicate Glasses, 38, pp. 1447–1459.
- Muenow, D.W., Uy, O.M., Margrave, J., 1970. Mass spectrometric studies of the vaporization of phosphorus oxides. J. Inorg. Nucl. Chem. 32, 3459–3467.

- Nagabayashi, R., Hino, M., Ban-Ya, S., 1989. Mathematical expression of phosphorus distribution in steelmaking process by quadratic formalism. ISIJ Int. 29, 140–147.
- Nakagawa, H., Asano, M., Kubo, K., 1982. Mass spectrometric investigation of the vaporization of Li<sub>2</sub>TiO<sub>3</sub> (s). J. Nucl. Mater. 110, 158–163.
- Nassaralla, C., Fruehan, R.J., 1992. Phosphate capacity of CaO-Al<sub>2</sub>O<sub>3</sub> slags containing CaF<sub>2</sub>, BaO, Li<sub>2</sub>O, or Na<sub>2</sub>O. Metall. Trans. 23B, 117–123.
- Navrotsky, A., 1977. Recent progress and new directions in high temperature calorimetry. Phys. Chem. Minerals 2, 89–104.
- Navrotsky, A., 1994. Repeating patterns in mineral energetics. Am. Mineral. 79, 589–604.
- Neuman, M., Holzheid, A., Lodders, K., Fegley Jr., B., Jolliff, B.L., Koefoed, P., Chen, H., Wang, K., 2022. High temperature evaporation and isotopic composition of K, Cu and Zn. Geochim. Cosmochim. Acta 316, 1–20.
- Nuta, I., Chatillon, C., Roki, F.-Z., Fischer, E., 2021. Gaseous phase above Ru-O system: a thermodynamic data assessment. CALPHAD 75, 102329.
- Odoj, R., Hilpert, K., 1980a. Mass spectrometric study of the evaporation of crystalline compounds in the Cs<sub>2</sub>O Al<sub>2</sub>O<sub>3</sub> SiO<sub>2</sub> system. I.The synthetic compound CsAlSi<sub>2</sub>O<sub>6</sub> and the mineral pollucite. High Temp.–High Pressures 12, 93–98.
- Odoj, R., Hilpert, K., 1980b. Mass spectrometric investigations of the evaporation of crystalline compounds in the system  $Cs_2O Al_2O_3 SiO_2$  Part II: the compounds  $CsAlSiO_4$  and  $CsAlSi_5O_{12}$ . Z. Naturforsch. 35a:9–13.
- O'Horo, M.P., White, W.B., 1971. Phase equilibria in the systems CdF<sub>2</sub> CaF<sub>2</sub>, CdF<sub>2</sub> PbF<sub>2</sub>, and CdF<sub>2</sub> ZnF<sub>2</sub>. J. Am. Ceram. Soc. 54, 588–589.
- Ohse, R.W., Babelot, J.-F., Magill, J., Tetenbaum, M., 1985. An assessment of the melting, boiling, and critical point data of the alkali metals. Pure Appl. Chem. 57, 1407–1426
- O'Neill, H.S.T.C., 1991. The origin of the Moon and the early history of the Earth a chemical model. Part 1: The Moon. Geochim. Cosmochim. Acta 55, 1135–1157.
- O'Neill, H.S.T.C., Nell, J., 1997. Gibbs free energies of formation of RuO<sub>2</sub>, IrO<sub>2</sub>, and OsO<sub>2</sub>: a high-temperature electrochemical and calorimetric study. Geochim. Cosmochim. Acta 61, 5279–5293.
- O'Neill, H.S.T.C., Berry, A.J., Eggins, S.M., 2008. The solubility and oxidation state of tungsten in silicate melts: implications for the comparative chemistry of W and Mo in planetary differentiation processes. Chem. Geol. 255, 346–359.
- Otto, E.M., 1966. Equilibrium pressures of oxygen over oxides of lead at various temperatures. J. Electrochem. Soc. 113, 525–527.
- Palme, H., O'Neill, H.St.C., 2014. Cosmochemical estimates of mantle composition. Treatise on Geochemistry, 2nd ed. Elsevier, Amsterdam, pp. 1–39.
- Paul, A., 1990. Oxidation reduction equilibrium in glass. J. Non-Cryst. Solids 123, 354–362.
- Paulina, L., Swinbourne, D.R., Kho, T.S., 2013. Distribution of bismuth between copper and FeO<sub>x</sub> - CaO - SiO<sub>2</sub> slags under copper converting conditions. Trans. Inst. Min. Metall. 122C. 79–86.
- Petaev, M.I., 2009. The GRAINS thermodynamic and kinetic code for modeling nebular condensation. CALPHAD 33. 317–327.
- Petaev, M.I., Jacobsen, S.B., Huang, S., 2014. Testing models of Moon origin: condensation of impact-vaporised bulk silicate Earth material. In: Abstract 2316 45th Lunar and Planetary Science Conference.
- Petaev, M.I., Jacobsen, S.B., Huang, S., 2015. Testing models of the Moon's origin, II: phase relations in a proto-lunar disk of the BSE composition. In: Abstract 2254. 46th Lunar and Planetary Science Conference.
- Petaev, M.I., Jacobsen, S.B., Huang, S., Lock, S.J., Stewart, S.T., 2016. Testing models of the Moon's origin, III: Phase diagram of a proto-lunar disk and condensation of trace elements. In: Abstract 2468. 47th Lunar and Planetary Science Conference
- Pistorius, P.C., 2006. Research in pyrometallurgy at the university of Pretoria, 1980–2005. In: Jones, R.T. (Ed.), South African Pyrometallurgy 2006. South African Institute of Mining and Metallurgy, Johannesburg, S. Africa, pp. 105–114.
- Pitzer, K.S., Brewer, L., 1961. Thermodynamics, 2nd ed. McGraw Hill, NY.
- Platteeuw, J.C., Meyer, G., 1956. The system tin  $\pm$  oxygen. Trans. Faraday Soc. 52,  $\pm$  1066–1073.
- Pottlacher, G., Jäger, H., 1996. A review of determinations of critical point data of metals using subsecond pulse heating techniques. J. Non-Cryst. Solids 205–207, 265–269.
- Pownceby, M.I., O'Neill, H.S.T.C., 1994. Thermodynamic data from redox reactions at high temperatures. IV. Calibration of the Re ReO<sub>2</sub> oxygen buffer from EMF and NiO + Ni-Pd redox sensor measurements. Contrib. Mineral. Petrol. 118, 130–137.
- Pretorius, E.B., Muan, A., 1992. Activity composition relations of chromium oxide in silicate melts at 1500  $^{\circ}$ C under strongly reducing conditions. J. Am. Ceram. Soc. 75, 1364–1377.
- Reddy, R.R., Ahammed, Y.N., Azeem, P.A., Gopal, K.R., Rao, T.V.R., 2001. Electronic polarizability and optical basicity properties of oxide glasses through average electronegativity. J. Non Cryst. Solids 286 (3), 169–180.
- Rey, M., 1948. The thermodynamic activity of silica and of oxides in silicate melts. Discuss. Faraday Soc. 4, 257–265.
- Reyes, R.A., Gaskell, D.R., 1983. The thermodynamic activity of ZnO in silicate melts. Metall. Trans. 14B, 725–731.
- Richards, A.W., Thorne, D.F.J., 1961. The activities of zinc oxide and ferrous oxide in liquid silicate slags. In: Pierre, G. St (Ed.), Physical Chemistry of Process Metallurgy Part 1. Wiley Interscience, New York, pp. 277–291.
- Richter, F.M., Davis, A.M., Ebel, D.S., Hashimoto, A., 2002. Elemental and isotopic fractionation of Type B calcium-, aluminum-rich inclusions: experiments, theoretical considerations, and constraints on their thermal evolution. Geochim. Cosmochim. Acta 66, 521–540.
- Richter, F.M., Janney, P.E., Mendybaev, R.A., Davis, A.M., Wadhwa, M., 2007. Elemental and isotopic fractionation of Type B CAI-like liquids by evaporation. Geochim. Cosmochim. Acta 71, 5544–5564.

- Ringwood, A.E., Kesson, S.E., 1977. Basaltic magmatism and the bulk composition of the Moon. II. Siderophile and volatile elements in Moon, Earth and chondrites: implications for lunar origin. Moon 16, 425-464.
- Robbins, C.R., Levin, E.M., 1959. The system magnesium oxide germanium dioxide. Am. J. Sci. 257, 63-70.
- Roberts, H.S., Smyth, F.H., 1921. The system copper: cupric oxide oxygen. J. Am. Chem. Soc. 43, 1061-1079.
- Robie, R.A., Hemingway, B.S., 1995. Thermodynamic properties of minerals and related substances at 298.15°K and 1 bar (10<sup>5</sup> Pascals) pressure and at higher temperatures. U.S. Geol. Surv. Bull. 2131.
- Ryerson, F.J., 1985. Oxide solution mechanisms in silicate melts: systematic variations in the activity coefficient of  $SiO_2$ . Geochim. Cosmochim. Acta 49, 637–649.
- Samarin, A., Temkin, M., Shvarzman, L., 1945. Distribution of sulphur between metal and slag from the viewpoint of the ionic nature of slag. Acta Physicochim. URSS 20,
- Schaefer, L., Fegley, B., 2004. A thermodynamic model of high temperature lava vaporization on Io. Icarus 169, 216-241.
- Schaefer, L., Fegley, B., 2010. Volatile element chemistry during metamorphism of ordinary chondritic material and some of its implications for compositions of asteroids. Icarus 205, 483-496.
- Schick, H.L., 1966. Thermodynamics of Certain Refractory Compounds, Two volumes. Academic Press, New York.
- Schmid, R., 1983. A thermodynamic analysis of the Cu-O system with an associated solution model. Metall. Trans. 14B, 473-481.
- Schramm, L., Behr, G., Löser, W., Wetzig, K., 2005. Thermodynamic reassessment of the Cu-O phase diagram, J. Phase Equilib. Diffus. 26, 605-612.
- Searcy, A.W., 1970. The kinetics of evaporation and condensation reactions. In: Searcy, A.W., Ragone, D.V., Colombo, U. (Eds.), Chemical and Mechanical Behavior of Inorganic Materials, 1970. John Wiley & Sons, New York, pp. 107-133.
- Semenov, G.A., Frantseva, K.E., Aurova, O.A., 1983. Mass-spectrometric study of the evaporation of antimony oxide. Izv Vyss Uchebnyk Zaved Khimiya I Khimicheskaya Tekhnologiya 26, 66-70.
- Shakhmatkin, B.A., Vedishcheva, N.M., 1994. Thermodynamic studies of glass-forming liquids by the electromotive force method. J. Non-Cryst. Solids 171, 1–30.
- Shannon, R.D., 1976. Revised effective ionic radii and systematic studies of interatomic distances in halides and chalcogenides. Acta Crystallogr. Sect. A 32, 751–767.
- Shornikov, S.I., 2015. Vaporization coefficients of oxides contained in the melts of Ca-Alinclusions in chondrites. Geochem. Int. 53, 1080–1089.
- Shornikov, S.I., 2020. Study of CaO TiO<sub>2</sub> melts by Knudsen effusion mass spectrometry. Russ. J. Phys. Chem. 94, 1289-1299.
- Shornikov, S.I., Stolyarova, V.L., Shul'ts, M.M., 1997. A mass-spectrometric study of vapor composition and thermodynamic properties of CaO - Al<sub>2</sub>O<sub>3</sub> melts. Russ. J. Phys. Chem. 71, 19-22.
- Shuva, M.A.H., Rhamdhani, M.R., Brooks, G.A., Masood, S., Reuter, M.A., 2016. Thermodynamics behavior of germanium during equilibrium reactions between FeO<sub>x</sub> - CaO - SiO<sub>2</sub> - MgO slag and molten copper. Metall. Mater. Trans. 47B, 2889-2903.
- Skinner, H.B., Searcy, A.W., 1973. Mass spectrometric studies of gaseous oxides of
- rhenium. J. Phys. Chem. 77, 1578–1585. Sommerville, I.D., Ivanchev, I., Bell, H.B., 1973. Activity in melts containing FeO, MnO, Al<sub>2</sub>O<sub>3</sub>, and SiO<sub>2</sub>. In: Chemical Metallurgy of Iron and Steel. The Iron and Steel Institute, London, pp. 23-25.
- Sossi, A., Fegley Jr., B., 2018. Thermodynamics of element volatility and its application to planetary processes. In: King, P.L., Fegley Jr., B., Seward, T. (Eds.), Reviews in Mineralogy and Geochemistry, vol 84, pp. 393-459.
- Sossi, P.A., Klemme, S., O'Neill HStC., Berndt J., and Moynier F., 2019. Evaporation of moderately volatile elements from silicate melts: experiments and theory. Geochim. Cosmochim. Acta 260, 204-231.
- Stolyarova, V.L., Lopatin, S.I., 2005. Mass spectrometric study of the vaporization and thermodynamic properties of components in the BaO - TiO2 - SiO2 system. Glass Phys. Chem. 31, 132-137.
- Stolyarova, V.L., Semenov, G.A., 1994. Mass Spectrometric Study of the Vaporization of Oxide Systems. Wiley & Sons, Chichester.
- Stolyarova, V.L., Shornikov, S.I., Ivanov, G.G., Shultz, M.M., 1991. High temperature mass spectrometric study of thermodynamic properties of the CaO - SiO2 system. J. Electrochem. Soc. 138, 3710-3714.
- Stolyarova, V.L., Shornikov, S.I., Shul'ts, M.M., 1996. Mass spectrometric study of vaporization processes and thermodynamic properties of diopside. Rapid Commun. Mass Spectrom. 10, 443-446.
- Stolyarova, V.L., Vorozhtcov, V.A., Shilov, A.L., Lopatin, S.I., Shugurov, S.M., 2020. Ceramics based on the Sm2O3 - Y2O3 and Sm2O3 - HfO2 systems at high temperatures: thermodynamics and modelling. Mater. Chem. Phys. 252, 123240.
- Suito, H., Inoue, R., Takada, M., 1981. Phosphorus distribution between liquid iron and MgO saturated slags of the system CaO - MgO - FeOx - SiO2. Tetsu-to-Hagane 67, 2645-2654.
- Suzuki, E., Nakajima, K., Osaka, M., Ohishi, Y., Muta, H., Kurosaki, K., 2020. Low temperature heat capacity of Cs<sub>2</sub>Si<sub>4</sub>O<sub>9</sub>. J. Nucl. Sci. Technol. 57, 852-857
- Svehla R. A. 1962. Estimated viscosities and thermal conductivities of gases at high temperatures. NASA Technical Report R-132, (122 pages).

- Takahashi, E., 1986. Melting of a dry peridotite KLB-1 up to 14 GPa: implications on the origin of peridotitic upper mantle. J. Geophys. Res. 91, 9367-9382.
- Temkin, M., 1945. Mixtures of fused salts as ionic solutions. Acta Physicochim. URSS 20, 411-420.
- Tian, Z., Magna, T., Day, J.M.D., Mezger, K., Scherer, E.E., Lodders, K., Hin, R.C., Koefoed, P., Bloom, H., Wang, K., 2021. Potassium isotope composition of Mars reveals a mechanism of planetary volatile retention. Proc. Natl. Acad. Sci. 118 (E39).
- Toker, N.Y., Darken, L.S., Muan, A., 1991. Equilibrium phase relations and thermodynamics of the Cr-O system in the temperature range of 1500 °C to 1825 °C. Metall. Trans. 22B, 225-232.
- Townsend, J.P., Shohet, G., Cochrane, K.R., 2020. Liquid vapor coexistence and critical point of Mg<sub>2</sub>SiO<sub>4</sub> from ab initio simulations. Geophys. Res. Lett. 47, e2020GL089599
- Tsuchiyama, A., Tachibana, S., Takahashi, T., 1999. Evaporation of forsterite in the primordial solar nebula; rates and accompanied isotopic fractionation. Geochim. Cosmochim. Acta 63, 2451–2466.
- Turkdogan, E.T., 1962. Diffusivities of gases and metal vapors at elevated temperatures. In: Elliott, J.F., Meadowcroft, T.R. (Eds.), Steelmaking: The Chipman Conference. MIT Press, Cambridge MA, pp. 77-87.
- Turkdogan, E.T., 1983. Physicochemical Properties of Molten Slags and Glasses. The Metals Society, London.
- Tyurnina, A.G., Lopatin, S.I., Shugurov, S.M., Stolyarova, V.L., 2005. Thermodynamic properties of silicate glass and melts: I. BaO - SiO<sub>2</sub>. Russ. J. Gen. Chem. 76,
- Visscher, C., Fegley, B., 2013. Chemistry of impact-generated silicate melt-vapor debris disks. Astrophys. J. Lett. 767, L12. https://doi.org/10.1088/2041-8205/767/1/L12.
- Wai, C.M., Wasson, J.T., 1977. Nebular condensation of moderately volatile elements and their abundances in ordinary chondrites. Earth Planet. Sci. Lett. 36, 1-13.
- Wakasugi, T., Hirota, A., Fukunaga, J., Ota, R., 1997. Solubility of Ag<sub>2</sub>O in the Na<sub>2</sub>O - $B_2O_3 - Al_2O_3$  system. J. Non-Cryst. Solids 210, 141–147.
- Wang, J., Davis, A.M., Clayton, R.N., Mayeda, T.K., Hashimoto, A., 2001. Chemical and isotopic fractionation during the evaporation of the FeO-MgO-SiO<sub>2</sub>-CaO-Al<sub>2</sub>O<sub>3</sub>-TiO<sub>2</sub> rare earth element melt system. Geochim. Cosmochim. Acta 65, 479-494.
- Wang, X., Fitoussi, C., Bourdon, B., Fegley Jr., B., Charnoz, S., 2019. Tin isotopes indicative of liquid - vapour equilibration and separation in the Moon-forming disk. Nat. Geosci. 12, 707–711.
- Watson, L.R., Thiem, T., Dressler, R.A., Salter, R.H., Murad, E., 1991. Thermochemical properties of the osmium oxides. J. Phys. Chem. 95, 8944–8947.
- Wilding, M.C., Navrotsky, A., 1998. The dissolution of silica and alumina in silicate melts: in situ high temperature calorimetric studies. Neues Jb. Mineral. Abh. 172 177-201.
- Willis, G.M., Hennessy, F.L., 1953. System  $Ag_2O B_2O_3$ ; its thermodynamic properties as a slag model, JOM 5, 1367-1372.
- Wood, B.J., Wade, J., 2013. Activities and volatilities of trace components in silicate melts: a novel use of metal - silicate partitioning data. Contrib. Mineral. Petrol. 166, 911-921.
- Woolley, H.W., 1962. The calculation of thermodynamic properties of gases at high temperature. In: Technical Report No. AFSWC-TDR-62-21. National Bureau of Standards, March 1962.
- Wriedt, H.A., 1987a, The O Zn (oxygen zinc) system, Bull, Alloy Phase Diagr. 8, 166-176.
- Wriedt, H.A., 1987b. The Cd-O (cadmium oxygen) system. Bull. Alloy Phase Diagr. 8, 140-147
- Yan, S., Swinbourne, D.R., 2003. Distributions of germanium under lead smelting conditions, Miner, Process, Extr. Metall, 112 (2), 75-80.
- Yazhenskikh, E., Hack, K., Müller, M., 2011. Critical thermodynamic evaluation of oxide systems relevant to fuel ashes and slags, Part 5: potassium oxide - alumina - silica. CALPHAD 35, 6-19.
- Yoshikawa, T., Astuti, I., Takahashi, H., Morita, K., 2004. Thermodynamic properties of the  $SiO_2$  –  $GeO_2$  and Pt-rich Pt – Ge systems at 1623 and 1723 K. Mater. Trans. 45, 1847-1851.
- Zaitsev, A.I., Mogutnov, B.M., 1995. Thermodynamic properties and phase equilibria in the MnO –  $SiO_2$  system. J. Mater. Chem. 5, 1063–1073.
- Zaitsev, A.I., Shelkova, N.E., Lyakishev, N.P., Mogutnov, B.M., 1999. Thermodynamic properties and phase equilibria in the Na2O - SiO2 system. Phys. Chem. Chem. Phys. 1, 1899-1907.
- Zaitsev, A.I., Shelkova, N.E., Lyakishev, N.P., Mogutnov, B.M., 2000a. The thermodynamic properties of  $\mathrm{K}_2\mathrm{O}$  -  $\mathrm{SiO}_2$  melts. Russ. J. Phys. Chem. 74, 907–913.
- Zaitsev, A.I., Shelkova, N.E., Lyakishev, N.P., Mogutnov, B.M., 2000b. Modeling of the thermodynamic properties of silicate melts and calculation of phase equilibria in the K<sub>2</sub>O - SiO<sub>2</sub> system. Russ. J. Phys. Chem. 74, 1033-1038.
- Zhang, Z.J., Nie, N.X., Mendybaev, R.A., Liu, M.-C., Hu, L.J., Hopp, T., Alp, E.E., Lavina, B., Bullock, E.S., McKeegan, K.D., Dauphas, N., 2021. Loss and isotopic fractionation of alkali elements during diffusion-limited evaporation from molten silicate: theory and experiments. ACS Earth Space Chem. https://doi.org/10.1021/ csearthspacechem.0c00263.
- Zhi, W., Wang, F., Yang, B., Qu, T., Deng, Y., Tian, Y., Zhao, J., 2019. Phase relations of CaO - Al<sub>2</sub>O<sub>3</sub> - Sc<sub>2</sub>O<sub>3</sub> ternary system. J. Am. Ceram. Soc. 102, 2863–2870.
- Zolotov, M.Yu., Fegley Jr., B., 1999. Oxidation state of volcanic gases and the interior of Io. Icarus 141, 40-52.